

Laboratory Studies of Heterogeneous Chemistry

Brandon Michael Connelly

B.A. Macalester College

A thesis submitted to the Faculty of the Graduate School of the University of Colorado in
partial fulfillment of the requirements for the degree of Doctor of Philosophy

Department of Chemistry and Biochemistry

August 16th, 2010

This thesis entitled:

Laboratory Studies of Heterogeneous Chemistry

Written by Brandon Michael Connelly

Has been approved for the Department of Chemistry and Biochemistry

Professor Margaret A. Tolbert

Professor David O. De Haan

Date: _____

The final copy of this thesis has been examined by the signators and we find that both the content and the form meet the acceptable presentation standards of scholarly work in the above mentioned discipline.

Connelly, Brandon Michael (Ph.D., Department of Chemistry and Biochemistry)

Laboratory Studies of Heterogeneous Chemistry: Reactive Uptake of Isoprene and Glyoxal to Acidic Particles Representative of Tropospheric Aerosols and Ice and Nitric Acid Trihydrate Nucleation Studies on Ammonium Nitrate

Thesis directed by Professor Margaret A. Tolbert

A high vacuum Knudsen flow reactor was used to determine the reactive uptake coefficient, γ , of isoprene on sulfuric acid films as a function of sulfuric acid weight percent, temperature, and relative humidity. No discernible dependence was observed for γ over the range of temperatures (220 – 265 K) and pressures (10^{-7} Torr - 10^{-4} Torr) studied. However, the uptake coefficient increased with increased sulfuric acid concentration between the range of 78 wt % ($\gamma_i 10^{-4}$) and 93 wt % ($\gamma_i 10^{-3}$). In addition to the Knudsen Cell, a bulk study was conducted between 60 and 85 wt % H_2SO_4 to quantify uptake at lower acid concentrations and to determine reaction products. After exposing sulfuric acid to gaseous isoprene the condensed phase products were extracted and analyzed using gas chromatography/mass spectrometry (GC/MS). Isoprene was observed to polymerize in the sulfuric acid and form yellow/red colored monoterpenes and cyclic sesquiterpenes. Finally, addition of water to the 85 wt % sulfuric acid/isoprene product mixture released these terpenes from the condensed phase into the gas phase. Together these experiments imply that direct isoprene uptake will not produce significant

SOA; however, terpene production from the small uptake may be relevant for ultrafine particles and could affect growth and nucleation.

Several laboratory and field studies have suggested that the simple aldehyde glyoxal could be a significant source of secondary organic aerosol (SOA) in the lower troposphere. However, recent studies have found that particles in the upper troposphere also contain significant amounts of organic material, with average organic mass fractions as high as 70%. We have examined whether glyoxal could be a source of SOA in the upper troposphere. The uptake of glyoxal to aerosols generally requires the presence of liquid water. Aerosols in the upper troposphere that could have supercooled liquid on the surface are cirrus ice and particles containing hygroscopic organic material. Several studies indicate cirrus ice may be coated with supercooled liquid $\text{HNO}_3/\text{H}_2\text{O}$. Thus we have utilized a high vacuum Knudsen Cell to measure the uptake of glyoxal on ice exposed to nitric acid at temperatures and pressures relevant to the upper troposphere. Here we present kinetic and spectroscopic data that indicates uptake of glyoxal is efficient on these films and irreversible. Spectroscopic data indicates the glyoxal is oxidized to glyoxylic acid, and the presence of glyoxylic acid has been confirmed via derivatization of the products followed by gas chromatography mass spectrometry. We have used the glyoxylic acid products from the ice experiments to test whether hygroscopic organic material exposed to water and nitric vapour would also uptake glyoxal. We have found that the uptake of glyoxal and oxidation to glyoxylic acid occurs in the presence of supercooled $\text{HNO}_3/\text{H}_2\text{O}$ liquid on glyoxylic acid even at water pressures below the saturation pressure of ice.

The critical saturation ratio required for heterogeneous nucleation of ice was studied on ammonium nitrate films in the presence of nitric acid. Under these conditions deliquescence of the particles was not observed; however, prior to deliquescence the uptake of H₂O was observed. Fourier transform infrared reflectance absorbance spectroscopy (FTIR-RAS) indicates the water absorbed water is liquid like in nature, and the film exists as a mixed solid/liquid phase prior to ice nucleation. The films were observed to freeze prior to the predicted saturation ratio for homogeneous freezing. At temperatures lower than 200 K and nitric acid pressures greater than 10⁻⁷ Torr, nitric acid trihydrate (NAT) nucleation was observed if the saturation ratio was held below the critical saturation ratio for heterogeneous ice nucleation. The growth rate of the NAT and ice films was measured under similar conditions. NAT growth is considerably slower, and laboratory evidence indicates the growth is regulated by the pressure of nitric acid. The critical saturation ratio for ice nucleation on NAT was determined to be higher than the mixed phase films, and approached the ratio required to nucleate ice on the hydrophobic gold surface.

Acknowledgements

In high school, I had the privilege having two very dedicated chemistry teachers; known only as Costigan and McDougal. Early on they recognized my aptitude for chemistry, and encouraged me to continue my education at the collegiate level. Because of their dedication, when I arrived at Macalester I scored 49 out of 50 on the pretest to determine the initial starting level for chemistry instruction. The score I achieved was the highest in the history of the pretest.

The faculty at Macalester College is focused on instruction of the chemistry students. My advisor at Macalester College was Dr. Truman Schwartz, a recipient of the George C. Pimentel Award in Chemical Education. I also had the pleasure of working with Dr. Emil Slowinski and Dr. Wayne Wolsey, coauthors of the widely used general chemistry text *Chemical Principles*, and the corresponding lab manual *Chemical Principles in the Laboratory*. I am grateful for the opportunity to learn from an experienced faculty, and thank them for building the firm foundation of knowledge necessary for my future study of chemistry.

For my graduate studies, I thank my advisor Professor Margaret Tolbert for her leadership and guidance. Dr. Tolbert has allowed me to pursue my own interests, and her continued encouragement and mentorship is greatly appreciated. The research in this thesis could not have been conducted without the technical assistance provided by Don David and Dennis Steffey. I am indebted to them for their help with electronics and custom glassware respectively. I am also appreciative of the entire Tolbert research group for their assistance and friendship. In particular, I would like to thank Christa Hassenkopf for her assistance with complicated mathematical problems encountered in graduate

research. Finally, I thank Gregory Schill for his work on the ammonium nitrate nucleation study.

Most importantly, I thank my wife Nicole Connelly and my two daughters Makayla and Fiona for being the light that guided me through my graduate experience. When research pursuits were difficult, they were always there to brighten my day. My mother and father have also been there for me through the difficult times, and I thank them for listening to me when I needed a kind ear.

Contents

I. Introduction

1.1	Earth's Atmosphere	1
1.2	Emissions of Gas Phase Species	2
1.3	Basics of Tropospheric VOC, NO _x , and OH Chemistry.....	4
1.4	Tropospheric SO ₂	7
1.5	Importance of Aerosols.....	9
1.6	Aerosol Size, Number and Composition	13
1.7	Aerosol Physical Properties: The Direct Effect.....	19
1.8	Aerosol Physical Properties: The Indirect Effect.....	21
1.9	Thesis Focus.....	22

2 Experimental

2.1	Introduction.....	24
2.2	Physical Description of the Knudsen Flow Reactor	24
2.3	Operation of the Knudsen Cell Flow Reactor.....	27
2.4	Interpretation of Knudsen Reactor Data	30
2.5	Fourier Transform Infrared Reflectance Absorbance Spectroscopy	34

3 Reaction of Isoprene on Thin Sulfuric Acid Films

3.1	Introduction.....	38
3.2	Experimental Procedure.....	40
3.2.1	Knudsen Cell.....	40
3.2.2	Infrared Gas Cell.....	41
3.2.3	Gas Chromatography/Mass Spectroscopy	42
3.3	Results and Discussion	44
3.3.1	Kinetics: Knudsen Cell	44
3.3.2	Kinetics: Gas Cell	46
3.3.3	Product Analysis: GC/MS	50
3.3.4	Kinetics: Knudsen Cell	44
3.4	Atmospheric Implications.....	55

4 Uptake of Glyoxal to Supercooled HNO₃/H₂O

4.1	Introduction.....	59
4.2	Experimental	61
4.2.1	Synthesis of Glyoxal.....	61
4.2.2	Glyoxal Uptake to Supercooled HNO ₃ /H ₂ O on ice	61
4.2.3	Amorphous H ₂ O/HNO ₃ Films	64
4.2.4	Gas Chromatography/Mass Spectroscopy	67
4.3	Results and Discussion	68
4.3.1	Glyoxal Uptake on Nitric Acid/Ice Films.....	68
4.3.2	Glyoxal Uptake to Supercooled HNO ₃ /H ₂ O on Organic.....	74
4.4	Atmospheric Implications.....	76

5 Laboratory investigations on the effect of nitric acid vapour on ice nucleation on ammonium nitrate (AN) thin films and experimental determination of the growth rate of NAT.

5.1	Introduction	80
5.2	Experimental	84
5.2.1	Preparation of Optically Flat AN Films.....	84
5.2.2	Experimental Determination of S_{crit}	85
5.2.3	Water Uptake Experiments	89
5.3	Results and Discussion.....	90
5.3.1	Ice Nucleation on Ammonium Nitrate.....	90
5.3.2	Ice Nucleation on AN in the Presence of Nitric Acid.....	96
5.3.3	Experimental Determination of the NAT Growth Rate.....	101
5.4	Atmospheric Implications	106

Tables

Chapter 1

Table 1.1. Global emission estimates for CO, NO_x, CH₄, VOC, and sulfur compounds2

Table 1.2. Global emission estimates for biogenic VOC.....3

Chapter 5

Table 5.1. Growth of ice and NAT films at 190 and 200 K.....104

Figures

Chapter 1

Figure 1.1. The effect of particle size on deposition of aerosols in the human respiratory tract.	10
Figure 1.2. Aerial photo of the Denver metropolitan area during a “Brown Cloud” event.....	11
Figure 1.3. Summary of the individual anthropogenic effects on radiative forcing from the IPCC (2007).....	12
Figure 1.4. A typical particle size distribution for ambient particulate matter is illustrated.....	14
Figure 1.5. A Saharan dust storm off the east coast of Africa pictured from space.	15
Figure 1.6. Average particle mass loading and composition as determined by FA-AMS for different regions of the earth.	17
Figure 1.7. A general water uptake and loss scheme for aerosol.....	20

Chapter 2

Figure 2.1. A schematic of the Knudsen flow reactor.	25
Figure 2.2. Example uptake plots for the Knudsen Cell.	31

Chapter 3

Figure 3.1. Isoprene uptake experiments performed at 1×10^{-5} Torr isoprene.	45
Figure 3.2 A plot of the initial reactive uptake coefficient, γ_i , as a function of sulfuric acid wt% for the Knudsen Cell.	47
Figure 3.3 Plots of $\ln(P/P_o)$ vs time for isoprene uptake in the static IR gas cell.	48
Figure 3.4. A plot of the steady state reactive uptake coefficient, γ_{ss} , vs wt% H_2SO_4 for the IR gas cell experiments.	49
Figure 3.5. Chromatograms from bulk study and chamber film extract	

of isoprene uptake on 85 wt% sulfuric acid.....	51
Figure 3.6. Mass spectra of uptake experiments performed on 85 wt% sulfuric acid.....	52
Chapter 4	
Figure 4.1. A. FTIR-RAS spectrum of ice film exposed to nitric acid.....	62
Figure 4.2. FTIR-RAS spectra of 4:1 amorphous H ₂ O/HNO ₃ films.	65
Figure 4.3. A calibration plot of thickness vs peak area for the 4:1 amorphous H ₂ O/HNO ₃ film.....	66
Figure 4.4. Mass spectrometer signal vs time for glyoxal uptake experiments.....	69
Figure 4.5. Plot of γ vs pressure of nitric acid for glyoxal uptake on supercooled HNO ₃ /H ₂ O on ice.	70
Figure 4.6. FTIR-RAS spectra of the products of the glyoxal uptake.	72
Figure 4.7. The mass spectra of the two derivatized glyoxal uptake products.....	73
Figure 4.8. γ vs RH _{ice} for glyoxal uptake to supercooled HNO ₃ /H ₂ O on organic material.	75
Chapter 5	
Figure 5.1. FTIR-RAS spectra of the <i>in situ</i> growth of an ammonium nitrate film.....	86
Figure 5.2. A sample experiment for determination of S_{ice} on ammonium nitrate films.	87
Figure 5.3. A closer view of the nucleation point from the S_{ice} experiment in Figure 5.2.....	88
Figure 5.4. FTIR-RAS spectra of the AN film prior to water uptake and after exposure to 2.44×10^{-4} Torr H ₂ O at 190 K.....	91
Figure 5.5. Water uptake to ammonium nitrate at 190 K.	93
Figure 5.6. Spectra of aqueous ammonium nitrate at different relative humidity at 293 K from Cziczo and Abbatt (2000).	95

Figure 5.7. S_{ice} values determined for heterogeneous ice nucleation for mixed phase AN films and nitric acid trihydrate.	97
Figure 5.8. The uptake of water to an ammonium nitrate film exposed to 10^{-7} Torr H_2O	99
Figure 5.9. FTIR-RAS spectra of the nucleation of nitric acid trihydrate on ammonium nitrate.	100
Figure 5.10. FTIR-RAS interference patterns form the growth of ice (A) and of NAT.	102
Figure 5.11. FTIR-RAS spectra of NAT films during growth and sublimation under high vacuum.	105

Chapter I

6 Introduction

6.1 Earth's Atmosphere

The atmosphere of the Earth is primarily composed of nitrogen ($N_2 \sim 78\%$), oxygen ($O_2 \sim 21\%$), and several noble gases which combined encompass more than 99% of the total dry atmosphere (Seinfeld and Pandis, 1998). However, while trace gas species and aerosols comprise less than 1% of the atmosphere, their composition and chemistry have a significant effect on the physical and chemical properties of the atmosphere as a whole. Trace gases and aerosols have a wide degree of variability with respect to altitude, region, season, and time of day. The lowest region of the atmosphere is the troposphere, which extends from the surface of the earth to 8 – 18 km, depending on latitude and time of year. The troposphere experiences the largest fluctuations in composition. Surface-based anthropogenic and biogenic emissions are responsible for the diverse concentrations of trace gas species and the composition of aerosols. The troposphere is divided into two sections, the lower troposphere which extends to the boundary layer, and the upper or free troposphere which extends from the boundary layer to stratosphere. The troposphere comprises 90% of the mass of the Earth's atmosphere (Jacob, 1999). The complex heterogeneous chemical processes involving trace gasses and aerosols within the troposphere are the focus of the thesis.

Species	Anthropogenic sources	Biomass burning	Continental biogenic sources	Oceans	Total
CO	383	730	165	165	1440
NO _x	72	18	22	0.01	122
CH ₄	132	54	310	10	506
VOC	98	51	500	30-300	750
Sulfur compounds ^a	77.6	2.3	0.9	11.9	102.2 ^b

^a Spiro et al., 1992

^b Includes 9.6 Tg/yr from volcanic activity

Table 1.1. Global emission estimates for CO, NO_x, CH₄, VOC (Müller, 1992) and sulfur compounds (Spiro, 1992) in Tg/yr (Table adapted from Finlayson-Pitts and Pitts, 2000).

Species	Isoprene	Monoterpene	Other more reactive organics ^a	Other less reactive organics ^b	Total VOC
Woods	372	95	177	177	821
Crops	24	6	45	45	120
Shrubs	103	25	33	33	194
Ocean	0	0	52.5	2.5	5
Other	4	1	2	2	9
Total	503	127	260	260	1150

^a Defined as having a lifetime < 1 day under typical atmospheric conditions

^b Defined as having a lifetime > 1day

Table 1.2 Global emission estimates from biogenic sources for selected compounds in Tg/yr (Values from Guenther, 1995; Table adapted from Finlayson-Pitts and Pitts, 2000).

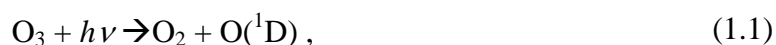
6.2 Emissions of Gas Phase Species

Gas phase species are emitted into atmosphere through anthropogenic, biogenic, marine, and geogenic sources. Table 1.1 is a brief summary of global emission estimates from anthropogenic and natural sources for carbon monoxide (CO), nitrogen oxides (NO_x), methane (CH₄), volatile organic compounds (VOC), and sulfur compounds (Müller, 1992; Spiro, 1992; Finlayson-Pitts and Pitts, 2000). Many different chemical species comprise the volatile organic compound class. Generally the class is divided into two subsets, non-methane hydrocarbons (NMHC) and oxygenated organic compounds (OOC) which may come from either anthropogenic or biogenic sources. As indicated in Table 1.1, a majority of the VOC is sourced naturally and a summary of the global emissions of biogenic VOC is shown in Table 1.2 (Guenther, 1995; Finlayson-Pitts and Pitts, 2000).

6.3 Basics of Tropospheric VOC, NO_x, and OH_x Chemistry

Given the wide variety and variability of gasses in the atmosphere, the gas phase chemistry of the atmosphere is complex. Accurate models account for numerous photochemical reactions, gas phase reactions, branching ratios and multigenerational decomposition of organic compounds. Presented here is a brief overview of gas phase chemistry necessary for the understanding of the thesis. The overview will focus on VOCs, the nitrogen oxide species (NO_x), ozone, and hydroxide radical species (HO_x).

The primary oxidant in troposphere is hydroxy radical, OH. Hydroxy radical is primarily sourced by the photochemistry of ozone (Jacob, 1999),





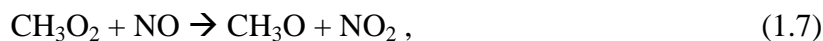
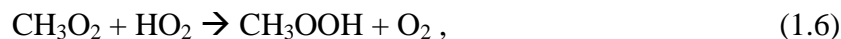
where M is a stabilizing third body. Hydroxy radical can extract hydrogen from any VOC in the atmosphere to form water and an alkyl radical; for the simplest scenario we will examine methane:



The CH_3 radical quickly reacts with oxygen to form a methylperoxy radical:



The peroxy radical (CH_3O_2) will generally follow one of the following pathways depending on whether it reacts with HO_2 or NO :



though other minor pathways are possible. The methylhydroperoxide (CH_3OOH) from Equation 1.6 may either react with OH or photolyze. The OH reaction has two pathways; one regenerates the methylperoxy radical (H extracted from OOH) and the other forms formaldehyde. Photolysis of the methylhydroperoxide yields the same methoxy radical product from Equation 1.7 (and generates an OH). The methoxy radical (CH_3O) quickly reacts with O_2 to form formaldehyde (CH_2O) by



The HO_2 product from Equation 1.8 can react with NO and regenerate ozone through



Additionally, under low NO conditions HO₂ may self-react or destroy ozone:

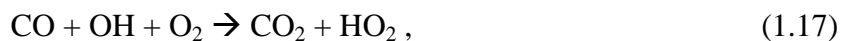


Note the NO₂ produced by Equation 1.7 will also regenerate ozone via Equations 1.10 and 1.11. The formaldehyde can either react with OH or photolyze via two branches:



The CHO radical reacts quickly with oxygen to produce carbon monoxide and HO₂.

Carbon monoxide also reacts with OH, and in the presence of NO,



From here, the NO₂ creates additional ozone as described in Equations 1.10 and 1.11.

Oxidation of higher order hydrocarbons and oxygenated organic material by OH follows a similar pathway as methane; however, the complete pathway to total oxidation to CO₂ and H₂O becomes more complex. There are a multitude of reaction pathways involving different fragmentations and rearrangements of the original molecule. Each run of the oxidation cycle creates a more oxygenated organic compound, and in turn these compounds further oxidize, fragment, and rearrange.

The above equations for methane oxidation describe two distinct oxidation pathways, and the route that the VOC follows will depend on the OH₂ and NO

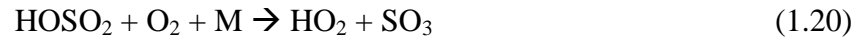
concentration from Equations 1.6 and 1.7. While each path essentially reduces methane to CO_2 , the NO path (1.6) will create 5 O_3 molecules and 2 OH radicals per methane or per oxidation cycle for larger VOC. The HO_2 (1.7) path will consume 3 OH radicals and not produce ozone. As shown in Table 1.1, NO_x is primarily sourced by anthropogenic activities, namely combustion. Therefore, urban environments often experience photochemical smog from high VOC and NO_x emissions, via the NO_x path (1.6). The NO_x path represents a catalytic cycle, where high NO_x increases ozone and OH via reactions with VOCs, thereby increasing the VOC oxidation rate of the atmosphere. For this reason, the federal government has set National Ambient Air Quality Standards (NAAQS) that restrict the concentrations of NO_x , O_3 , and CO (USEPA, 2005). High concentrations of these compounds in conjunction with high concentrations of particulate matter have been found to have profound impacts on human health (Dockery, 1993; Katsouyanni, 1993; Nel, 2005).

It is important to note that OH radical oxidation is only one pathway for the oxidation of organic species in the atmosphere. Other species, such as the ozone produced in the reaction sequence above, nitrate radicals (NO_3), and heterogeneous pathways also play a role depending on concentration, location, seasonality, and even time of day.

6.4 Tropospheric SO_2

In addition to NAAQS restricting the compounds listed above, the standards also restrict sulfur emissions, in particular sulfur dioxide (SO_2). The marine biosphere and volcanic activity produce sulfur naturally, but the anthropogenic sources dominate the emission profile as shown in Table 1.1. One source that is strong in the Eastern United

States is coal fired power plants (Lee, 2009). The coal mined from the Appalachian Mountains is rich in sulfur (Ruppert, 1999) and the combustion of the coal releases the sulfur as SO_2 . In the gas phase SO_2 can react with hydroxyl radical:



and form sulfuric acid, H_2SO_4 . Reactions 1.20 and 1.21 occur quickly, while Reaction 1.19 is relatively slow. The lifetime of SO_2 with respect to oxidation by OH, τ_{OH} , which is simply the inverse of the gas phase rate constant (with respect to OH), k_{OH} , is ~ 13 days.

Sulfuric acid has a low volatility, and new particle formation has been linked to H_2SO_4 concentrations. The exact mechanism is unknown and the topic of continued research, but it is generally accepted that the low volatility sulfuric acid forms molecular clusters which then grow to new particles (Seinfeld and Pandis, 1999; Sipilä, 2010). Sipilä and coworkers (2010) have proposed two nucleation pathways: kinetic and activation described by

$$J = K[\text{H}_2\text{SO}_4]^2, \quad (1.22)$$

$$J = A[\text{H}_2\text{SO}_4], \quad (1.23)$$

where J is the nucleation rate in number $\text{cm}^{-3} \text{s}^{-1}$, K and A are the empirically determined kinetic and activation constants, and $[\text{H}_2\text{SO}_4]$ is the gas phase concentration of sulfuric acid. The kinetic nucleation is collision controlled, while the activation requires that preexisting clusters heterogeneously react with another molecule. The most commonly

investigated “activating” molecules are ammonia (Smith, 2005; Benson, 2009) and more recently organic molecules (O’Dowd, 2002; Smith, 2008).

While gas phase H_2SO_4 production can cause new particle formation events, the kinetics are insufficient to account for the high rain acidity in the geographic regions surrounding areas with high SO_2 emissions (Jacob, 1999). It has been found that sulfur dioxide makes acid rain through aqueous phase reactions (Martin, 1994). The deadly London fog of 1952 (~ 4000 deaths) caused by SO_2 production was an early indication that a comprehensive understanding of aerosols and heterogeneous chemistry are important for human health (Finlayson-Pitts and Pitts, 2000). This leads us to the next sections which introduce and discuss aerosols.

6.5 Importance of Aerosols

Ambient particulate matter in the Earth’s atmosphere affects human health, visibility, and global climate. Studies have found that the high aerosol concentrations found in urban environments correlate to an increased risk to human health (Dockery, 1993; Nel, 2005; Pope, 2009). Particle size determines where aerosols deposit in the human respiratory system as shown in Figure 1.1 (Heyder, 1986; Patton, 2007). While larger particles are removed by the nose and throat, small or ultrafine particles tend to deposit deep in the alveoli of lung tissue. Aerosol size and concentration also affect visibility by scattering light. Figure 1.2 is a photo of the Denver area, where a “brown cloud”, caused by local pollution, is significantly reducing visibility. Scattering and absorbance of light by aerosols also impacts global climate. Figure 1.3 is a summary of the anthropogenic effects on radiative forcing from the Intergovernmental Panel on

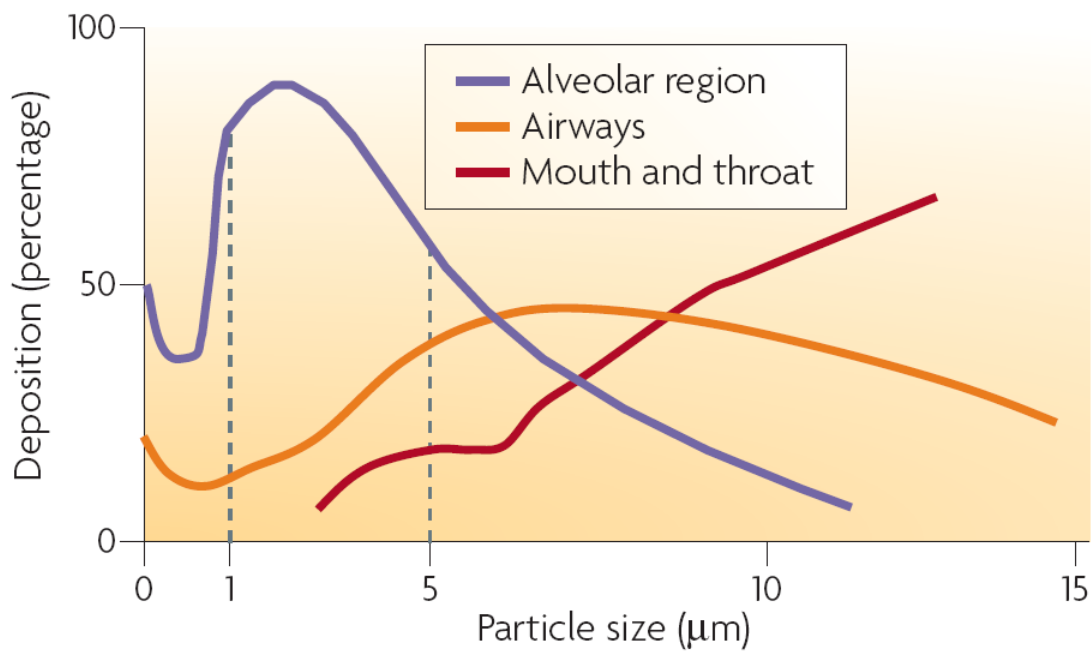


Figure 1.1. The effect of particle size on deposition of aerosols in the human respiratory tract. Figure from Patton and Byron (2007).



Figure 1.2. Aerial photo of the Denver metropolitan area during a “Brown Cloud” event. The particulate levels are high enough to obscure the ground. Photo from the Denver’s regional air quality council:
(http://www.epa.gov/oar/caaac/aqm/200608_denveraq.pdf)

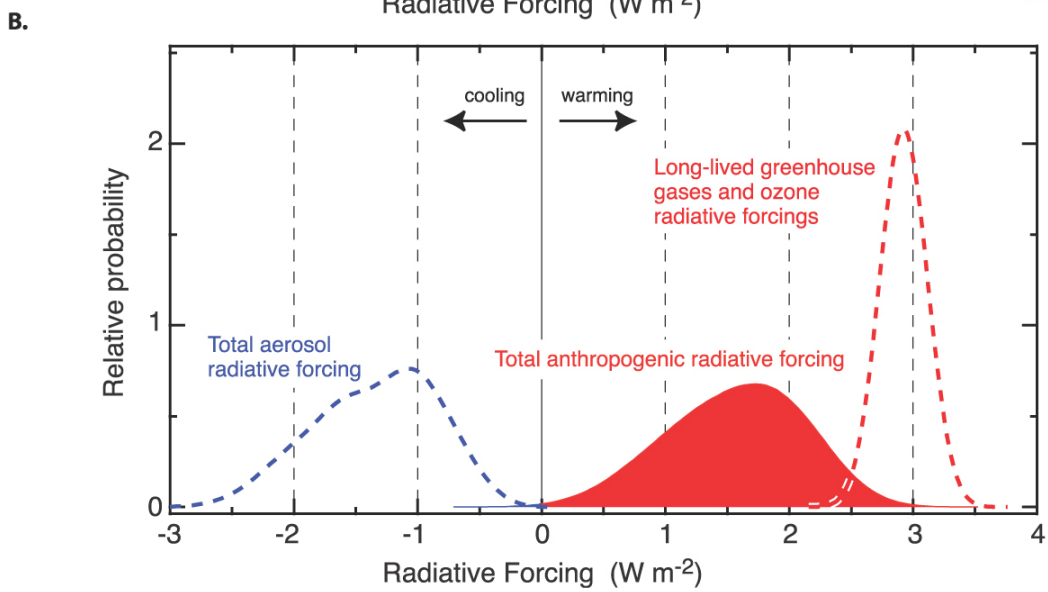
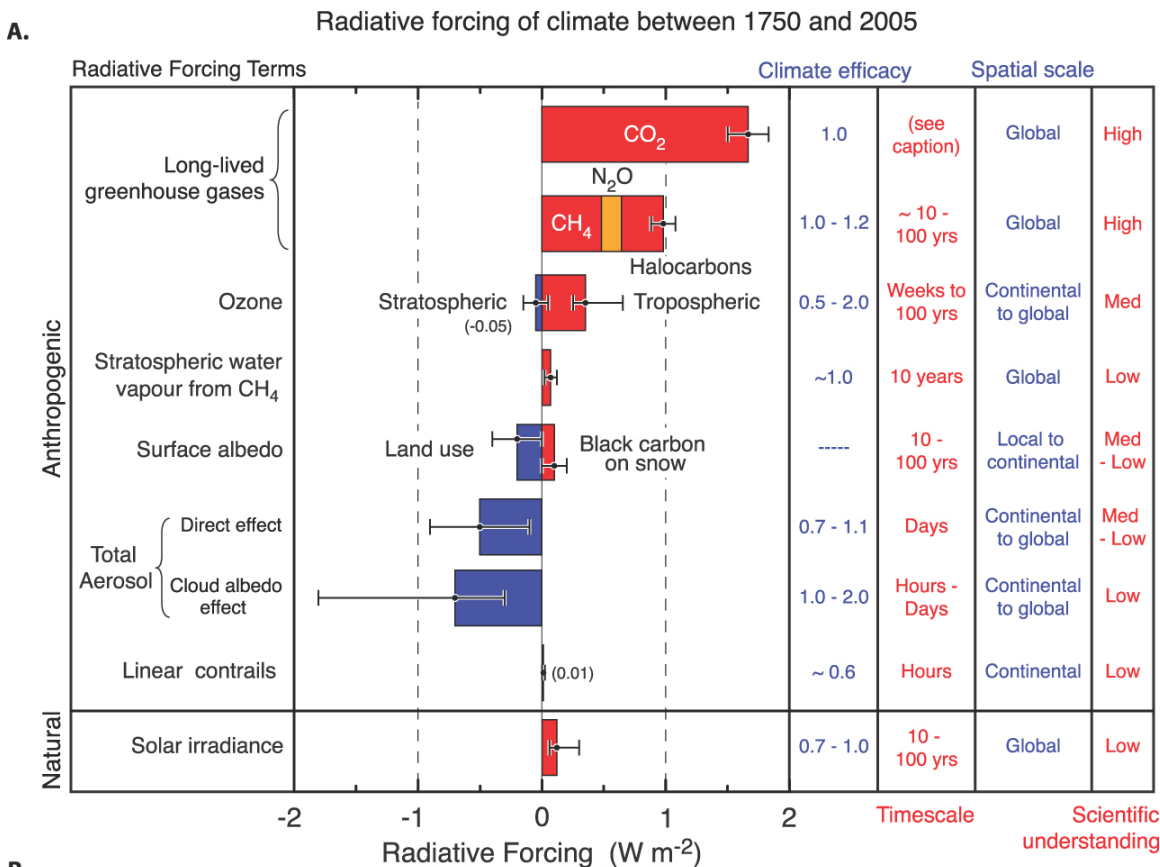


Figure 1.3. A. Summary of the individual anthropogenic effects on radiative forcing from the IPCC. **B.** A probability distribution of the total aerosol (blue dash), total long lived green house gases and ozone forcing (red dash) and the sum of these two effects (solid red). Figure from Soloman et al. (2007).

Climate Change (Solomon, 2007). In Figure 1.3 greenhouse gasses, ozone, stratospheric water vapor, and surface albedo all have relatively small error bars indicating these processes are relatively well understood. On the other hand we can see that the aerosol effects have large error bars, because these processes are not well understood. In order to increase our understanding of the radiative forcing effects of anthropogenic activity, we need increased understanding of the physical and chemical processes of aerosol.

6.6 Aerosol Size, Number, and Composition

Ambient particulate matter encompasses a diverse range of size, concentration, chemical composition, and physical properties. Tropospheric particle diameters range five orders of magnitude in size as shown in Figure 1.4 (Whitby and Cantrell, 1976). The smallest and generally most numerous particles are termed ultrafine, nucleation, or Aitkin mode particles. These are created by the clustering of low volatility gas molecules, such as H_2SO_4 or organic material of low volatility. These particles then grow via continued condensation and coagulation to the fine mode or accumulation mode. The accumulation mode particles range from 0.1 to 2.5 μm in diameter. These particles are usually smaller in number than the Aitkin mode particles, however they tend to compose the greatest surface area of the three modes. Accumulation mode particles have the longest lifetime in the troposphere. The slower mobility of accumulation mode particles reduces coagulation and they are small enough to remain lofted and “accumulate” in the atmosphere. Particles greater than 2.5 μm are termed coarse particles and are produced by physical or mechanical processes. These particles have a relatively short lifetime in the atmosphere due to their size, and gravitationally settle near the source.

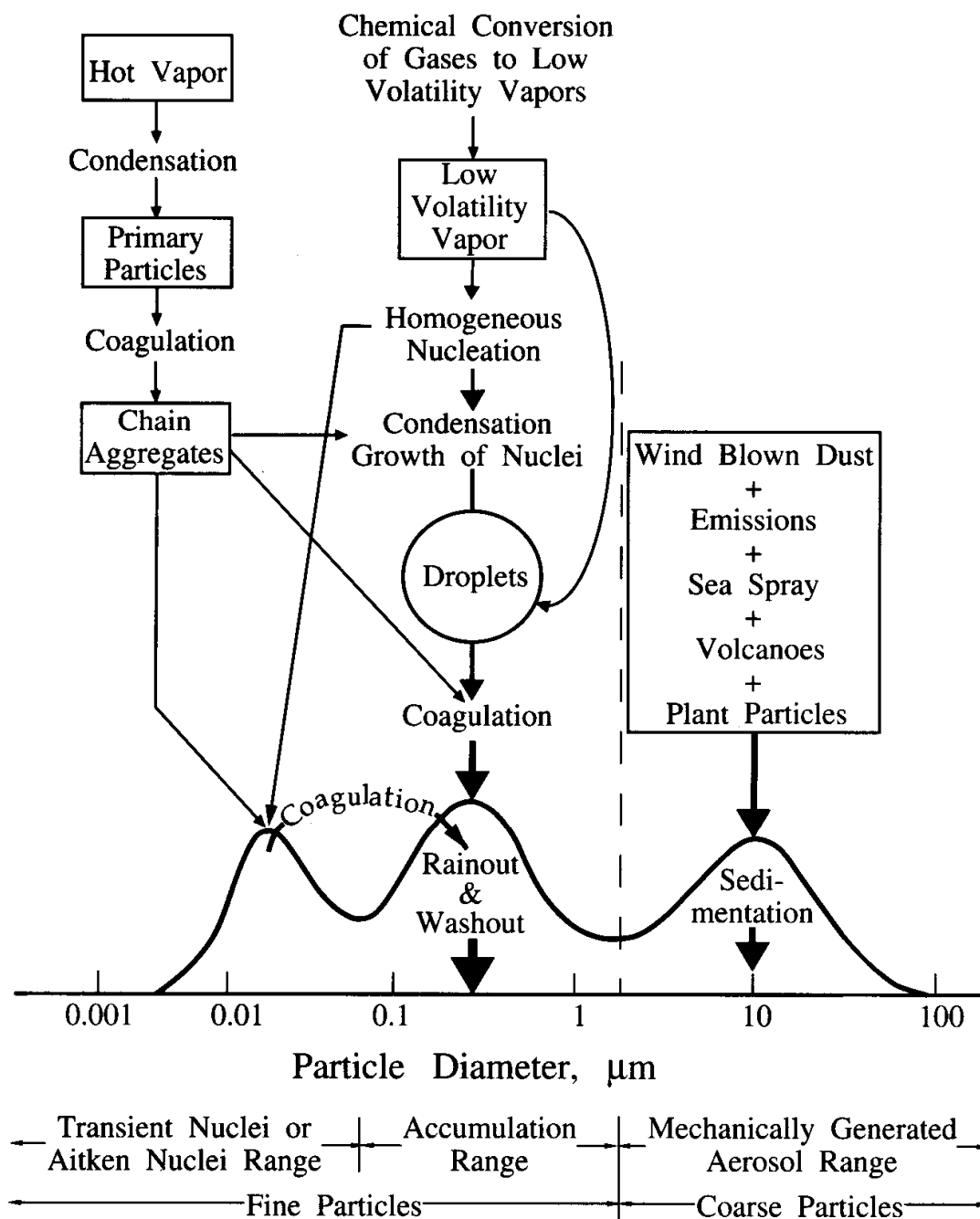


Figure 1.4. A typical particle size distribution for ambient particulate matter is illustrated. Three modes are shown, the transient nuclei or Aitken Nuclei (also called ultrafine): ~ 1 – 100 nm; the accumulation range (also called fine): ~ 0.1 – 1 μm ; and the coarse mode: ~ 1 – 100 μm . The most common sources lie above each mode, while under the distribution the common sinks for each mode are listed. Figure from Whitby and Cantrell (1976).

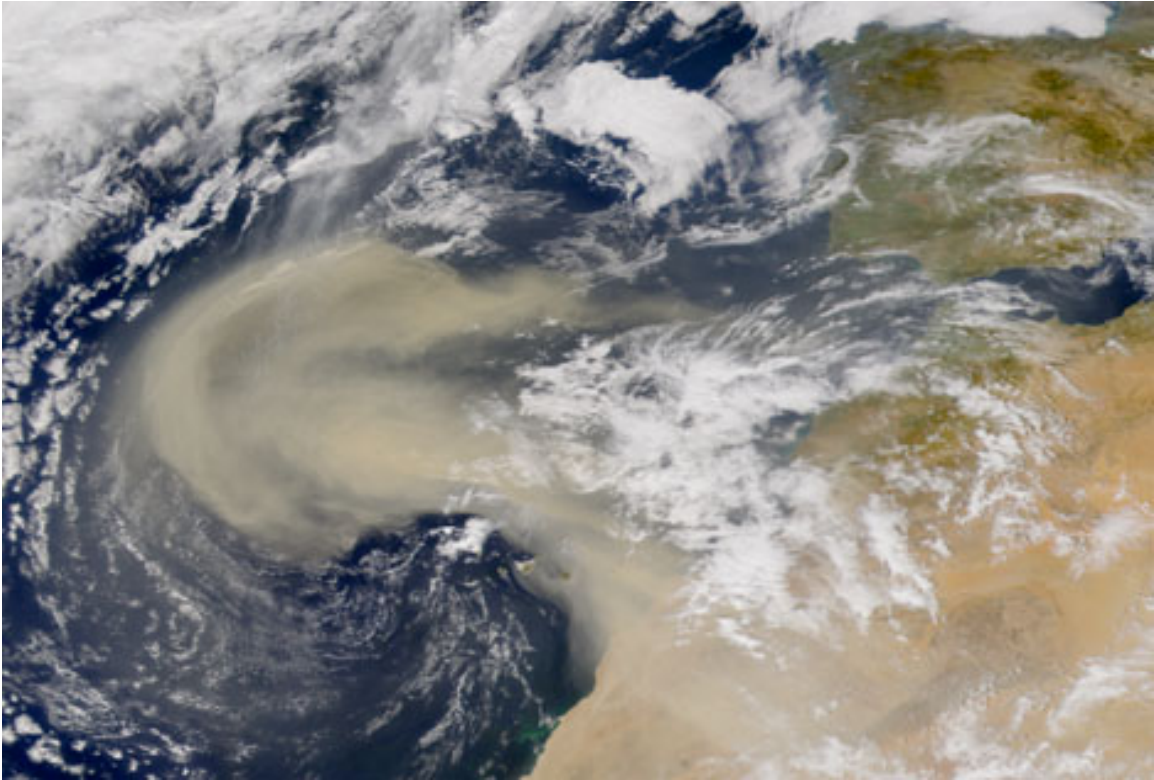


Figure 1.5. A Saharan dust storm off the east coast of Africa pictured from space. Picture from UCAR (<http://www.ucar.edu/communications/newsreleases/2003/DustStorm.jpg>).

Ambient particles also vary in their chemical composition. In the coarse fraction, particles are generally composed of dirt, dust, debris, soot or plant matter (pollen, spores, etc.). In the accumulation mode particles usually are internal mixtures of multiple components. They may be composed of inorganic and organic matter, or even minerals from dust storms, as pictured in Figure 1.5. The average particle composition at different measurement locations determined by aerosol mass spectroscopy (AMS) is shown in Figure 1.6 (Jimenez, 2009). In Figure 1.6 the pie charts show the average mass fraction of non-refractory material in the particles as classified and determined by factor analysis of AMS data (FA-AMS) (Ulbrich, 2009). The number above each pie chart shows the average particle concentration in micrograms per cubic meter. The legend for the pie charts shows the divisions determined by FA-AMS. Primarily the components split into two categories: inorganic and organic material. The inorganic fraction consists of sulfate, nitrate, ammonia, and chloride; while the organic fraction is broken down into the following components:

1. Hydrocarbon-like organic aerosol (HOA), generally primary aerosols from emissions with a low oxygen to carbon (O:C) ratio of ~ 0.1 as indicated in the insert in Figure 1.6.
2. Other organic aerosol (Other OA) includes primary organic aerosol different than HOA, such as organic aerosol produced by biomass burning (BBOA). Other OA tends to have a slightly higher O:C ratio than HOA of ~ 0.2 .
3. Semi-volatile oxygenated organic aerosol (SV-OOA) which is semi-volatile organic matter that has been slightly aged in the atmosphere as described in Chapter 1.2 (and through other methods), giving it an O:C ratio of 0.3.

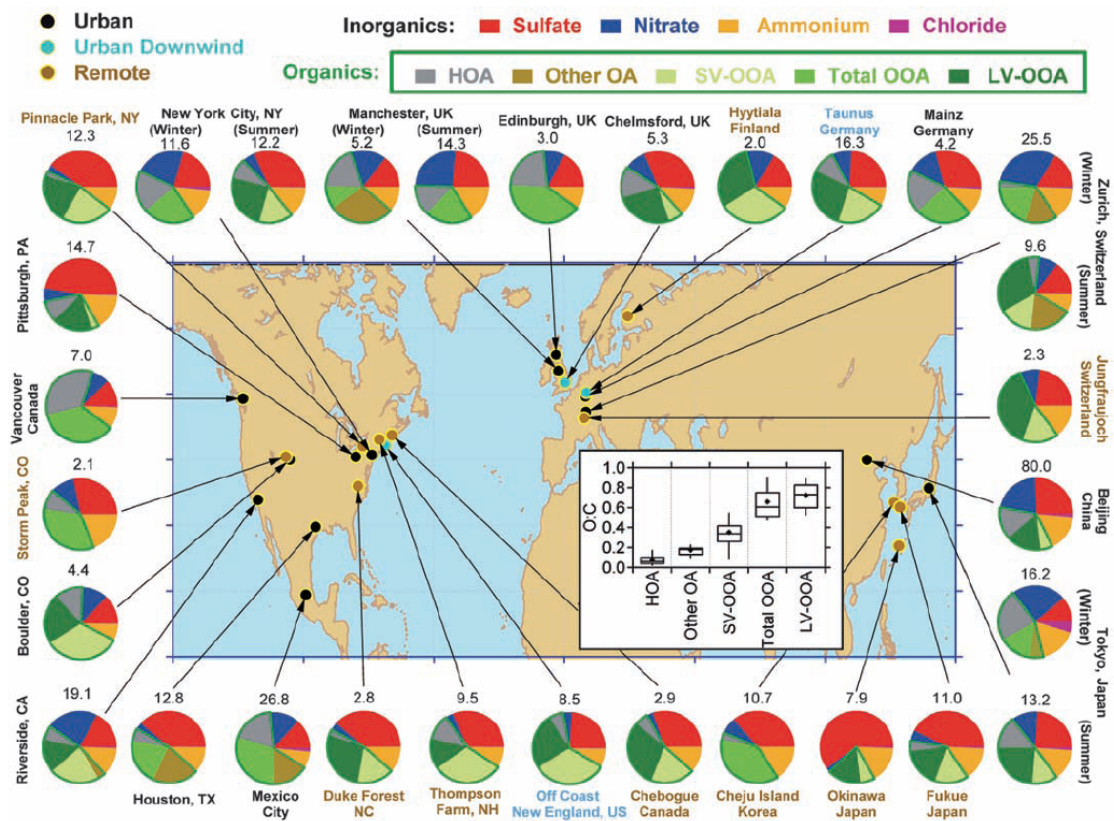


Figure 1.6. Average particle mass loading and composition as determined by FA-AMS for different regions of the earth. The inset is the oxygen to carbon ratio for each subgroup of organic material determined by the FA-AMS analysis. Figure from Jimenez et al. (2010).

4. Low volatility oxygenated organic aerosol (LV-OOA) which consists of organic matter significantly aged in the atmosphere with the highest O:C ratio of ~0.8.

5. Total oxygenated organic aerosol (Total-OOA) is a category where FA-AMS did not find a distinction between SV-OOA or LV-OOA. The O:C ratio of this component averages to ~0.7.

Within these 5 subgroups there are hundreds of identified, and thousands, if not more, unidentified compounds. Figure 1.6 illustrates that the variability of vapor emissions and gas phase composition discussed in Chapter 1.2 is also present and even more complex in the condensed aerosol phase.

Understanding the physical processes that create the wide variety of aerosol compositions is important. For example, if you compare the urban location of Pittsburgh in the U.S.A. to the Japanese city of Fukue in Figure 1.6, the mass loading and FA-AMS composition are similar. However, the mechanisms for the aerosol production and aerosol chemical composition may be different. Chemicals with similar oxygen to carbon ratios can have distinctly different physical properties and toxicities. The study by Dockery et al. (1993) indicates that urban aerosol has the direst effects on human health compared to rural aerosol. Exploring the fundamental chemical mechanisms and heterogeneous processes may lead to understanding of the chemical compounds that cause the observed ill effects. Particle composition also determines its physical properties which can affect the climate as discussed in the next section.

6.7 Aerosol Physical Properties: The Direct Effect

Particle size and chemical composition determines how particles interact with both incoming and outgoing radiation. Aerosols can either scatter or absorb light, which has impacts on both visibility (Figure 1.2) and radiative forcing (Figure 1.3). The wavelength of incoming radiation, $\sim 300\text{-}700$ nm in the troposphere, is on the order of the particle diameter of the accumulation mode shown in Figure 1.4. Particles of this size scatter light according to Mie theory. Extinction, σ_{ext} , in the Mie scattering regime is a function of the wavelength of radiation, particle size, number concentration, and the real and imaginary refractive index of the particle. Atmospheric extinction is the sum of both scattering and absorbance by particles and gasses, and the ratio of transmitted light, I , to incoming light, I_o , is described by Beer-Lambert-Bouguer law:

$$\frac{I}{I_o} = \exp(-\sigma_{ext}l), \quad (1.24)$$

where l is the path length through the atmosphere. The scattering and absorption of light is known as the aerosol direct effect.

In the atmosphere particle size and composition can change rapidly when a particle endures a phase change, which in turn changes its extinction. The phase of particle, either solid or liquid, depends on the composition, the relative humidity, and the history of the particle as shown in Figure 1.7. At low relative humidity the particle is a solid, but as relative humidity increases the particle will uptake water at its deliquescence relative humidity, DRH. Once deliquesced, the particle will remain liquid until the

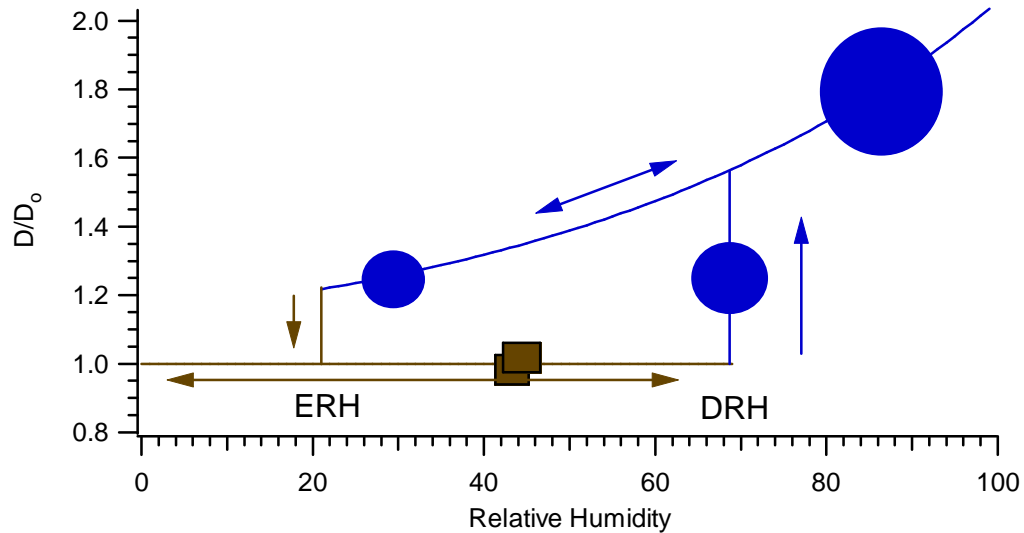


Figure 1.7. A general water uptake and loss scheme for aerosol. The efflorescence relative humidity (ERH) is when a particle will change from liquid to solid phase. The deliquescence relative humidity is the change from solid to liquid phase. As shown in the diagram, determining the particle phase requires knowledge of its history. For example, at 50% RH the particle would either be solid, if it has a “dry” history or liquid if the particle has previously deliquesced (and not effloresced).

relative humidity drops to the efflorescence relative humidity, ERH. At this point the particle will transform into a solid, repartitioning the water to the gas phase. The deliquescence and efflorescence of pure inorganic compounds have been well characterized (Seinfeld and Pandis, 1999), and research has begun to classify organic/inorganic mixtures (Tang, 1996; Marcolli, 2004; Beaver, 2008; Freedman, 2009).

6.8 Aerosol Physical Properties: The Indirect Effect

In the upper troposphere, aerosols serve as a site for the formation of cirrus clouds. Cirrus clouds are thin, wispy clouds composed of few ice particles. The size, number, and composition of the ice particles have an effect on climate, known as the aerosol indirect effect. If the number of ice particles is increased the cloud albedo also increases reflecting more radiation to space. However, if the clouds contain more water, or even liquid water, they will absorb outgoing infrared radiation from earth having a warming effect.

The thin cirrus clouds of the upper troposphere have presented some unique physical behaviors that elude current scientific understanding. First, studies have found that only a few particles nucleate ice, about 1 in 10^4 to 10^6 (Jensen, 2005). Researchers have investigated a variety of substances to determine if nucleation is favored for a particular particle (Zuberi, 2002; Beaver, 2006; Knopf, 2006; Shilling, 2006; Baustian, 2010). However, field measurements indicate there is not a discernable chemical difference between the ice nuclei and the other particles (Froyd, 2010). Second, field measurements have repeatedly found persistent supersaturations in ice clouds (Jensen, 2001 & 2005; Shibata, 2007; Gensch, 2008). Recently, it has been determined that particles in upper troposphere contain a mixture of organic and inorganic material

(Cziczo, 2004; Murphy, 2007; Froyd, 2009). The possible effects of organic material on ice nucleation have begun to be investigated (Wise, 2004; Garland, 2005; Karcher, 2005; Beaver, 2006; Shilling, 2006; Murray, 2008; Baustian, 2010). With respect to the persistent supersaturations, different mechanisms have been proposed and investigated. (Gao, 2004; Shilling, 2006; Zobrist, 2008; Bogdan and Molina, 2009); however the results have been inconclusive. Additional research is needed to gain a firm understanding of cirrus formation which is necessary for determining the overall radiate forcing effects of cirrus clouds.

6.9 Thesis Focus

Recent technological advances, laboratory, and field studies have improved our understanding of aerosol composition. However, atmospheric models based on measurements and laboratory data often underpredict the SOA formation throughout the troposphere and explicit models do not accurately predict SOA concentrations or the degree of oxidation (Jimenez, 2009). The research in this thesis is focused on the kinetics and mechanisms of heterogeneous chemistry. Field studies offer valuable information from which other scientists develop hypotheses and models of chemical processes. Laboratory studies are necessary to confirm, refute, or adjust models; improving our understanding of the atmospheric system. Fundamental kinetic information is necessary to determine the significance of proposed chemical mechanisms. In this thesis, Chapter 2 and 3 describe laboratory investigations of acid-catalyzed heterogeneous chemistry of organic compounds relevant to the lower troposphere (Chapter 2) and the upper troposphere (Chapter 3). The uptake of the biogenically sourced compound isoprene to sulfuric acid films is examined in Chapter 2. The significance of the uptake with respect

to both secondary organic aerosol formation and particle nucleation is discussed. Chapter 3 investigates the nitric acid catalyzed uptake of glyoxal to supercooled liquid layers of $\text{HNO}_3/\text{H}_2\text{O}$ on ice and organic matter under conditions relevant to the upper troposphere. Chapter 4 focuses on the effect of nitric acid on ice nucleation and growth on ammonium nitrate films at conditions relevant to the upper troposphere. Additionally, the growth rate of NAT is measured and compared to ice, which has implications for the formation and growth observed in cirrus clouds. The studies in this thesis offer relevant pieces to the very complex puzzle that is the Earth's atmosphere.

Chapter II

7 Experimental

7.1 Introduction

A high vacuum stainless steel Knudsen flow reactor was used for the majority of experiments presented in this thesis. The chamber was designed to study simultaneously both heterogeneous uptake kinetics and condensed phase products. Reaction kinetics are determined by monitoring the gas phase using absolute pressure measurements and mass spectroscopy, while the condensed phase composition is determined by Fourier transform reflectance absorption spectroscopy (FTIR-RAS). Coupling these experimental techniques yields a detailed picture of heterogeneous processes. An overview of the Knudsen flow reactor will be presented in this chapter, while procedures particular to a set of experiments can be found in the following chapters.

7.2 Physical Description of the Knudsen Flow Reactor

The Knudsen flow reactor is illustrated in Figure 2.1. The chamber is primarily composed of stainless steel, with each section of the chamber sealed together by Conflat flange seals and copper gaskets. A Balzers TPH 240 turbomolecular pump serves to pump down the chamber, with pumping speed of 240 L s^{-1} . Above the turbomolecular pump there is a gate valve with a small hole drilled through it, which serves as a calibrated escape orifice. With the gate valve open, the turbomolecular pump evacuates the chamber to pressures ranging 0.7 to 2.0×10^{-7} Torr. With the gate valve closed, the small escape orifice pumps the chamber to $\sim 1.0 \times 10^{-6}$ Torr. The internal chamber pressure is monitored by a Baratron capacitance manometer (MKS, 690A), an ion gauge

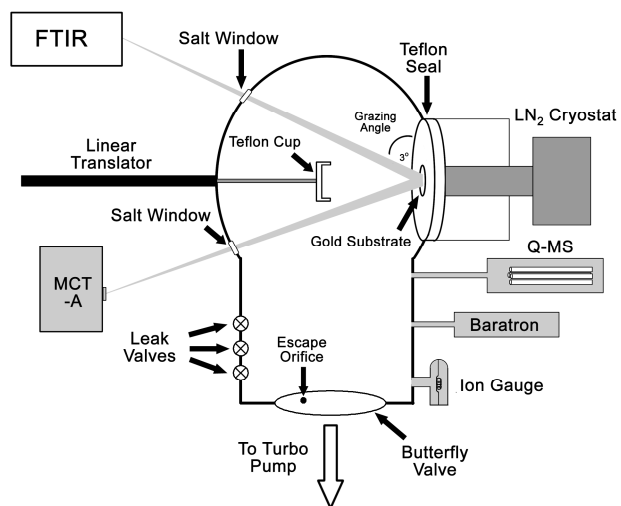


Figure 2.1. A schematic of the Knudsen flow reactor.

(Granville-Phillips), and an electron ionization quadrupole mass spectrometer (UTI 100C).

The chamber supports a vertically mounted 2.54 cm^2 gold mirrored surface (Janos Technology) where condensed phase substrates are grown. The surface is attached to a copper mount, which in turn is attached to a liquid nitrogen cryostat. The temperature of the surface is controlled by resistively heating the copper mount against the cryostat. A Eurotherm PID controller is used to control the resistive heating to set the temperature. The temperature is monitored by T-Type thermocouples that are attached directly to the mount of the gold surface using Stycast thermally conductive epoxy-resin (Lake Shore Cryotronics). The gold surface is sealed to the chamber with a custom Teflon seal (Eclipse Engineering). The copper mount and cryostat are enclosed in stainless steel, and the enclosed volume is evacuated using a rough pump. This serves to isolate the low temperature of the cryostat and gold surface from the chamber ensuring that the gold surface is the coldest surface exposed to the chamber atmosphere.

A small Teflon cup attached to a pneumatic linear translator is positioned perpendicular to the gold surface. The cup is used to isolate the gold surface from the chamber atmosphere, and in turn expose the surface to the gasses in the flow reactor. The volume of the cup is $\sim 7 \text{ mL}$, which composes only 0.1% of the 7 L chamber volume. When the cup is retracted, the small expansion coupled with the continuous flow conditions of the reactor result in a minute pressure change that lies below the limit of detection for the instrumentation.

A Nicolet Magna 550 FTIR spectrometer serves as the source for the infrared beam. The chamber has two KCl windows on either side of the gold surface to allow the

passage of the infrared light. The light is focused onto the gold mirror at a grazing angle of $\sim 84^\circ$ from the surface normal. After passing through the chamber the beam is detected using a mercury cadmium telluride (MCT-A) photoconductive detector.

For the introduction of gaseous species, custom glass manifolds are attached to four leak valves housed on the chamber. The manifolds are evacuated by individual rough pumps. Manifolds used for highly reactive gaseous species are equipped with liquid nitrogen traps and the attached rough pump is lubricated with fluorinated oil (Kurt J. Lesker, TKO W/7 Ultra) to preserve the integrity of the manifold and the gas species. The quality of each manifold and gas species is regularly checked using the chamber's mass spectrometer.

7.3 Operation of the Knudsen Cell Flow Reactor

The use and development of the Knudsen flow reactor was pioneered by Golden, Spokes, and Benson in the 1970's (Golden, 1973). The reactor utilizes the principle of molecular effusion demonstrated by Martin Knudsen in the early 1900's. Originally, the device was used to study gas phase reactions, but Golden and coworkers soon applied the operation of the Knudsen cell for the study of heterogeneous reactions. Knudsen cells operate at very low pressure, within the kinetic regime. Gas phase molecular collisions are minimal, as the mean free path of the gas is often greater than the distance between the chamber walls. In the kinetic regime the flow cell equilibrates rapidly and homogeneously, due to the free movement of the gas. In this regime data analysis is straightforward allowing accurate determination reaction kinetics.

As described in Chapter 2.2, the flow reactor has a drilled escape orifice that lies just above a turbomolecular pump. The surface area of the escape is calibrated in the

following manner. The flow through the chamber in the kinetic regime can be calculated by

$$F_h = \frac{P}{\sqrt{2\pi mkT}} A_h, \quad (2.1)$$

where F_h is the flow in molecules s^{-1} exiting the chamber through the hole, P is the chamber pressure, m is the mass of the molecule, k is Boltzmann's constant, T is the temperature of the gas, and A_h is the surface area of the escape orifice. The pressure in the chamber is determined by the instrumentation. At steady pressure, the flow into the chamber equals the flow out of the chamber. To determine the flow into the chamber, a manifold of known volume is used. Gas is introduced from the manifold into the chamber using a leak valve. By measuring the pressure change in the manifold the flow of molecules into the chamber can be calculated using the ideal gas law. The flow is then plotted versus the chamber pressure, and as can be seen from Equation 2.1 the slope of the plot, along with the known constants yields the area of the escape orifice.

Primarily, the Knudsen flow reactor is used to determine the uptake probability, γ , of a gas to a condensed substrate on the gold mirror. The uptake probability is defined as

$$\gamma = \frac{\# \text{ of molecules reacting with the surface}}{\# \text{ of molecules colliding with the surface}}. \quad (2.2)$$

To determine the uptake probability, the leak valves are used to establish a steady pressure of gas in the chamber with the cup closed, isolating the surface from the chamber. Under steady state conditions the change in the number of molecules in the chamber, N_0 , is zero; therefore, the flow into the chamber, F_{in} , is equal to the flow out F_h :

$$0 = \frac{dN_0}{dt} = F_{in} - F_h. \quad (2.3)$$

Equation 2.1 can be used to calculate the flow out, and through substitution and rearranging of Equation 2.3 yields,

$$F_{in} = \frac{P_0}{\sqrt{2\pi mkT}} A_h, \quad (2.4)$$

where P_0 is the initial steady state pressure. When the cup is retracted, the surface is exposed to the chamber atmosphere. If there is uptake to the surface the number of molecules in the chamber will decrease as they are lost to the surface. A new steady state is established

$$0 = \frac{dN_r}{dt} = F_{in} - F_h - F_s, \quad (2.5)$$

where N_r is the number of molecules after opening the cup and F_s is the flow to the surface. Rearranging,

$$F_{in} = F_h + F_s. \quad (2.6)$$

The flow into the chamber, F_{in} , remains unchanged after opening the cup. The flow out of the escape orifice and to the surface can also be determined by Equation 2.1, with the inclusion of the uptake probability for the flow to the surface. Substituting in to Equation 2.6 yields

$$\frac{P_0}{\sqrt{2\pi mkT}} A_h = \frac{P_r}{\sqrt{2\pi mkT}} A_h + \gamma \frac{P_r}{\sqrt{2\pi mkT}} A_s, \quad (2.7)$$

where γ is the uptake probability, and P_r as the pressure after retracting the cup. Solving for γ yields:

$$\gamma = \frac{A_h (P_0 - P_r)}{A_s P_r}. \quad (2.8)$$

Since the ratio of the pressure with and without the reactive surface is what is required to calculate γ , any value proportional to the pressure can be used. In general, for this thesis the mass spectrometer signal is used in the calculation which leads to

$$\gamma = \frac{A_h (S_0 - S_r)}{A_s S_r}, \quad (2.9)$$

where S_0 and S_r is the signal before and after exposure of the reactive surface respectively.

7.4 Interpretation of Knudsen Reactor Data

As described in the previous section, experimental kinetic data is acquired by establishing a steady state flow through the cell with the surface isolated from the chamber. When the cup is retracted, four trends in the mass spectrometer signal are generally observed: No change in signal, uptake with recovery to the original signal, uptake with partial recovery to the original signal, and continuous uptake without recovery. Presented in this chapter is a succinct description of gas/condensed phase kinetics necessary for the understanding of the experiments presented in the thesis (Danckwerts, 1970; Finlayson-Pitts and Pitts, 1999; Seinfeld and Pandis, 2000; Oura, 2003), and is not intended as a complete description of the complex field of surface chemistry. For each uptake regime, multiple physical phenomena could be occurring. The following paragraphs describe typical mechanisms responsible for the uptake trends. Confirmation of the uptake mechanism requires confirmation by complementary experimental techniques.

When the cup is retracted and the signal remains unchanged as shown in Figure 2.2A, two phenomena are possible. First, there is not any uptake to the surface, or uptake

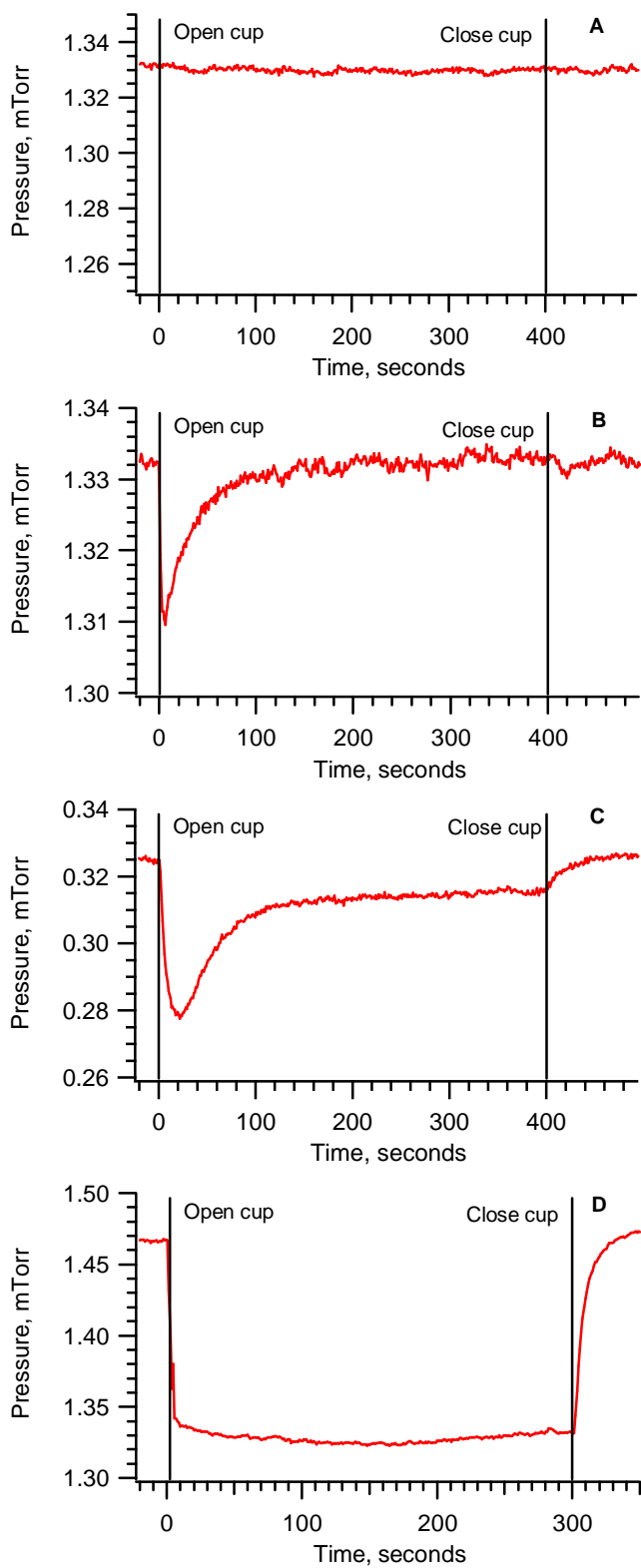


Figure 2.2. Example uptake plots for the Knudsen Cell. **A.** No change in signal. **B.** Uptake with full recovery. **C.** Uptake with partial recovery. **D.** Uptake without recovery.

is below the limit of detection for the system ($\gamma < 10^{-5}$). Second, the condensed phase could be in equilibrium with the gas phase. A straightforward example would be exposing ice to water vapor at its saturation vapor pressure. In this scenario, while no change is observed, there is exchange between the condensed and vapor phase. Performing an experiment either above or below the saturation vapor pressure can confirm the hypothesis. Above the saturation pressure the signal will decrease, and growth of the condensed phase can be confirmed by the FTIR-RAS. Below the saturation pressure, the signal will increase and desorption of the substrate will also be visible spectroscopically.

Uptake with full recovery is when the signal decreases to a minima and then recovers to its original level upon retracting of the cup as shown in Figure 2.2B. Typically, uptake with recovery can be explained by two phenomena. First, the uptake could be only to the surface of the substrate; a monolayer or Langmuir type uptake. When the surface is first exposed to the chamber atmosphere the uptake is rapid because the surface sites are unoccupied. As the experiment progresses, more sites become occupied and signal decreases. When either the entire surface is occupied by a monolayer of the gas or equilibrium is reached between desorption and adsorption of the gas, the signal returns to the original level. Secondly, the uptake can represent the solubility of a gas phase species in the condensed phase. Initially, the condensed phase is free of the species and uptake occurs rapidly. As the condensed phase nears saturation, the signal decreases until and equilibrium is established. The equilibrium between the vapor phase and condensed phase is described by Henry's law:

$$[X] = H_x P_x, \quad (2.10)$$

where $[X]$ is the equilibrium concentration of X in solution, P_X is the gas phases pressure, and H_X is the Henry's law constant. Knowledge of the system under study allows interpretation of the data, if the condensed phase is liquid, it is likely uptake with recovery is attributed to Henry's Law, if the condensed phase is solid and < 1 monolayer is observed to uptake to the film it is likely this is a monolayer type surface uptake.

Uptake with partial recovery, as shown in Figure 2.2C is indicative of either a multilayer uptake or solubility of the molecules with reaction in the condensed phase. For the multilayer uptake, the gas "sticks" to the bare substrate with a higher efficiency than on itself. Upon initial opening of the cup the unoccupied sites in the substrate are occupied. As time progresses, these sites become filled and a multilayer uptake occurs, albeit less efficiently on the condensed molecules from the gas phase. For uptake governed by solubility with reaction, uptake initially occurs as described in the previous section as the gas reaches saturation and equilibrium with the gas phase. However, because there is a reaction in the condensed phase the signal recovers only partially. As reaction consumes molecules in the aqueous phase, uptake continues to maintain the Henry's law equilibrium.

Uptake without recovery as shown in Figure 2.2D is generally also due to two processes: either multilayer uptake or uptake with a fast reaction. A straightforward example of multilayer uptake is the growth of ice when the gas phase pressure exceeds the vapor pressure of the condensed ice. For uptake with a fast reaction, the soluble species does not reach a Henry's law equilibrium as the reaction occurs faster than diffusion through the condensed solution, or the reaction occurs directly on the surface

region. The reaction product(s) can desorb into the gas phase or be absorbed into the condensed phase.

In summary, the uptake measured by the Knudsen cell gives accurate kinetics of the uptake, and from the observed kinetic regime, clues can be deduced as to the mechanism responsible for the uptake. Additional information is required to confirm the mechanism. The FTIR-RAS can generally provide the required information.

7.5 Fourier Transform Infrared Reflectance Absorbance Spectroscopy

FTIR-RAS, also referenced in the literature as reflectance absorbance infrared spectroscopy (RAIRS), offers a significant improvement in sensitivity compared to traditional transmission infrared spectroscopy. The technique was originally developed by Robert Greenler for the study of mono and sub-monolayer study of gas absorbed on metal substrates (Greenler, 1966), but has since been applied to the study of many heterogeneous processes. The increased sensitivity is due to two effects. First, the reflection of light off the metal surface creates a localized standing electric field. Second, the free electrons of the metal create an image dipole increasing the strength of the oscillations in the absorbed layer. Since both of the enhancements are localized at the surface, the enhancements are greatest when the film is sufficiently thin.

When light reflects off a surface, the incident and reflected waves combine to form a standing electric field. Light reflected from a surface at near normal incidence is phase shifted $\sim 180^\circ$; therefore, near the surface the reflected and incident waves cancel each other, creating a weak electric field. For infrared light ranging between 4000 cm^{-1} to 600 cm^{-1} the distance from the node at the surface to the first anti-node would be between

0.625 to 4.17 μm from the surface, making it very difficult to detect molecules near the surface.

When the angle of incidence is increased from normal to the surface the phase shift changes depending on the polarization. For light polarized perpendicular to the surface the phase shift remains near 180° for all angles; however, for light polarized parallel to the surface the phase shift is highly dependent on the angle. For angles of incidence between 0° and 60° the phase change is $\sim 30^\circ$. Between 60° and 90° the phase changes rapidly from $\sim 60^\circ$ to a full 180° . At angles between 80° to 88° the phase change is approximately 90° . For a phase change of 90° the incident and reflective waves constructively interfere at the surface, creating an elliptical standing wave with a magnitude double that of the incoming radiation. Doubling the magnitude translates into a four fold increase in field intensity. For isotropic films vibrations orientated perpendicular to the surface will be fully enhanced, while vibrations parallel to the surface will be less strongly enhanced by the field.

As molecules near the metal surface absorb radiation they begin to oscillate. The oscillation creates a dipole moment, and the free electrons in the gold respond by creating an image dipole. If the dipole created by the oscillation is parallel to the surface, the image dipole in the metal is orientated in the opposite direction, which truncates the oscillation. When the dipole is perpendicular to the surface, the image dipole enhances the oscillation. The extent of the enhancement is dependent both on the imaginary refractive index of the metal, k , and the angle of incidence of incoming light, ϕ , with greater values of k and ϕ resulting in increased enhancement.

For thin films the combined enhancements translate into an increased sensitivity by a factor of ~ 25 over transmission spectroscopy. However, once films grow beyond ~ 500 nm, the absorbance is observed to decrease with film thickness (Zondlo, 1997). As thickness increases, the standing field decreases in magnitude as the light is absorbed before it reflects off the surface. Also, as the molecules move farther from the surface, they no longer “feel” the image dipole, and vibrations parallel to the surface become visible while vibrations perpendicular become significantly less enhanced. The decrease in absorption by reducing the surface enhancements is greater than the Beer’s law increase in absorption gained by thicker film. When the film becomes sufficiently thick destructive interference patterns appear as the path length of the light through the film and the light reflected off the surface film differ by half a wavelength. While interference patterns can distort the spectra making interpretation difficult, they can be useful in determining to the thickness of the film. Perpendicular polarized light has a phase change upon reflection at the surface and metal, using geometry the thickness of the film can be determined by the destructive interference maxima by

$$d = \frac{(m + 1/2)\lambda}{2 \left[\frac{n_2}{\cos(\phi_2)} - n_1 \sin(\phi_1) \tan(\phi_2) \right]}, \quad (2.11)$$

where d is the film thickness, n is the refractive index, ϕ is the angle of incidence, λ is the wavelength of light, m is an integer, and the subscripts 1 and 2 refer to the vacuum and the film respectively (Robinson, 1999). For parallel polarized light at high angles of incidence the equation is similar, with the numerator simply $m\lambda$, as there is not a phase change for light reflected from the surface.

For isotropic films, FTIR-RAS spectra differ from transmission spectra as the orientation of the vibration determines the extent of the enhancement and for all media there is a red shift in the absorption maxima. FTIR-RAS is sensitive to changes in the real refractive index, n , of the absorbed film. Across absorption bands there is typically a decrease in the refractive index on the red (near) side of the band followed by an increase on blue (far) side of the band. As dictated by Snell's law, a decrease in the refractive index of the film corresponds to an increase in the angle of incidence with the metal surface. The increased angle causes an increased enhancement at these wavelengths, as described above. As a result, when FTIR-RAS is compared to traditional transmission spectra, the absorbance peaks are typically red shifted by $\sim 4 \text{ cm}^{-1}$, and peak structure can change because of the effect of the real refractive index on the absorption. The unique effects must be taken into consideration when comparing FTIR-RAS spectra to traditional transmission spectra.

Chapter III

8 Reaction of Isoprene on Thin Sulfuric Acid Films: Kinetics, Uptake, and Product Analysis

8.1 Introduction

Sulfates, both natural and anthropogenic, have been identified as important components of the tropospheric aerosol and gaseous sulfuric acid has been linked to new particle formation events (Bonn, 2008; Kulmala, 2008). Additionally, a key finding in the last decade is that almost all tropospheric sulfate particles, including ultrafine (< 10 nm) particles, are internal mixtures of many components, with organics comprising up to 80% of the particle mass (Middlebrook, 1998; Kalberer, 2004; Cottrel, 2008). However, some model predictions of SOA formation fall well short of the observed field data (Griffin, 2002; Heald, 2005; Volkamer, 2006). Smog chamber studies suggest that inorganic acids catalyze carbonyl heterogeneous reactions leading to an increase in secondary organic aerosol production (Jang, 2002). Additional smog chamber research has investigated sulfuric acid-catalyzed SOA formation of anthropogenic and biogenic carbonyls (Claeys, 2004A & B; Keywood, 2004A & B; Gao, 2004A & B; Edney 2005; Kroll, 2005A & B; Borge, 2006; Ervens, 2007; Liggio, 2007 & 2008; Ng, 2007; Surratt, 2007). However the mechanisms, products, and kinetics of acid-catalyzed heterogeneous SOA formation pathways are still poorly understood. Thus the atmospheric significance of this SOA formation mechanism is uncertain.

Emissions of isoprene account for approximately 50% of the global volatile organic carbon (VOC) budget, with recent estimates between 500-750 Tg yr⁻¹ (Guenther, 2006). Due to isoprene's high vapor pressure of 550 Torr at 298K and low Henry's law constant of 0.02 M atm⁻¹, gas phase oxidation pathways are assumed to be the only

relevant mechanisms for isoprene degradation (Mackay, 1981)). However, direct polymerization of isoprene on existing sulfuric acid particles in the absence of gas phase oxidants and photochemistry has been observed in smog chamber experiments (Liggio, 2007). In those studies isoprene uptake involved polymerization of isoprene into various dimers, trimers, and higher ordered oligomers. However, the manuscript calculates an equilibrium partitioning for isoprene to the condensed phase which does not take the kinetics of the process into account. Without fundamental kinetic data it is difficult to determine the significance of the observed uptake.

Polymerization of isoprene into dimers and trimers would form compounds similar in structure to naturally emitted monoterpenes and sesquiterpenes. Monoterpenes, sesquiterpenes and higher order terpenes are emitted through biogenically controlled isoprene polymerization within the emitting species. Recently, it has been proposed that these terpenes may play an important role in atmospheric chemistry. For example, new particle formation events in forested environments have been linked to the formation of stabilized Crige intermediates from sesquiterpene/ozone reactions (Bonn, 2008). Additionally, a field study has found that increases in ambient sesquiterpene concentration correlate to nucleation events. The source of the increase remains unclear. If acid catalyzed production of mono and sesquiterpene like compounds from isoprene is efficient it could compete with the biogenic sources, especially during nucleation events.

In the present study isoprene uptake was measured using a high vacuum Knudsen cell flow reactor and a gas IR cell as a function of sulfuric acid wt%, temperature, and pressure of isoprene. Uptake probabilities were determined and the potential SOA formed with respect to heterogeneous acid catalyzed reactions was estimated. In addition, bulk

reactions of sulfuric acid and isoprene were studied and the products were analyzed using GC/MS. Together these experiments imply that direct isoprene uptake will not produce significant SOA; however, terpene production from the small uptake may be relevant for ultrafine particles and could affect growth and nucleation.

8.2 Experimental Procedure

8.2.1 Knudsen Cell

A schematic of the high vacuum Knudsen cell used in these studies is shown in Figure 2.1. This apparatus has been described in detail in Chapter 2. A method for the production of optically flat sulfuric acid films has previously been reported (Middlebrook, 1993). Initially, a thin film of ice is deposited on the gold substrate, followed by deposition of SO_3 to the ice substrate at 130 K. A second thin film of ice is then deposited on top of the SO_3 . Finally, the mixed film is warmed slowly (5 K min^{-1}) to $\sim 215 \text{ K}$ and liquid sulfuric acid forms on the substrate. Sulfuric acid wt% ranging from 78 to 93 wt% is controlled by establishing a steady state flow of water vapor over the film. Higher water pressures required to generate a film less than 78 wt% H_2SO_4 were not obtainable due to the operational limitations of the Knudsen cell. The wt% sulfuric acid is determined by pressure of water in the chamber and the temperature of the film (Gmitro and Vermeulen, 1964).

After the sulfuric acid films have been prepared, the Teflon cup is used to isolate the film from the chamber. Isoprene (Aldrich, 99%) is introduced into the chamber and monitored using an electron impact ionization/quadrupole mass spectrometer (MS) tuned to 67 m/z . The flow is adjusted until the desired concentration ($10^{-6} - 10^{-4} \text{ Torr}$) is

reached and the signal becomes stable. After stable conditions are achieved, the cup is retracted to expose the isoprene to the sulfuric acid film. A decrease in the signal from the MS corresponds to uptake by the substrate. The Knudsen effusion relation is then used to determine the uptake probability, γ ,

$$\gamma = \frac{A_h(S_0 - S)}{A_s S} \quad (3.1)$$

where S_0 is the initial MS signal, S is the signal after cup is opened, A_h is the area of the escape orifice (0.19 cm^2) and A_s is the surface area of the sample (5.1 cm^2). The FTIR-RAS is used to confirm the composition (wt% H_2SO_4) and state (solid, liquid) of the substrate. It is also used to identify any condensed phase products that form as a result of the reaction.

8.2.2 Infrared Gas Cell

Knudsen Cell experiments were performed at sulfuric acid concentrations greater than 78 wt%. We were not able to generate more dilute samples because the pressures of H_2O required at warmer temperatures were greater the operational limits of the apparatus. Cooling the films to lower temperatures to lower the vapor pressure was not possible as the condensed phase would freeze at 78 wt%. We thus used a glass cell (11-cm path length, 99.6 mL in volume) with KCl windows to study isoprene uptake on sulfuric acid solutions ranging from 60 to 85 wt% sulfuric acid. The cell had a removable “cup” for holding the liquid sulfuric acid. The gas phase of the cell was monitored using the Nicolet Magna 550 FTIR spectrometer. For calibration, isoprene was introduced to the cell through a manifold at pressures between 0.1 – 50 Torr (determined by a capacitance manometer) and the spectra recorded. For uptake measurements, ~ 1 mL sulfuric acid

solution was placed into the cup both with and without stirring. The cell was gently “pumped” by opening it to an evacuated trap of equal volume 12 times, dropping the background cell pressure to < 500 mTorr with most of the remaining gas being water vapor and CO₂. For the 60 wt% sulfuric acid sample, which has the highest water vapor pressure, this technique would remove an insignificant 0.0020 g of water from the 1.5 g sample. Then, 2 to 5 Torr of isoprene was introduced into the cell and the pressure loss was monitored by infrared spectrometry at 2 second intervals.

8.2.3 Gas Chromatography/Mass Spectroscopy

In addition to the FTIR-RAS data for product analysis, bulk experiments were performed. To analyze the products formed inside the Knudsen Cell, the film was removed from the flow reactor after an uptake experiment and the products were analyzed using gas-chromatography/mass spectroscopy (GC/MS). The chamber films were extracted by filling the chamber with argon after 2 hours of isoprene uptake on the sulfuric acid film using $\sim 10^{-5}$ Torr isoprene. The stainless steel housing holding the cryostat and surface was detached from the Knudsen cell and a thin layer (100 μ L) of methylene chloride (Aldrich, 99.8%) was placed on the film and covered. After 5 minutes, the remaining methylene chloride mixture was extracted using a glass capillary. The needle of a gas tight syringe was inserted directly into the capillary and the methylene chloride sample was analyzed using GC/MS.

The above experiments were compared to experiments at higher isoprene pressures (3 - 4 Torr) where bulk mixtures of sulfuric acid were reacted with isoprene using a manifold. Here, 1-2 ml of 85 wt% sulfuric acid was degassed using freeze-pump-thaw cycles until the pressure in the manifold was equal to the calculated pressure of

water vapor above 85 wt% sulfuric acid. The manifold was then sealed from the sulfuric acid and pumped down to 5 mTorr. Then ~ 5 Torr of isoprene was introduced into the manifold and sealed from the pump. The valve isolating the sulfuric acid from the gaseous isoprene was opened, and after an initial expansion (reducing the pressure to 3 - 4 Torr) a continuous drop in pressure was observed in addition to a color change of the condensed phase from clear to yellow. The uptake process was repeated four times to ensure the organic mass concentration in the bulk sample was sufficient for further analysis.

After the bulk uptake, three methods of GC/MS product analysis were employed; solvent extraction, solvent extraction with derivatization to test for hydroxyl functional groups, and headspace analysis. For all methods, the sulfuric acid vessel was removed from the manifold and opened under argon. For the solvent extractions, 1 mL methylene chloride was added to the organic/sulfuric acid mixture and swirled. The methylene chloride layer was then extracted and sealed in a vial for immediate analysis (less than 30 minutes) using GC/MS. Control vials consisting of only methylene chloride exposed to sulfuric acid were also prepared and analyzed to ensure product peaks were not due to the solvent. For the derivatized samples, 0.5 mL of N-Methyl-N-trimethylsilyltrifluoroacetamide with 1% trimethylchlorosilane (MSTFA + 1% TMCS, Thermo Scientific) was added to the dry methylene chloride and allowed to react at 50 °C for 10 minutes, then analyzed with the GC/MS. For headspace analysis, an 85 wt% H₂SO₄ bulk sample was placed into a 50 mL bottle fitted with a silicon septa and sealed under nitrogen. Headspace samples were extracted using a 10 mL gas tight syringe and injected directly into the GC/MS. Then the same sample was placed in an ice bath and

slowly diluted with distilled water to a sulfuric acid concentration of ~ 50 wt%, from which a second 10 mL headspace sample was analyzed.

A Finnigan trace GC ultra equipped with a Zebron ZB-5mS capillary column (95% dimethylpolysiloxane & 5% phenylarylene, 30 m x 0.25 mm x 0.25 μm) was used for separations and mass spectra were obtained with a Polaris Q ion trap detector (ThermoFinnigan, San Jose, CA). The helium carrier gas flow rate was 1.0 mL min^{-1} for all separations. Because thermal degradation of the products was a possibility, the programmed temperature vaporization (PTV) injection technique was employed for the liquid samples. Immediately following sample injection (splitless) the injector temperature was ramped from 50 $^{\circ}\text{C}$ to 280 $^{\circ}\text{C}$ at ~ 20 $^{\circ}\text{C min}^{-1}$. The initial column temperature was 40 $^{\circ}\text{C}$ which was held for 5 minutes, ramped to 200 $^{\circ}\text{C}$ at 3 $^{\circ}\text{C min}^{-1}$, held for 2 min, ramped to 310 $^{\circ}\text{C}$ at 30 $^{\circ}\text{C min}^{-1}$ and then held for 1 minute. The headspace analysis was performed without PTV with the injector at 150 $^{\circ}\text{C}$. For all experiments, the EI-Ion trap mass spectrometer collected ions from 30-650 m/z .

8.3 Results and Discussion

8.3.1 Kinetics: Knudsen Cell

Isoprene uptake on sulfuric acid was studied in a Knudsen cell as a function of temperature (220 – 265 K), pressure (10^{-7} – 10^{-5} Torr), and wt% sulfuric acid (78 – 93 wt%). Figure 3.1 shows results for a typical isoprene uptake experiment on a blank gold surface (A), solid sulfuric acid tetrahydrate (B) and liquid sulfuric acid (C). As can be seen in panels A and B, uptake was not observed on either the gold substrate or solid sulfuric acid films. However, on liquid sulfuric acid films uptake is observed. The MS

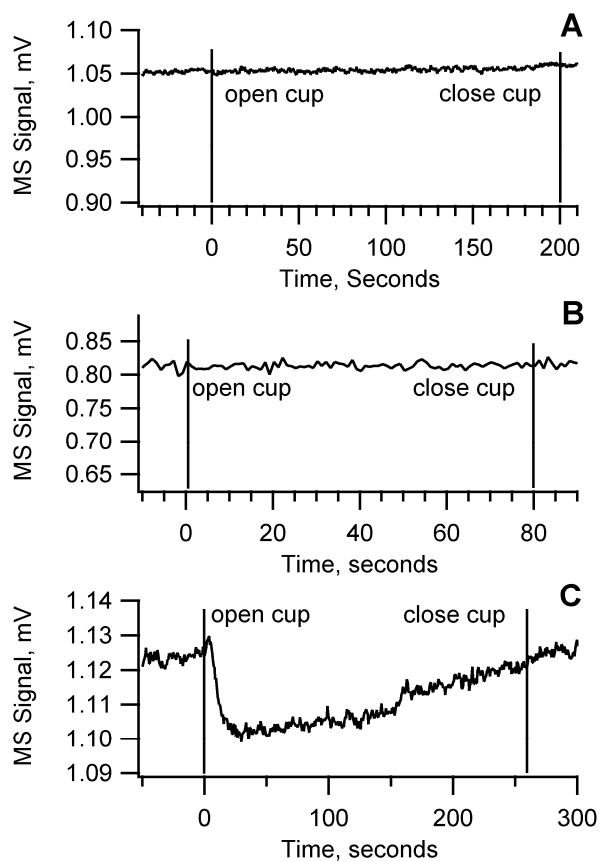


Figure 3.1. Isoprene uptake experiments performed at 1×10^{-5} Torr isoprene. “Open cup” indicates when film was exposed to isoprene, “Close Cup” indicates isolation of film from the chamber. The plot A is isoprene exposed to the bare gold surface at 220K. Plot B is isoprene exposed to a frozen sulfuric acid tetrahydrate film at 220K. Plot C is isoprene exposed to 89 wt% sulfuric acid at 260K.

signal drops initially with partial recovery. Equation 3.1 is used to determine the initial uptake probability, γ_i , the maximum uptake shortly after opening the cup. At a constant wt% H_2SO_4 γ_i values did not deviate significantly with either temperature or pressure of isoprene. However, Figure 3.2 shows γ_i as a function of sulfuric acid wt%. Here it can be seen that γ_i increases with increasing wt% sulfuric acid from 78 – 93 wt% H_2SO_4 .

For each uptake experiment, uptake continued for the entire time the cup was open, with γ decreasing from 10^{-4} to less than 10^{-5} and then remaining constant until the cup was closed. Additionally, after each experiment the chamber was pumped free of isoprene with the cup closed. When the cup is reopened there is no change in signal, indicating isoprene does not desorb from the film isothermally or at fixed relative humidity. These observations coupled with the absence of either a pressure or temperature dependence for uptake is consistent with polymerization reactions. Polymerization reactions for alkenes are expected to have a small activation barrier and large rate constant (Gehlawat, 1964; Brilman, 1997; Odian, 2004). The increase of γ_i as a function of sulfuric acid wt% indicates the reaction is likely acid catalyzed.

8.3.2 Kinetics: Gas Cell

To determine whether uptake of isoprene on sulfuric acid would occur below the 78 wt% limit of the Knudsen Cell, a gas IR cell was utilized. The cell had a small “cup” for the condensed phase acid which ranged from 60 to 85 wt% held at 293 K, and pressures of isoprene between 1 and 4 Torr were introduced into the cell. Figure 3.3 shows plots of $\ln(P_{\text{isoprene}}/P_o)$ versus time in seconds. For all experiments the log plot was linear (lowest $R^2 = 0.95$) and the first order loss rate calculated by the slope of the

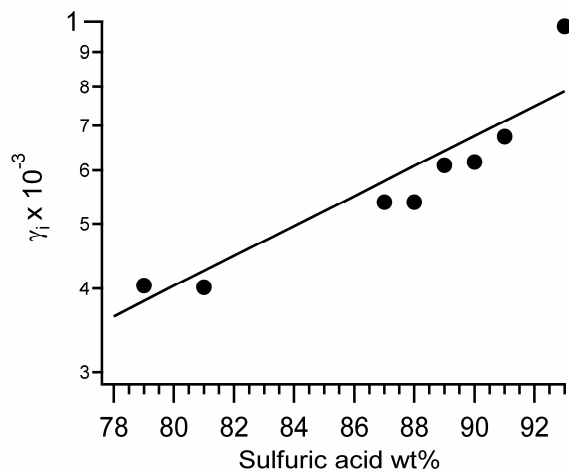


Figure 3.2 A plot of the initial reactive uptake coefficient, γ_i , as a function of sulfuric acid wt% for the Knudsen Cell with best fit ($R^2 = 0.86$). The line serves only as an empirical fit to the data.

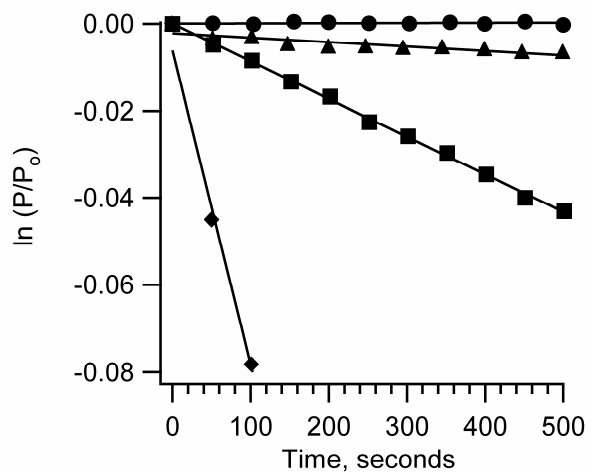


Figure 3.3 Plots of $\ln(P/P_0)$ vs time for the static IR gas cell study. Black diamonds are for 85 wt% H₂SO₄, squares are for 75 wt% H₂SO₄, and triangles are for 60 wt% H₂SO₄. Black circles are a control experiment.

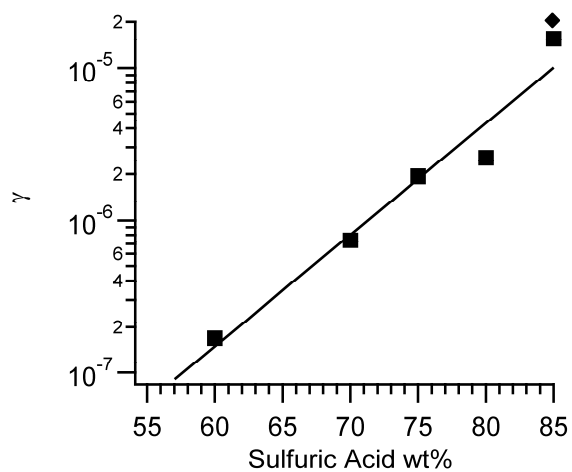


Figure 3.4. A plot of the steady state reactive uptake coefficient, γ_{ss} , vs wt% H_2SO_4 for the IR gas cell experiments (squares) and from the 2 hour uptake performed in the Knudsen cell at the closing of the cup (diamond).

plot did not indicate changes with initial pressure. As with the Knudsen Cell uptake, increased sulfuric acid wt% results in an increase of isoprene uptake rate. If we assume that the uptake was not limited by gas phase diffusion as isoprene pressures were greater than that of water, then γ can be calculated from the first order gas phase loss rate, k_{gas} in s^{-1} , by,

$$\gamma = \frac{4k_{gas}V_{cell}}{\langle v \rangle SA}, \quad (3.2)$$

where V_{cell} , $\langle v \rangle$, and SA are the volume of the gas cell, the mean molecular speed, and the surface area of the condensed phase, respectively. For the gas cell, γ values range from 10^{-7} to 10^{-5} for 60 to 85 wt% H_2SO_4 as shown in Figure 3.4. Also in Figure 3.4 is the γ value prior to closing the cup in the Knudsen Cell experiment after the long 2 hour uptake. The value from the gas cell is consistent with the Knudsen cell value after the initial fast uptake regime.

8.3.3 Product Analysis: GC/MS

To determine products of the uptake, bulk experiments were performed. To ensure products were due to isoprene reactions with the sulfuric acid, a blank was prepared. First, methylene chloride was added to 85 wt% sulfuric acid and the resulting gas chromatogram was the same as for stock methylene chloride. For the sulfuric acid bulk samples, assuming all pressure loss in the manifold was due to uptake, an estimated ~ 0.002 grams of isoprene (four uptake cycles) was absorbed in 1 mL sulfuric acid at isoprene pressure of 3-4 Torr at 293 K. The extracted products were analyzed using GC/MS. A typical chromatogram from the bulk study is shown in Figure 3.5A. The

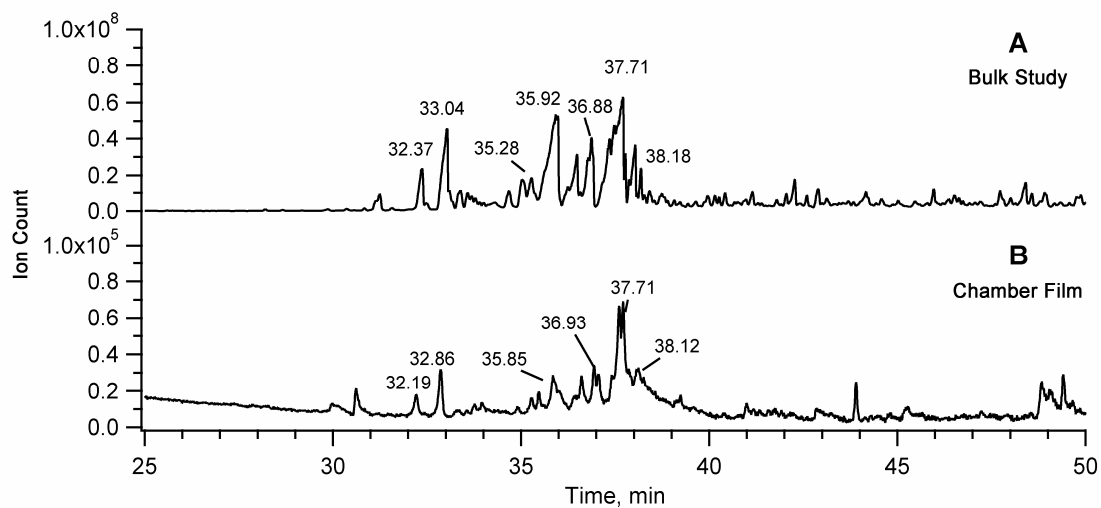


Figure 3.5. Chromatograms from bulk study and chamber film extract of isoprene uptake on 85 wt% sulfuric acid. A. Chromatogram of 4 Torr isoprene bulk uptake at 293 K. B. Chromatogram of 1×10^{-5} Torr isoprene chamber uptake at 260 K.

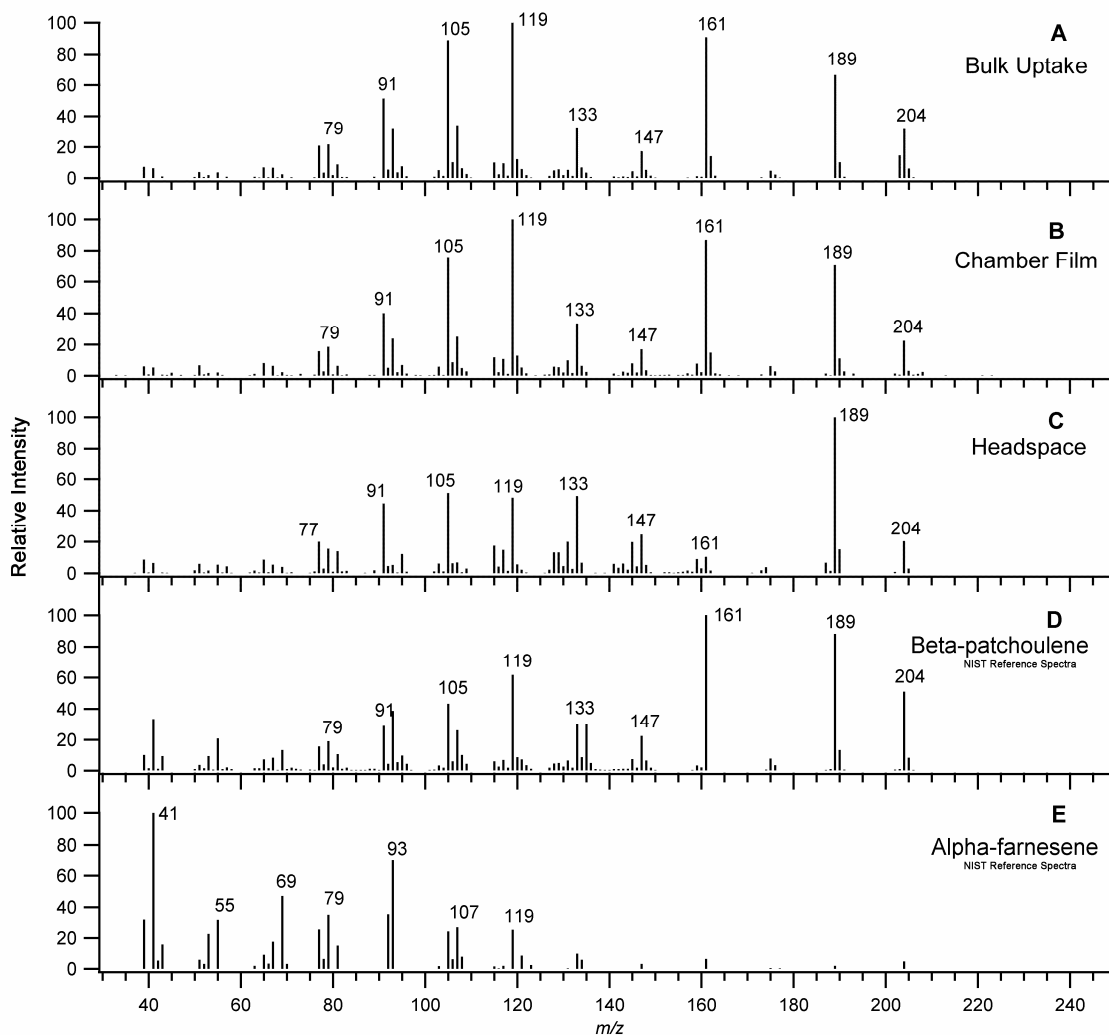


Figure 3.6. Mass spectra of uptake experiments performed on 85 wt% sulfuric acid. A. Chromatogram peak at 33.04 minutes for a bulk 4 Torr isoprene uptake at 293 K. B. Peak at 32.86 minutes from a chamber film extract for a two hour 1.0×10^{-5} Torr isoprene uptake at 260 K. C. Peak at 33.07 minutes for headspace gas analysis after a 4 Torr isoprene uptake on 85 wt% sulfuric acid solution was diluted to 50 wt%. D and E. NIST Reference spectra for a beta-patchoulene, a polycyclic sesquiterpene, and alpha-farnesene, a linear sesquiterpene, respectively.

chromatogram identifies a significant number of reaction products eluting from the column indicating many reaction pathways. Mass spectra for each individual GC peak labeled in Figure 3.5 contain fragments greater than the single isoprene skeleton, confirming that polymerization is occurring. The individual spectra for each major GC peak were very similar, with the greatest intensities at 91, 93, 105, 107, 119, 131, 133, 135, 147, 161, 189, and 204 m/z . The mass spectrum of the peak at 33.04 minutes from Figure 3.5A is shown in Figure 3.6A, and is typical of the other chromatography peaks. The peak at 204 m/z is consistent with a molecular ion of an isoprene trimer. Also, the spectral pattern is not consistent with linear or “chain” cationic polymerization of isoprene with hydroxyl or sulfate termination. For example, in a linear C_{15} chain, low mass peaks generally dominate the spectrum; however cyclic structures tend to have higher mass signatures (McLafferty, 1993). For comparison Figure 3.6 also displays NIST reference spectra for the cyclic sesquiterpene β -Patchoulene (panel D) and a linear $C_{15}H_{24}$ isoprene trimer α -farnensene (Panel E). Clearly, the cyclic sesquiterpene is a closer match than the linear trimer.

Comparisons to the NIST spectral database did not produce ideal matches, but the “best” match was generally a polycyclic sesquiterpene. However, sesquiterpenes and sesquiterpenols can have similar mass spectra as they only vary by a hydroxyl group and hydrogen added across a double bond. Hydroxyl groups bonded to cyclic structures tend to “steal” hydrogen from elsewhere on the ring during ionization and then fragment as a neutral water molecule and a $[M^+ - H_2O]$ fragment (McLafferty, 1993). To test for hydroxyl groups, the derivatization agent N-methyl-N-(trimethylsilyl) trifluoroacetamide (MTSFA) was added to methylene chloride samples. If hydroxyl groups are present the

hydrogen bonded to oxygen would be replaced by a trimethylsilyl group significantly changing both the chromatogram and individual mass spectra. No significant changes were noted in either the chromatogram or mass spectra, indicating hydroxyl groups were not present in the solvent extracts.

To test whether the observed polymerization was pressure dependent as the pressures used in the bulk study were significantly greater than in the Knudsen cell, a 2 hour isoprene uptake was performed in the Knudsen cell on an 85 wt% sulfuric acid film at an isoprene pressure of 1×10^{-5} Torr. The chromatogram of the extracted products is illustrated in Figure 3.5B. The chromatograms in Figure 3.5A and B are similar, with the largest difference being slight differences in retention times. This difference is likely due to variability in the manual temperature ramp of the injector. Figure 3.6B is a typical mass spectrum for the chamber extraction which is also very similar to the extracts from the bulk study in Figure 3.6A.

To test the effects that water uptake may have on sulfuric acid particles that were previously exposed to isoprene, a headspace analysis of a bulk sample was performed. The chromatograms for the gas phase above the initial 85 wt% sulfuric acid solution showed very low signals. In contrast, upon dilution to 50% sulfuric acid solution, an increase of ~ 2 orders of magnitude in gas phase products was observed. The spectra for the sesquiterpene peak at 33.07 minutes is shown in Figure 3.6C, very similar to bulk uptake and chamber film shown in Figure 3.6A & B. It is clear that the addition of water to the sulfuric acid causes the isoprene products to partition back into the gas phase. It is likely that equilibrium exists between the terpene product and its cation, and the addition of water drives the reaction to favor the terpene, which then partitions into the gas phase.

8.4 Atmospheric Implications

To determine the significance of the isoprene uptake by sulfuric acid, we will use the heterogeneous rate constant, k_{het} , which can be estimated in the kinetic regime by

$$k_{het} = \gamma \langle v \rangle SA / 4, \quad (3.3)$$

where γ is the uptake coefficient, $\langle v \rangle$ is the mean molecular speed, and SA is particle surface area per unit volume. Even at a low relative humidity of 20%, a pure sulfuric acid particle would be 60 wt% H_2SO_4 (Clegg, 1998). Using the steady state γ_{ss} of 10^{-7} at 60 wt% H_2SO_4 from the gas cell and a large particle surface area of $1 \times 10^{-6} \text{ cm}^2/\text{cm}^3$, $k_{het} = 7.6 \times 10^{-10} \text{ s}^{-1}$. The lifetime, τ , of isoprene with respect to heterogeneous loss would be 4 years. From a particle standpoint, a 100 nm particle exposed to a concentration of isoprene of 5 ppb for one 1 day at this acidity and surface area would gain only 0.03% product by mass. Alternatively, if we extrapolate an initial γ_i value from the Knudsen cell of 10^{-4} for 60 wt% H_2SO_4 from Figure 3 the lifetime of isoprene is then 14 days, and the particle would gain 6.8% product by mass. Because isoprene has a gas phase lifetime of ~ 3 hours, direct heterogeneous loss on sulfuric acid is not a significant sink for isoprene. Further, field studies indicate particles greater than 20 nm are significantly neutralized by ammonia, and the majority of the surface area used in the above calculation is due to particles greater than 20 nm (Cottrell, 2008). Therefore, heterogeneous acid catalyzed production of SOA directly from isoprene uptake onto sulfuric acid is unlikely to be important. Additionally, a recent field study a semi-rural environment in the south eastern United States, where isoprene and terpene emissions are high, did not find any correlation between particle acidity and SOA mass (Tanner, 2009).

While larger particles would not have significant acidity to make uptake of isoprene relevant, small and freshly nucleated particles are expected to be acidic. For example, a field study conducted in the Rocky Mountains estimated 10-75% of ultra-fine particle growth was due to sulfuric acid, suggesting these particles are quite acidic (Boy, 2008). Additionally, field measurements in forested regions do not show any correlation between ammonia concentration and particle nucleation and growth (Riipinen, 2007). Recently, a laboratory study confirmed that for concentrations of ammonia < 1ppbv, which is typical for a forested region, there is no enhancement to the nucleation rate over binary H₂SO₄ nucleation (Benson, 2009). This suggests that at low concentrations, ammonia may not play a significant role in particle formation and growth. If we assume particles less than 3 nm are not significantly neutralized, sulfuric acid particles ranging from 1 to 3 nm at 20% RH would be between 70 and 80 wt% H₂SO₄ (due to the Kelvin effect) (Willeke, 1980). If we consider a growing particle during a nucleation event, the uptake of isoprene would be

$$\frac{dN_{iso}}{dt} = n_{iso} \gamma < v > \pi (D_o + (GR)t)^2 / 4, \quad (3.4)$$

where N_{iso} , n_{iso} , D_o , and GR are the number of molecules of condensed isoprene products, the gas phase number density of isoprene (molecule cm⁻³), the initial sulfuric acid particle diameter (cm), and the growth rate (cm s⁻¹) respectively. Using a growth rate of 4 nm/hr from the Rocky Mountain field study (Boy, 2008), an initial diameter of 1 nm, 1 ppbv of isoprene, the lowest γ_i of 4×10^{-4} from the Knudsen Cell and integrating from 0 to 1800 seconds (the time for the particle to grow to 3 nm) the particle would take up ~ 21 molecules of isoprene. For the 3 nm particle this uptake corresponds to a coverage of 7.4×10^{13} molecules/cm² (~0.65 monolayers) and isoprene would compromise 9.1% of the

particle mass (assuming a density of 1.6 g/mL). However, if we again extrapolate a γ_i of 10^{-4} for a 60 wt% particle and allow the particle to grow from 1 to 20 nm, the uptake would be 1503 molecules of isoprene. Therefore heterogeneous chemistry could in part explain the ubiquitous presence of organics in ultrafine particles found in the atmosphere.

As these small particles grow to larger sizes the wt% H₂SO₄ will decrease, and based on the data presented here a fraction of the mono and sesquiterpenes will partition back into the gas phase. The sesquiterpene production can then be calculated by

$$P_{sqt} = \frac{\%Yield}{100} * J * \frac{N_{iso}}{3}, \quad (3.5)$$

where P_{sqt} is the production of sesquiterpenes in molecules cm⁻³ s⁻¹, J is the nucleation rate (4 particles cm⁻³ s⁻¹) from a field study, and N_{iso} is the number of molecules of isoprene per particle (Boy, 2008). A previous study of the products of acid catalyzed isoprene polymerization found a 40% sesquiterpene yield (Audisio, 1991), which is consistent with the organic mass loss reported when relative humidity is increased for terpenes (Liggio, 2008). The heterogeneous source contribution to gas phase concentration, [SQT], can be estimated by

$$[SQT] = \tau * P_{sqt}, \quad (3.6)$$

where τ is the lifetime for the sesquiterpenes. Sesquiterpene lifetimes vary significantly, with β -caryophyllene on the order of minutes, while α -cedrene is significantly longer with a lifetime of 2 hours (Shu and Atkinson, 1995). However, since β -caryophyllene has a unique 9 carbon ring, the lifetime of α -cedrene is assumed more representative of the sesquiterpenes formed by cationic polymerization. Using a lifetime of 2 hours we

estimate the production of sesquiterpenes via the heterogeneous reaction of isoprene could increase the gas phase sesquiterpene concentration by 6×10^6 molecules cm^{-3} .

In the gas phase it has been proposed that sesquiterpenes will react with ozone and stimulate additional particle nucleation (Bonn, 2008). A field study reported the average increase in gas phase sesquiterpene concentration for nucleation events near the test site was $\sim 10^8$ molecules cm^{-3} (Boy, 2008). Isoprene alone could explain 6% of this increase. In addition to isoprene, other similar molecules such as terpenes and isoprene degradation products may also be a source of sesquiterpenes or sesquiterpene like compounds. For example, mono and sesquiterpenes were also found to react on acidic particles and the products repartitioned to the gas phase upon increasing the relative humidity (Liggio, 2008). Heterogeneous polymerization processes previously considered of minor significance with respect to SOA formation should be reinvestigated as possible sources of sesquiterpene or sesquiterpene like gas phase compounds. A process involving organics may explain in part the discrepancy between the observed nucleation rates in the field ($1 \text{ particle cm}^{-3} \text{ s}^{-1}$ at 10^6 molecules cm^{-3} H_2SO_4) and the orders of magnitude higher sulfuric acid concentration ($>10^8$ molecules cm^{-3}) required to achieve a similar rate in laboratory studies (Zhang, 2004; Riipinen, 2007; Benson, 2009). Indeed, a recent study has found that unsaturated hydrocarbons enhance particle growth (Wang, 2010). Given the data presented here, we suggest that future nucleation studies should be performed in the presence of isoprene and biogenic terpenes to elucidate the potential importance of this heterogeneous process.

Chapter IV

9 Uptake of Glyoxal to Supercooled HNO₃/H₂O on Ice and Organic Material: A Potential Source of SOA in the Upper Troposphere

9.1 Introduction

Recent field studies have found that organics comprise a significant fraction of aerosol mass throughout the entire troposphere (Froyd et al., 2009, 2010; Mirme et al., 2010; Murphy et al., 2006; Nguyen et al., 2008). Significant organic mass fractions have even been found in the tropical tropopause layer (TTL) during periods where continental convection is limited, suggesting that convection through the boundary layer may not be the sole source of organic aerosols in the upper troposphere (UT) (Froyd, 2009). The finding is surprising considering the most abundant non-methane hydrocarbons of the upper troposphere have 3 or less carbon atoms and do not decompose to yield any known condensable products. However, there are compounds in the free troposphere that are known glyoxal precursors, namely acetylene, benzene, isoprene, toluene, and xylene (Greenberg and Zimmerman, 1984; Blake, 2003; Myriokefalitakis, 2008). The di-aldehyde glyoxal (CHOCHO) has been proposed to be a significant SOA precursor in the lower troposphere, especially in deliquesced aerosol (Volkamer, 2007). Given that the conditions of the upper troposphere, and in particular the TTL, are very cold, it is thought that there would not be liquid water available to stimulate SOA formation by this mechanism. However, laboratory and field studies indicate that at conditions relevant to the upper troposphere cirrus ice is likely to have a thin, liquid-like layer of nitric acid/water on the surface (Zondlo, 1998; Iraci, 2002; Hudson, 2002; Gao, 2004; Voigt,

2006; Popp, 2006). Also, the organic material detected in particles in the UT and TTL is highly oxidized (O:C ratio > 1), suggesting it may be hygroscopic (Froyd, 2008 & 2009). Aerosols containing hygroscopic organic material could also uptake nitric acid and water forming a liquid $\text{HNO}_3/\text{H}_2\text{O}$ layer on the surface. Commercially, nitric acid and glyoxal have been reacted to synthesize glyoxylic acid (CHOCOOH), which has a significantly lower vapour pressure than its parent glyoxal (US Patent #3281460, 1968; US Patent #4146731, 1979). In this study we investigate if the supercooled layer of nitric acid/water on ice or hygroscopic organic material is sufficient to uptake glyoxal and form glyoxylic acid.

We have utilized a high vacuum Knudsen flow reactor to determine the uptake probability, γ , of glyoxal to ice films exposed to nitric acid at atmospherically relevant pressures (10^{-8} to 10^{-6} Torr HNO_3) and temperatures (181 – 211 K). Additionally, we have used both infrared spectroscopy and gas chromatography/mass spectroscopy (GC/MS) to confirm glyoxylic acid as the primary product of the uptake. To determine if hygroscopic organic material could also be coated with a reactive $\text{HNO}_3/\text{H}_2\text{O}$ liquid layer, we performed uptake experiments with the glyoxylic acid products from the ice experiments under relevant conditions. We have found that in the presence of nitric acid and water vapour, the glyoxylic acid products also uptake glyoxal and create additional glyoxylic acid at $\text{RH}_{\text{ICE}} > 60\%$. Comparisons to field data are presented and the atmospheric implications of this SOA formation mechanism in the UT are discussed.

9.2 Experimental

9.2.1 Synthesis of Glyoxal

The experiments were conducted in the high vacuum Knudsen flow cell as described in Chapter 2. Anhydrous gas phase glyoxal was prepared by heating a mixture of glyoxal trimer dihydrate (Aldrich) and phosphorous pentoxide (Fisher) to 160° C under a stream of dry, high purity helium. The monomer was collected in a LN₂ trap and purified via trap to trap distillation using a vacuum manifold. The remaining yellow solid/gas was examined using both FTIR and MS: neither technique detected hydrated glyoxal, CO, or CO₂. Water (NERL) and nitric acid (Fisher) (nitric acid mixed 1:3 with sulphuric acid) were both freeze-pump-thawed repeatedly, and mass spectra confirmed dissolved gasses (N₂, CO₂, O₂) had been removed prior to each experiment.

9.2.2 Glyoxal Uptake to Supercooled HNO₃/H₂SO₄ on Ice

For each series of experiments an ice film was initially deposited on the gold surface and an ice frost point calibration performed. Then the ice film was removed and the chamber pumped down. Next, water vapour was introduced at 10⁻³ Torr and a ~150 nm ice film was deposited on the surface. After closing the cup the nitric acid pressure was set to 10⁻⁶ to 10⁻⁸ Torr, and the water vapour was set to the frost point. After opening the cup the equilibrium water vapour pressure was checked, and for each film the equilibrium vapour pressure was equal to the frost point for pure ice, consistent with previous studies (Zondlo, 1998; Hudson, 2002). FTIR-RAS spectra indicate that for all the experimental conditions a supercooled HNO₃/H₂O layer initially formed on the ice. Figure 4.1A shows a spectrum of a film while Figure 4.1B is a spectrum of 4:1 solid amorphous HNO₃/H₂O. It can be seen that the spectrum of ice exposed to gaseous HNO₃

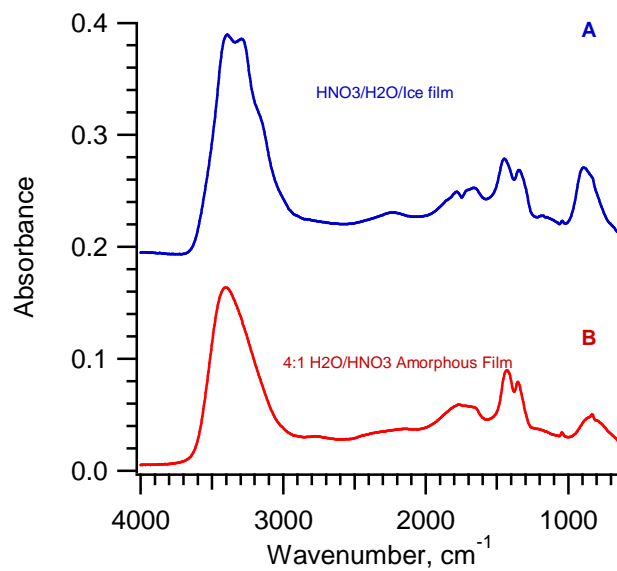


Figure 4.1. A. FTIR-RAS spectrum of ice film exposed to nitric acid, with asymmetric NO_3^- peaks between 1500-1200 indicating the formation of a supercooled $\text{H}_2\text{O}/\text{HNO}_3$. B. FTIR-RAS spectrum of 4:1 $\text{H}_2\text{O}:\text{HNO}_3$ amorphous film for comparison.

is similar to liquid HNO₃/H₂O (Toon, 1994). For nitric acid pressures lower than 10⁻⁶ Torr the layer remained a supercooled solution. However, at pressures above this level the formation of nitric acid trihydrate (NAT) was observed. Upon FTIR-RAS indication of NAT nucleation the cup was immediately closed and the chamber prepped for glyoxal uptake. For films where the supercooled liquid layer persisted the cup was closed after 25 minutes. After isolating the surface from the chamber, glyoxal was introduced into the chamber and monitored at 57 *m/z* (CHOCO⁺) using the MS. When a stable signal was achieved at the desired pressure, the cup was retracted to expose the surface to the glyoxal. A decrease in the signal from the MS corresponds to uptake by the substrate. The Knudsen effusion relation is then used to determine the uptake probability, γ ,

$$\gamma = \frac{A_h(S_0 - S)}{A_s S}, \quad (4.1)$$

where S_0 is the initial MS signal, S is the signal after cup is opened, A_h is the area of the escape orifice (0.19 cm²) and A_s is the surface area of the sample (5.1 cm²). Control experiments were performed on the bare gold substrate and pure water ice films in the absence of HNO₃. Glyoxal uptake was not observed for the control experiments.

9.2.3 Glyoxal uptake to supercooled HNO₃/H₂O on organic material

To test whether hygroscopic organic material exposed to water and nitric acid can also uptake glyoxal, experiments were performed on the reaction products of the above HNO₃/H₂O experiments. For these experiments, the supercooled liquid was left exposed to the glyoxal for more than 600 seconds at optimum uptake conditions to ensure uniform organic coverage. Then the chamber was pumped down to remove excess water and nitric acid until the FTIR-RAS spectra indicated the condensed phase was stable. Next,

the surface was exposed to a set relative humidity and pressure of nitric acid. The FTIR-RAS spectra and a decrease in the chamber pressure both indicated liquid water and nitric acid uptake followed by an equilibration with the gas phase at $RH_{ice} > 60\%$. Following equilibration, the surface was isolated and a steady flow of glyoxal was established before retracting the cup and measuring the uptake probability as before.

9.2.4 Amorphous H_2O/HNO_3 Films

In order to estimate the thickness of the supercooled nitric acid/water layer on the ice films we produced 2:1, 3:1, and 4:1 ($H_2O:HNO_3$) amorphous nitric acid/ice films. The optical properties of HNO_3/H_2O amorphous films (Toon, 1994) are similar to the optical properties of HNO_3/H_2O supercooled liquid films (Norman, 1999; Biermann, 2000). To create the films, steady vapour pressures of both water and nitric acid are established at $H_2O:HNO_3$ stoichiometric ratios with the cup closed. Then, with the surface temperature at 140 K the cup was opened and the films were allowed to grow for 300 seconds. At this low temperature the sticking coefficients for both water and nitric acid are at or near unity, therefore the condensed phase composition will be similar to the vapour phase composition (Toon, 1994, Middlebrook, 1994). The FTIR-RAS spectra for these films are similar to those measured previously, and examples of the spectra are shown in Figure 4.2 (Zondlo, 1997 & 1998; Hudson, 2002). Figure 4.2A shows spectra of the initial growth of the 4:1 H_2O/HNO_3 film. Film thickness was determined by calculating the loss of gas phase HNO_3 to the film over time. To serve as a check for our thickness calculations, we also used the maxima of the interference pattern that appears when the film reaches ~ 340 to 410 nm in thickness as shown in Figure 4.2B (inset), and both methods agree to within 10%. A plot of film thickness versus peak area for the NO_3^-

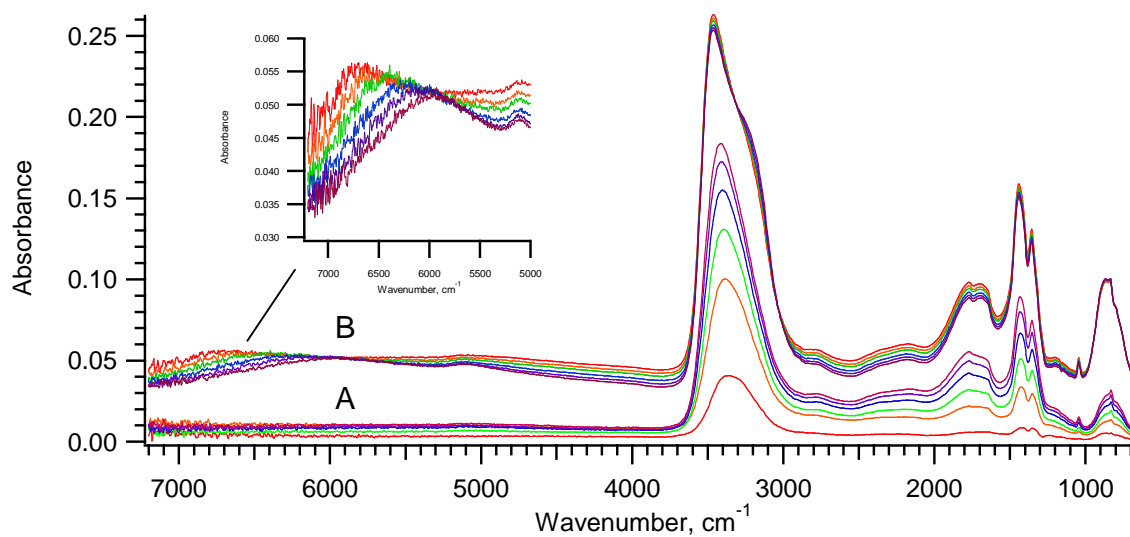


Figure 4.2. FTIR-RAS spectra of 4:1 amorphous H₂O/HNO₃ films. A. Spectra of film taken from the start of growth to 60 seconds, spaced at 10 second intervals for clarity. B. Spectra of film from 272 to 332 seconds showing an interference pattern in the near IR, with inset showing the pattern.

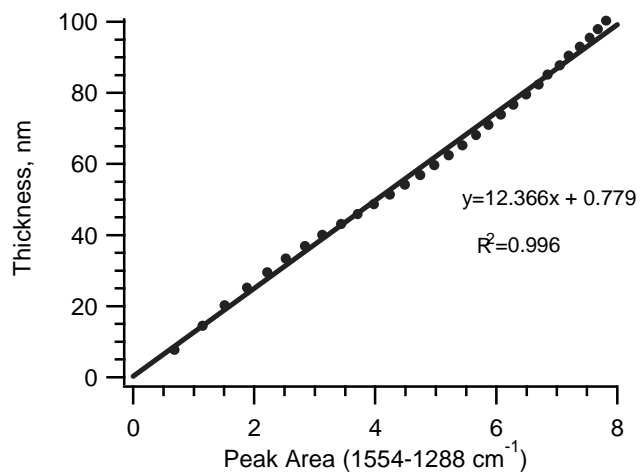


Figure 4.3. A calibration plot of thickness vs peak area for the 4:1 amorphous H₂O/HNO₃ film. The line is a linear fit to the data.

stretches from the spectra is shown in Figure 4.3. For films ranging 0 to 100 nm in thickness the relationship is linear, with a R^2 value of 0.994. This calibration is used to determine the supercooled $\text{HNO}_3/\text{H}_2\text{O}$ film thicknesses prior to the uptake experiment.

9.2.5 Gas Chromatography/Mass Spectroscopy

Gas Chromatography/Mass Spectroscopy with derivatization was used to confirm the products of the uptake. *N*-Methyl-*N*-trimethylsilyl-trifluoroacetamide with 1% trimethylchlorosilane (MSTFA + 1% TMCS) dissolved in an equal volume of pyridine was used as the derivatization agent. After an uptake experiment was performed, the chamber was flushed with dry nitrogen and the gold substrate removed. Then 200 μL of the derivatization agent was added directly to the gold surface and removed using a glass capillary after the solid products dissolved. Following 15 minutes reaction time a 5 μL sample was injected into the GC/MS for analysis. A Finnigan Trace GC Ultra equipped with a Zebron ZB-5mS capillary column (95% dimethylpolysiloxane & 5% phenylarylene, 30 m x 0.25 mm x 0.25 μm) was used for separations and mass spectra were obtained with a Polaris Q ion trap detector (ThermoFinnigan, San Jose, CA). The helium carrier gas flow rate was 1.0 mL min^{-1} . The initial column temperature was 85 $^{\circ}\text{C}$ which was held for 5 minutes, then ramped to 320 $^{\circ}\text{C}$ at 30 $^{\circ}\text{C min}^{-1}$, and then held for 1 min. The EI-Ion trap mass spectrometer collected ions from 30-650 m/z .

9.3 Results and Discussion

9.3.1 Glyoxal Uptake on Nitric Acid/Ice Films

Glyoxal uptake was first probed on the bare gold substrate and pure ice surfaces. Figures 4.4A and B show that glyoxal uptake does not occur on either of these surfaces. In contrast, for all pressures of nitric acid ($10^{-8} - 10^{-6}$ Torr) and of glyoxal ($10^{-7} - 10^{-5}$ Torr), uptake is observed from 181 to 201 K for both supercooled $\text{HNO}_3/\text{H}_2\text{O}$ films and films where partial NAT formation was observed. An example uptake is shown in Figure 4.4C, which is consistent with all experiments performed in the presence of nitric acid. After exposure of the nitric acid/ice film to glyoxal the MS signal decreases to a stable level without recovery, even for the longest measured uptake of 2 hours. The uptake of glyoxal did not vary with the pressure of glyoxal ($10^{-7} - 10^{-5}$ Torr) or temperature (181 – 201 K). However, γ does vary with the pressure of nitric acid. Figure 4.5 shows the uptake probability increases as nitric acid pressure increases.

After glyoxal uptake the chamber was then pumped free of glyoxal with the cup closed. When the cup was retracted the MS did not indicate any desorption of glyoxal from the film. Irreversible uptake without recovery is indicative of a fast reaction occurring on or in the condensed phase. The FTIR-RAS spectra confirm this hypothesis. Figure 4.6A shows the uptake products while Figure 4.6B is an FTIR-RAS spectrum of glyoxylic acid, a known reaction product of glyoxal and nitric acid. The spectra are very similar indicating the irreversible formation of glyoxylic acid. The absorbance in OH stretching region ($3500\text{-}3000\text{ cm}^{-1}$) of the uptake sample suggests either the presence of liquid water or that a hydrate of glyoxylic acid is present. Given that the chamber was pumped down to 10^{-7} Torr ($< 0.02\% \text{ RH}_{\text{ice}}$) and held for 10 minutes without a change in

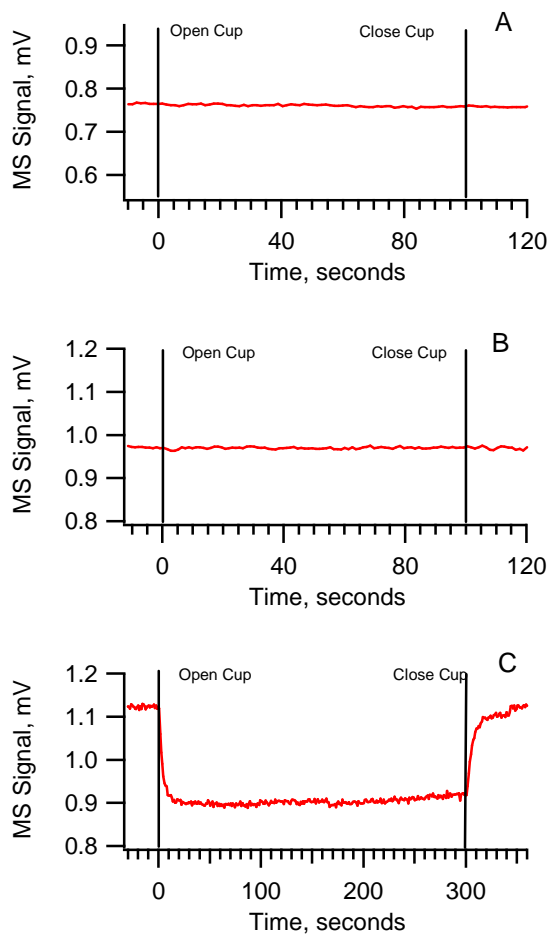


Figure 4.4. Mass spectrometer signal vs time for glyoxal uptake experiments. A. Bare gold substrate. B. Ice film. C. Uptake to ice film exposed to 10^{-6} Torr nitric acid.

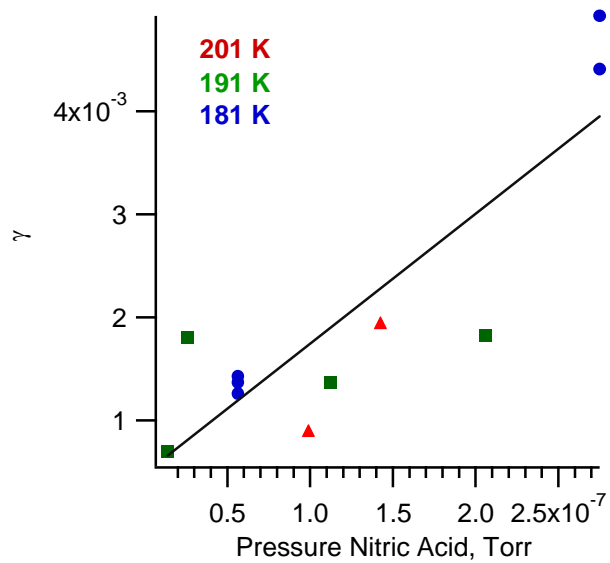


Figure 4.5. Plot of γ vs pressure of nitric acid for glyoxal uptake to supercooled liquid $\text{HNO}_3/\text{H}_2\text{O}$ on ice, with colours / shapes indicating the temperature. Line serves only to guide the eye.

the spectra, the OH stretch is likely due a hydrate. Additionally, the absorbance of the uptake products between 1500 and 1400 cm^{-1} , while larger than our standard, are still consistent with the literature, which reports a peak for the glyoxylic acid hydrate at 1442 cm^{-1} (Fleury, 1971).

For ice films exposed to nitric acid pressures greater than 10^{-6} Torr the FTIR-RAS spectra indicates nucleation of NAT. Despite the presence of the nitric acid hydrate glyoxal uptake is observed on these films as well, with similar product spectra. However, for these data points the calculated γ values (assuming a constant surface area) had an increased variance, with values ranging from 10^{-3} to as high as 10^{-2} . We propose that given the high viscosity of supercooled solutions and the continued uptake of nitric acid that some supercooled liquid remains at the surface available for uptake, while some of the $\text{HNO}_3/\text{H}_2\text{O}$ has crystallized into NAT. Given this scenario, we can not report γ values as we can not determine the fraction of the surface area covered with NAT, relative to that covered with a supercooled $\text{HNO}_3/\text{H}_2\text{O}$ liquid. To test this hypothesis we nucleated a NAT film and then pumped out the remaining HNO_3 vapour. Glyoxal uptake was not observed under these conditions, demonstrating that glyoxal is not taken up by solid NAT films.

To confirm the identity of the reaction products GC/MS analysis with derivatization was employed. The products were extracted directly from the Knudsen cell, derivatized on the gold substrate, and injected into the instrument after allowing 15 minutes for derivatization. The mass spectra of the only two discernable GC product peaks are shown in Figure 4.7A and B. Also in Figure 4.7A is the NIST reference spectra

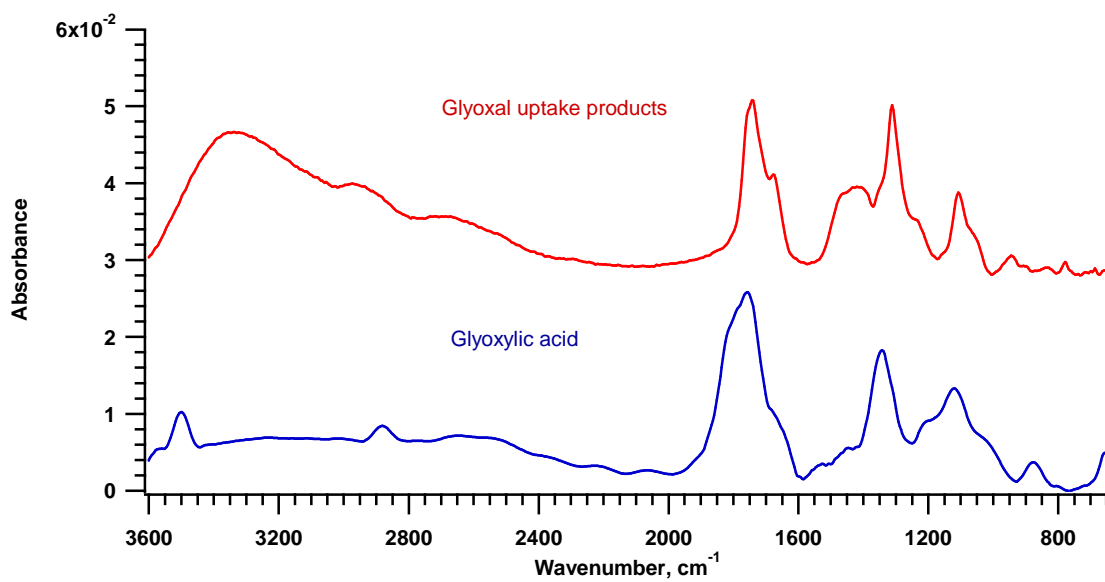


Figure 4.6. FTIR-RAS spectra of the products of the glyoxal uptake (red) and a spectra of glyoxylic acid. The spectra are offset for clarity.

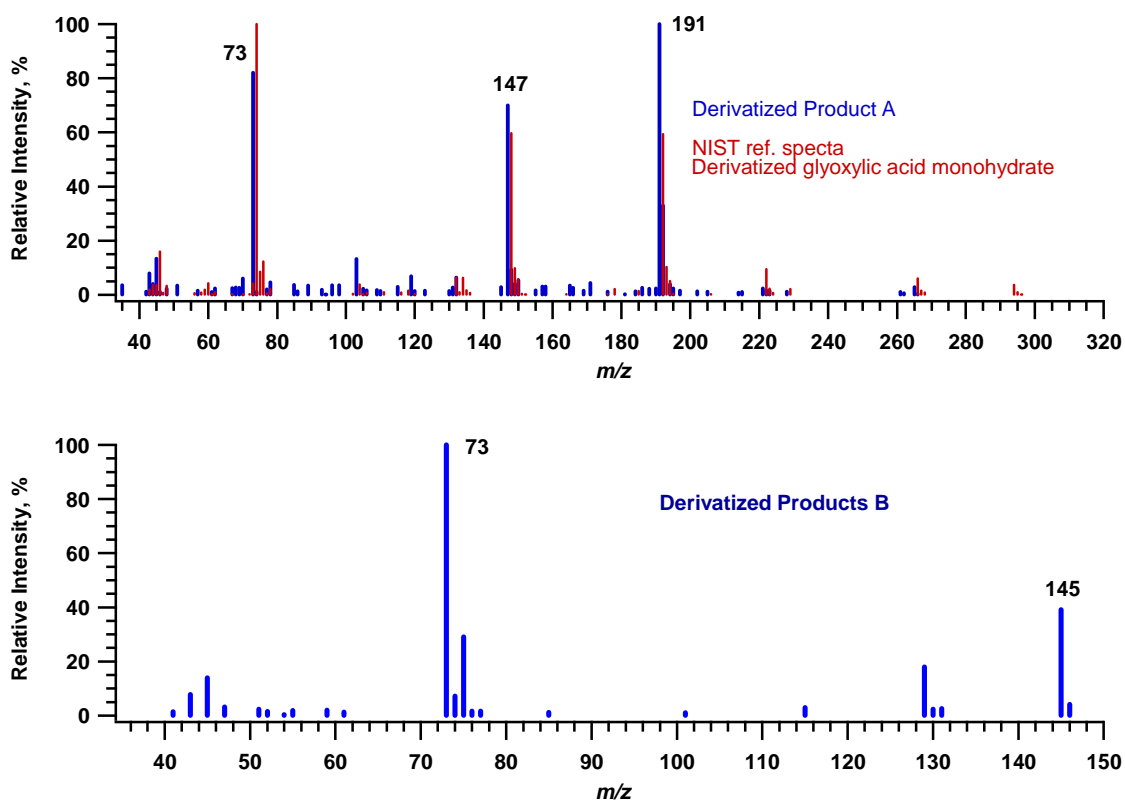


Figure 4.7. The mass spectra of the two derivatized uptake products. Top spectrum is product “A” compared to NIST reference spectra for derivatized glyoxylic acid monohydrate, which is offset + 1 m/z for clarity. B. Bottom spectrum is product “B” with a peak at 145 m/z , consistent with derivatized anhydrous glyoxylic acid ($C_2H_2O_3+TMS$).

for trimethylsilyl derivatized monohydrate of glyoxylic acid, and the spectra are very similar. While a reference spectra for the anhydrous form was not available, the peak from the other product in Figure 4.7B at $145\ m/z$ is the correct mass for the $(M-H)^+$ ion of derivatized anhydrous glyoxylic acid. The GC/MS analysis is in agreement with the FTIR-RAS spectra in Figure 4.6. The FTIR-RAS spectrum closely resembles glyoxylic acid with features indicating the presence of the hydrate. We conclude that the primary reaction product of the glyoxal uptake to supercooled liquid HNO_3/H_2O films is glyoxylic acid in both its anhydrous and hydrate forms, which is expected. Industrially, mixtures of glyoxal and nitric acid have been used to synthesize glyoxylic acid (sold as the monohydrate), producing NO_2 gas as a by product (US Patent #3281460, 1969). Due to the significant NO_2^- ion in the mass spectra from nitric acid, we could not directly determine NO_2 production from the uptake process. However, given that the products of the industrial process have been studied in detail we propose that the uptake of glyoxal by supercooled HNO_3/H_2O results in the formation of glyoxylic acid, which then is in equilibrium between its anhydrous and monohydrate states. The mechanism of the reaction cannot be determined from the data obtained from our experiments, and the possibility of intermediate carbonyl-nitrate compounds can not be ruled out. However, given the irreversibility of the reaction and resemblance of the FTIR-RAS spectra to glyoxylic acid during the uptake process it is likely that intermediate carbonyl-nitrate compounds are short lived.

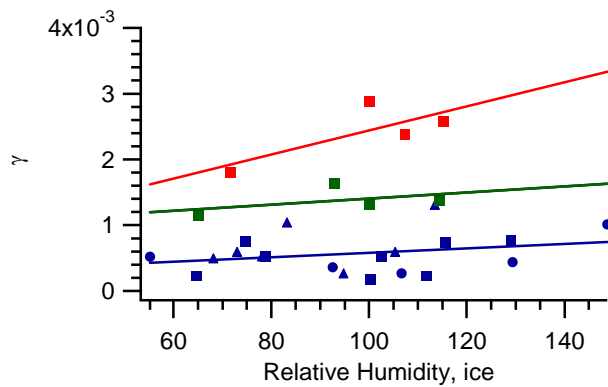


Figure 4.8. γ vs RH_{ice} for glyoxal uptake to supercooled HNO_3/H_2O on glyoxylic acid products with linear fits. Blue plot is for nitric acid pressures of 7×10^{-8} Torr, with circles at 181 K, triangles at 191 K, and squares at 200 K. Green and red plots are both at 200 K with nitric acid pressure at 4×10^{-7} Torr and 2×10^{-6} Torr respectively.

9.3.2 Glyoxal Uptake to HNO₃/H₂O Supercooled Liquid on Organic Products

Since glyoxylic acid, and other organic compounds found in aerosols in the UT and TTL are hygroscopic, we tested whether supercooled layers of HNO₃/H₂O could form on organic material and also uptake glyoxal. For our organic film, we used the glyoxylic acid films from the glyoxal uptake on supercooled films from the prior experiments. The experiments were conducted as a function of relative humidity, temperature, and pressure of nitric acid. When the relative humidity with respect to ice reached ~ 60% we observed the uptake of water and nitric acid to the organic films by both a drop in the chamber pressure and changes to the FTIR-RAS spectra. When uptake of water and nitric was observed, glyoxal uptake experiments were also performed. The blue trace and symbols in Figure 9 show that γ increases as a function of RH_{ice} from 65 to 130% at fixed pressure of nitric acid, independent of temperature between 181 to 201 K. Figure 4.8 also illustrates that γ increases as nitric acid pressure increases from 7.3×10^{-8} Torr (blue), to 4.3×10^{-7} Torr (green), and to 2.4×10^{-6} Torr (red) HNO₃. The γ values range from 2×10^{-4} for the lowest RH_{ice} and nitric acid pressure to 3×10^{-3} the highest values. As with the ice experiments, the uptake is also continuous without recovery, and irreversible on the organic/HNO₃/H₂O films. The uptake yields the same FTIR-RAS spectra, therefore we conclude that the uptake of glyoxal with a fast irreversible reaction to glyoxylic acid is also occurring on the products films exposed to nitric acid and water vapour.

9.4 Atmospheric Implications

In the atmosphere glyoxal can be sourced from acetylene, benzene, toluene, xylene, and isoprene. All of these compounds have been detected by field measurements in the free troposphere (Greenberg and Zimmerman, 1984). Using the average concentration in the free troposphere of these precursors from the field measurements along with published rate coefficients, glyoxal yields, and an OH radical concentration of 10^6 molecules cm^{-3} , we estimate the glyoxal source strength to be 1.86×10^4 molecules $\text{cm}^{-3} \text{ s}^{-1}$ (Greenberg and Zimmerman, 1984; Myriokefalitakis, 2008; Finlayson-Pitts and Pitts, 2000). Given the production, the steady state ambient concentration can be determined from the sinks by

$$\text{Source} = \text{Sinks} \quad (4.2)$$

$$\text{Source} = J_{\text{Glyoxal}} [\text{Glyoxal}] + k_{\text{OH}} [\text{Glyoxal}] + k_{\text{het}} [\text{Glyoxal}] \quad (4.3)$$

$$[\text{Glyoxal}] = \frac{\text{Source}}{k_{\text{OH}} + J_{\text{Glyoxal}} + k_{\text{het}}}, \quad (4.4)$$

where J_{Glyoxal} , k_{OH} , and k_{het} , are the photolysis rate, rate constant for glyoxal reaction with OH, and heterogeneous rate constant for glyoxal loss respectively. The heterogeneous rate constant, k_{het} , can be estimated in the kinetic regime by

$$k_{\text{het}} = \gamma \langle v \rangle SA / 4 \quad (4.5)$$

where γ is the uptake coefficient, $\langle v \rangle$ is the mean speed, and SA is the surface area of the particles in $\text{cm}^2 \text{ cm}^{-3}$. Using the average gamma from our experiments of 10^{-3} and a particle surface area in the UT from field measurements of $6 \times 10^{-8} \text{ cm}^2 \text{ cm}^{-3}$ (Froyd, 2009), $k_{\text{het}} = 4.05 \times 10^{-7} \text{ s}^{-1}$. The estimated photolysis rate for glyoxal, J_{glyoxal} , is $8.9 \times 10^{-5} \text{ s}^{-1}$, and the rate constant for reaction with OH (at 10^6 molecules cm^{-3}), k_{OH} , is $1.5 \times 10^{-5} \text{ s}^{-1}$ (Finlayson-Pitts and Pitts, 2000; IUPAC, 2006; Myriokefalitakis, 2008; Feierabend,

2008). Using Equation 4.4 the steady state concentration of glyoxal would be 1.8×10^8 molecules cm^{-3} (37 pptv). Recent measurements of glyoxal in the free troposphere indicate concentrations are greater than 10 pptv (Volkamer, personal communication), so our estimation is consistent with measurement. From our experiments glyoxal uptake to $\text{HNO}_3/\text{H}_2\text{O}$ films on hygroscopic organics (glyoxylic acid) was observed when the $\text{RH}_{\text{ice}} > 60\%$. Data from the UT reflects a 60% probability of the RH_{ice} being greater than 60% (Ryoo, 2008), therefore we will assume uptake is only occurring 60% of the time. Using k_{het} and the previous assumption, the average daytime uptake of glyoxal is 43 molecules $\text{cm}^{-3} \text{ s}^{-1}$. Froyd and coworkers (2009) estimated a continuous source of ~ 100 molecules $\text{cm}^{-3} \text{ s}^{-1}$ (day and night) could account for all of the organic mass in the particles measured in the UT in one month; therefore, reactive heterogeneous uptake during the daytime could account for almost one half of the estimated source.

Once day becomes night, there is not a glyoxal loss via photolysis, and OH radical concentration will decrease as it is sourced by photolysis as well. As OH concentrations decrease the glyoxal source and OH sink will decrease by the same factor, which would leave the ambient concentration approximately equal to the daytime value when night falls. Models predict the night-time OH radical concentration at this altitude will drop to $\sim 10^3$ molecules cm^{-3} (Lu and Khalil, 1991). At an OH concentration of 10^3 molecules cm^{-3} the rate constant for glyoxal reaction with OH, k_{OH} , would now be $1.5 \times 10^{-8} \text{ s}^{-1}$. The heterogeneous rate constant would not change, and at night is greater than k_{OH} by a factor of 25. Therefore, heterogeneous loss could titrate down the daytime concentration of glyoxal. Starting with the daytime concentration (37 pptv), the night time uptake can be estimated by first order kinetics,

$$P = [\text{Glyoxal}(0)] - [\text{Glyoxal}(0)]\exp(-k_{\text{het}}t) \quad (4.6)$$

where P is the production of condensed glyoxal (molecules $\text{cm}^{-3} \text{s}^{-1}$), $[\text{Glyoxal}(0)]$ is the initial concentration of glyoxal, and t is the overall night time in seconds. Using Equation 4.6 (also assuming uptake only 60% of the time) the particle could uptake 43 molecules $\text{cm}^{-3} \text{s}^{-1}$ of glyoxal, which over the course of a 12 hour evening would consume 1% of the gas phase glyoxal. Averaging the day light and night-time for a full diurnal cycle, heterogeneous glyoxal uptake could account for 43% of the estimated source of organic aerosol in the upper troposphere. Field data support our proposed reactive heterogeneous uptake of glyoxal, as a positive correlation was observed for the nitrate content of the particles and oxidized organic signal in the UT and TTL (Froyd, 2009). It should be noted that glyoxylic acid and its monohydrate are significantly oxidized, with O/C ratios of 1.5 and 2 respectively. Our results suggest that glyoxal uptake to $\text{HNO}_3/\text{H}_2\text{O}$ supercooled liquid solutions on both ice and hygroscopic organic material may be a significant source of SOA in the UT and in the TTL.

Chapter V

10 Laboratory investigations on the effect of nitric acid vapour on ice nucleation on ammonium nitrate thin films and experimental determination of the growth rate of NAT.

10.1 Introduction

Cirrus clouds are ubiquitous in the upper regions of the troposphere and are composed primarily of water ice. The ice in cirrus clouds affects the climate directly by absorbing and scattering light, and aerosols indirectly influence climate by modifying cloud formation and optical properties. Also, ice clouds dehydrate air before it enters the stratosphere which manages water exchange between the troposphere and stratosphere (Jensen, 1996). The effects are shown in Figure 1.3, and their combined effect is greater than the overall effect of greenhouse gases. Despite the commonality of cirrus clouds the mechanism responsible for cloud formation is uncertain. The mechanisms need to be understood in order to improve the accuracy of global climate models.

Ice is thought to nucleate at these high altitudes either through homogeneous or heterogeneous processes. Homogeneous ice nucleation would occur if a particle is in a liquid state and the liquid freezes as temperature decreases and relative humidity (water activity) increases. Koop et al. (2000) proposed that the driving force of homogeneous nucleation is water activity, not the chemical composition of the aqueous phase. A majority of inorganic systems studied agree with the activity model (Cziczo and Abbatt; 2001; Mangold, 2005; Larson, 2006). While some of these experiments found that ammonium sulphate (AS) nucleated prior to the predicted homogeneous nucleation curve it is likely that some of the AS had effloresced prior to the experiment and had nucleated

heterogeneously (Wise, 2009). Mixtures of organics/inorganics have been found, in some cases, to increase the threshold of homogeneous nucleation (Prenni, 2001; Pant, 2004; Beaver, 2006). In some cases an increase is not observed (Zobrist, 2008), but organic material and conditions did differ for these experiments.

Heterogeneous nucleation, by definition, involves two separate phases, and therefore two separate mechanisms. Heterogeneous nucleation can refer to the deposition of water from the gas phase to the solid phase. For the sake of clarity, gas to solid ice nucleation will be referred to as depositional nucleation. Depositional nucleation occurs when the critical supersaturation ratio with respect to ice occurs prior to deliquescence. At low temperatures, laboratory experiments have found that the critical supersaturation ratio, S_{crit} , is lower for depositional ice nucleation than for homogeneous nucleation (Zuberi, 2002; Beaver, 2006; Knopf, 2006; Shilling, 2006; Baustian, 2010).

Heterogeneous ice nucleation can also refer to a particle that has both a liquid and solid phase. Nucleation by this pathway has been studied (Zobrist, 2008), and has found that liquid-solid heterogeneous nucleation occurs at similar water activities as homogeneous nucleation, for the four non-soluble nuclei studied.

When the homogeneous nucleation mechanism is applied to atmospheric models, the models predict high number densities of ice because water activity, and therefore relative humidity, controls the nucleation in conjunction with temperature (Karcher and Lohmann, 2002). The results are inconsistent with field observations of a low ice number density (Lawson, 2008) and high levels of ice supersaturations ($S_{ice} > 1.2$) inside the cloud (Jensen, 2005; Gensch, 2008; Kramer, 2009). Models using the heterogeneous ice

nucleation pathway predict the number density of particles more accurately (Gierens, 2003; Abbatt, 2006), however the large supersaturations remain a mystery.

Different theories have been proposed to account for the large supersaturations in cirrus clouds. There may be particles that preferentially nucleate ice in the upper troposphere (UT). The presence or absence of organic material may cause different values for different particles. Mineral dust has also been investigated as a potentially efficient ice nucleating material. However, recent field studies have not found mineral dust or a discernable difference between the unfrozen aerosol and the nuclei inside frozen subvisible cirrus ice (Froyd, 2010). It has been reported that the vapour pressure of cubic ice is greater than that of hexagonal by 10%, which may in part help explain the observations (Shilling, 2006); but this claim has been disputed as the enthalpy change should only account for a difference of 1% (Bogdan, 2009). The possibility of a new phase of nitric acid/ice, Δ -ice, has been proposed to have a higher vapour pressure than ice (Gao, 2004), but the process as described may violate the second law of thermodynamics (McGraw, 2004). Zobrist and coworkers (2008) proposed that organic containing aerosol may form glasses in strong updrafts, and glassy material may settle back into the UT and inhibit nucleation. On the contrary, experimental results indicate the opposite is true, laboratory produced glassy material heterogeneously nucleates at a lower ice saturation ratio, S_{ice} , than its crystalline counterpart (Murray, 2010).

It is important to note that for all the above laboratory nucleation experiments, the only species in the vapour phase was water. In the upper troposphere, as indicated in the Gao et al. (2004) hypothesis, nitric acid vapour is ubiquitous. Lin and Tabazadeh (2002) proposed that nucleation experiments should be conducted in the presence of nitric acid

vapour. The manuscript investigated the thermodynamic model by Clegg et al. (1998), and found it predicts that at low temperatures ammonium nitrate (AN), ammonium sulphate, and ammonium bisulphate should partially deliquesce in the presence of nitric acid vapour prior to ice nucleation, forming mixed phase liquid/solid aerosol. A forward search on the manuscript indicates that process has not been investigated.

A Knudsen cell flow reactor was used to probe the effect nitric acid vapour has on ice nucleation of AN. Even with trace levels nitric acid vapour ($< 10^{-8}$ Torr), below typical concentrations in the UT, a liquid layer develops on the surface forming a solid/liquid mixed phase as predicted by Lin and Tabazadeh (2002). The AN/HNO₃ mixed phase film is observed to nucleate ice below the homogeneous ice nucleation threshold set by the Koop et al. (2000) model. For experiments with levels of nitric acid greater than 10^{-8} Torr, the liquid layer can increase in thickness or heterogeneously nucleate to form ice or nitric acid trihydrate. The pathway depends on the experimental conditions. At 210 K if the S_{ice} is between 1 and the critical supersaturation for ice nucleation, S_{crit} , a liquid layer forms on the solid AN and uptakes water continuously. At 210 K ice nucleation will occur if S_{ice} is raised to S_{crit} . At 190 and 200 K, if S_{ice} reaches S_{crit} rapidly (< 500 minutes), ice nucleates. If the S_{ice} is held below S_{crit} , NAT nucleation is observed.

To fully understand the significance of the two nucleation pathways, one leading to ice and the other NAT, it is imperative to know how these solids would interact with the gas phase. To this end, the growth and evaporation rate of each phase has been determined. For all conditions studied NAT grows at a significantly slower rate than ice, while both films evaporate at approximately the same rate. Spectral data indicates that a

supercooled $\text{HNO}_3/\text{H}_2\text{O}$ liquid layer may exist on the surface of NAT, serving to regulate how NAT interacts with both water vapour and ice. The atmospheric implications of these findings are discussed.

10.2 Experimental

10.2.1 Preparation of Optically Flat Ammonium Nitrate Films

Experiments were conducted in high vacuum Knudsen flow cell with FTIR-RAS. The apparatus is described in detail in Chapter 2. Water vapour is introduced into the chamber via a leak valve. The vapour comes from a bulb with pure water (NERL) that has been subjected to repeated freeze-pump-thaw cycles to remove dissolved gases. The mass spectrometer is used to confirm the purity of the water. Nitric acid vapour is introduced by preparing a 3:1 molar $\text{H}_2\text{SO}_4:\text{HNO}_3$ solution and using the vapour above the solution. Dissolved gases are removed and purity is also verified by mass spectroscopy. Anhydrous ammonia vapour, NH_3 , is sourced from a cylinder of liquid NH_3 (99% Pure Gas). The cylinder is connected to a manifold and introduced into the chamber by a chemically resilient leak valve.

The production of optically flat AN films has been described previously (Shilling, 2004). Briefly, the temperature of the gold substrate is reduced to 160 K. Then, with the cup closed nitric acid, HNO_3 , vapour is introduced into the chamber at $\sim 1 \times 10^{-3}$ Torr. The cup is retracted and molecular nitric acid condenses on the substrate, which is confirmed by the FTIR-RAS as shown in spectrum in Figure 5.1 (Green Spectrum). Next the surface is isolated from the chamber and the nitric acid is pumped out. When the chamber pressure is restored to the original level ($\sim 1 \times 10^{-7}$ Torr), gaseous anhydrous

ammonia is introduced at 5×10^{-3} Torr and the cup retracted. After 5 ~ 10 minutes the presence of NH_3 reacting with the molecular HNO_3 in the condensed phase is clear as shown in Figure 4.1 (Blue Spectrum). The film is then annealed at 265 K to remove any unreacted HNO_3 and NH_3 , and to crystallize the film. A spectrum of the final film is shown in Figure 4.1 (Red Spectrum), and is consistent with previous films (Shilling, 2004 & 2006).

10.2.2 Experimental Determination of S_{crit}

The Knudsen flow reactor is used to determine the critical supersaturation ratio, S_{crit} , for the substrate. The procedure for determining the S_{crit} is illustrated in Figure 5.2. First, the FTIR-RAS spectra are carefully examined to ensure it is free of any liquid or solid water features on the AN. As described in Chapter 2, FTIR-RAS has monolayer sensitivity and before each experiment is conducted the spectra indicate the film is solid AN. Then, with the surface exposed to the chamber atmosphere the water vapour pressure is incrementally increased using the leak valve as shown in Figure 5.2 (Red Trace). The size of the steps is determined by the precision of the leak valve. During the pressure increase, the FTIR-RAS records spectra and displays the integrated peak areas at 2 second intervals for both of the predominant spectral ranges for ice: $3600 - 3350 \text{ cm}^{-1}$, and $1000 - 870 \text{ cm}^{-1}$. When the FTIR-RAS indicated ice formation, the event was confirmed by the Baratron reading, as water pressure would decrease. Figure 5.3 is a magnification of Figure 5.2 and shows the event is clearly visible in both the spectral trace and pressure reading. After nucleation, the water pressure is increased to grow a thick film across the substrate, and the frost point ($S_{ice} = 1$) of the ice is determined.

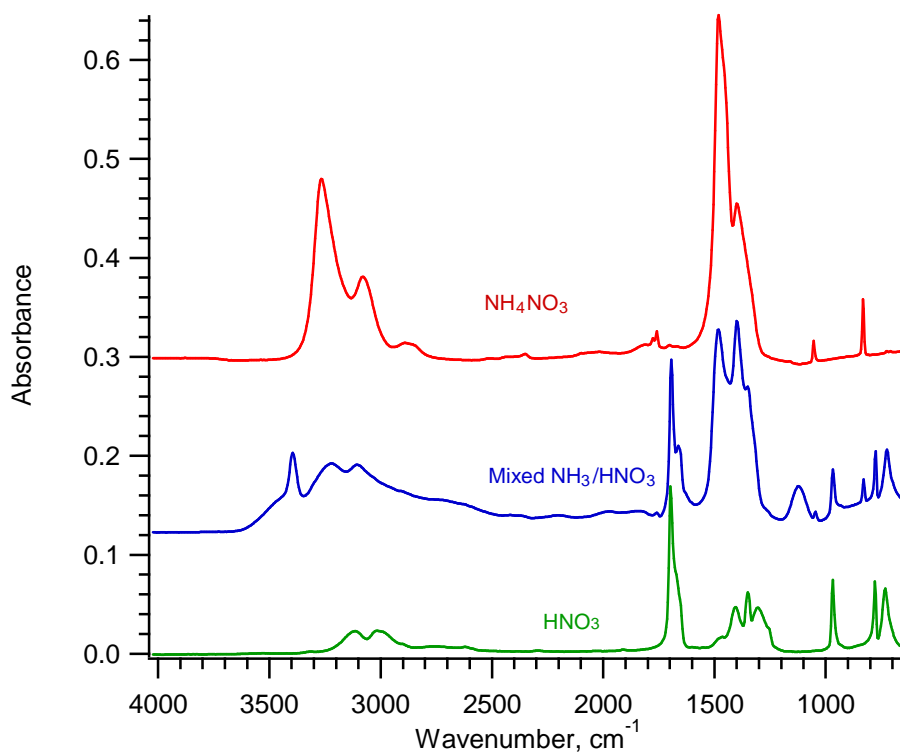


Figure 5.1. FTIR-RAS spectra of the *in situ* growth of an ammonium nitrate film. Nitric acid (green trace) is deposited on the substrate at 160 K. The blue trace is after the molecular HNO₃ is exposed to ammonia vapour. The red trace is the film after annealing to 265 K.

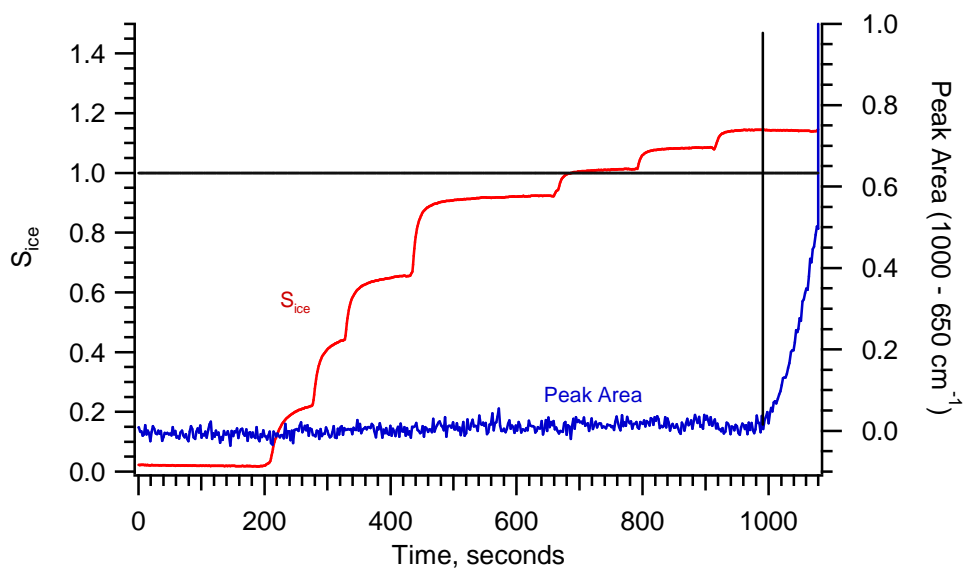


Figure 5.2. A sample experiment for determination of S_{ice} on ammonium nitrate films. The red trace is the value of S_{ice} (left axis), and the blue trace is the integrated peak area from the FTIR-RAS (right axis). The horizontal black line marks where $S_{ice} = 1$, and the vertical black line indicates the onset of ice nucleation.

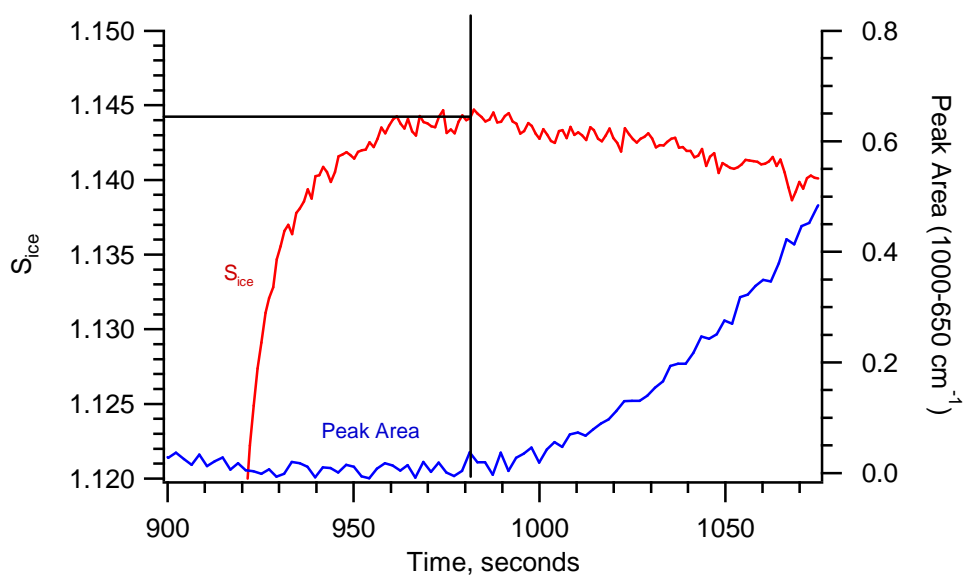


Figure 5.3. A closer view of the nucleation point from the S_{ice} experiment in Figure 5.2.

The critical saturation ratio is then determined by dividing the water pressure where nucleation occurred by the ice frost point. The temperature was determined by referencing the measured frost point to literature data (Marti and Mauersberger, 1993). Experiments were also performed on the bare gold substrate to ensure that ice had nucleated on the film as opposed to the gold. For all of the AN films studied the S_{crit} values lie below the experimental determined S_{crit} value for the gold surface.

10.2.3 Water Uptake Experiments

Experiments were also performed with nitric acid vapour in the chamber. For these experiments, the film was dried at high vacuum ($\sim 1.0 \times 10^{-7}$ Torr) and then isolated from the chamber by closing the Teflon cup. Then nitric acid was introduced into the chamber with cup isolating the surface from the chamber. Nitric acid pressures were monitored at $46 m/z$ (NO_2^+) using the mass spectrometer. The nitric acid pressures used in these experiments were all less than sensitivity of the Baratron, 1×10^{-6} Torr, which was used to measure the pressure of water vapour. For each run, the Baratron reading remained at zero while the nitric acid pressure was set. After the nitric acid pressure was set to the desired level the cup was retracted and the experiment performed. A decrease in signal indicates uptake to the surface. The uptake probability, γ , is calculated from the drop in signal by Equation 2.9. Additionally, the number of molecules lost to the surface can be calculated by the integrated area of the uptake curve using the ideal gas law and Equation 2.1.

Water uptake experiments were performed on the films in the absence of nitric acid flow from the leak valve, though experimental evidence indicates there may have been residual nitric acid at pressures lower than the limit of detection of the mass

spectrometer (1×10^{-8} Torr). The effect of the low level of nitric acid is discussed in following chapter.

10.3 Results and Discussion

10.3.1 Ice Nucleation on Ammonium Nitrate

For ice nucleation experiments performed on AN, careful inspection of the FTIR-RAS spectra did reveal spectral changes prior to nucleation as shown in Figure 5.4. Spectrum A was taken after annealing with the film subjected to high vacuum (1×10^{-7} Torr) for 3 hours. Spectrum B is the film after exposure to 2.44×10^{-3} Torr water vapour at 190 K ($S_{ice} = 0.76$). While to the naked eye Spectra A and B seem similar, the subtraction spectrum, B – A, is shown as Spectrum C. For comparison, a standard spectrum of amorphous 3:1 H₂O:HNO₃ is shown in Spectrum D. The spectrum of amorphous HNO₃/H₂O is similar to liquid nitric acid and water (Toon, 1994), with the exception of solid water libration centred at 850 cm^{-1} . The asterisks indicate the spectral features in the subtraction spectrum that match features of liquid HNO₃/H₂O.

To confirm the existence of a HNO₃/H₂O supercooled liquid layer on the AN films seen in FTIR-RAS observations, water uptake experiments were performed on the AN films. An example uptake is shown in Figure 5.5. Water uptake was observed on all films with liquid coverages ranging 1 to 5 monolayers, even at S_{ice} values as low as 0.25. Water uptake to AN prior to its deliquescence point could occur for two reasons. First, that the ammonium nitrate is not fully effloresced and water uptake is occurring because the film is aqueous. Second, that residual nitric acid below the limit of detection of the

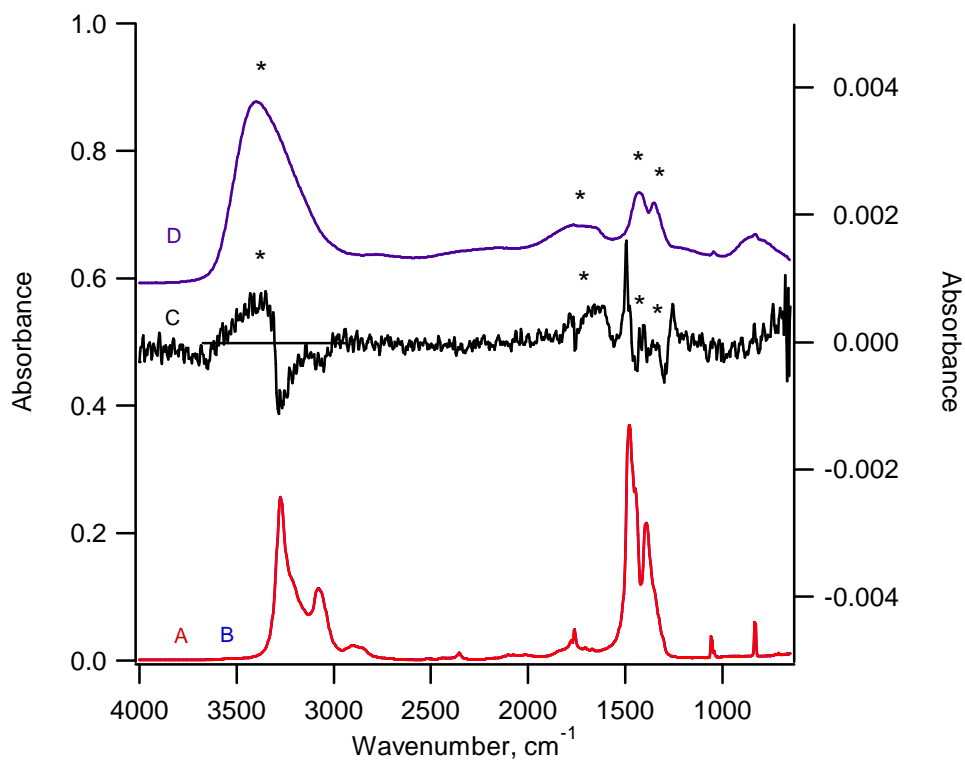


Figure 5.4. FTIR-RAS spectra of the AN film prior to water uptake (A) and after exposure to 2.44×10^{-4} Torr H_2O at 190 K (B). Spectrum C is a subtraction of A from B. Spectrum D is 3:1 amorphous $\text{H}_2\text{O}:\text{HNO}_3$, and the asterisks indicate the matching peaks from Spectrum C & D.

mass spectrometer may be sufficient to enable the two phase system as proposed by Lin and Tabazadeh (2002).

If the film is not effloresced, then the water uptake can be predicted using the Aerosol Inorganic Model (AIM) developed by Clegg et al. (1998). Using the experimental conditions, and disallowing the formation of solid AN, the model predicts H₂O mole fraction of the aqueous phase for the film used for Figure 5.5 would be 0.42. As determined by interference pattern in the IR, the original AN film was ~ 250 nm thick. If we approximate the density of AN by using its value at 298 K of 1.7 g/cm³, the film would consist of 1.63×10^{18} molecules AN. Therefore, applying the mole ratio from the AIM model, the modelled water uptake is 1.18×10^{18} molecules. The measured uptake for the film in Figure 5.5 is 5.5×10^{16} molecules, a factor of 0.046 lower than predicted. Additionally, if the film were liquid it should then resemble the spectrum of aqueous ammonium nitrate. Figure 5.6 is a spectra of deliquesced AN at 273 K at different relative humidity (Cziczo and Abbatt, 2000). Since the solubility of AN decreases with temperature, a solution of a 0.42 mole ratio at 273 K would have a RH of ~ 40%. The 30% and 50% RH spectra from Figure 5.6 do not match the spectra in Figure 5.4: the addition of water should form a separate peak centred at 3400 cm⁻¹ and the peak at ~ 1400 cm⁻¹ should increase in intensity. Those changes are not observed in the spectra. FTIR-RAS is also sensitive to the differences between as isotropic (crystalline) and anisotropic film as discussed in Chapter 2.5. The spectra in Figure 5.4 have sharp peaks, not broad features indicative of anisotropic media, as can be seen by comparing the isotropic AN spectra to that of the amorphous HNO₃/H₂O. Finally, if the AN is aqueous the solution should freeze homogeneously. According to the model developed

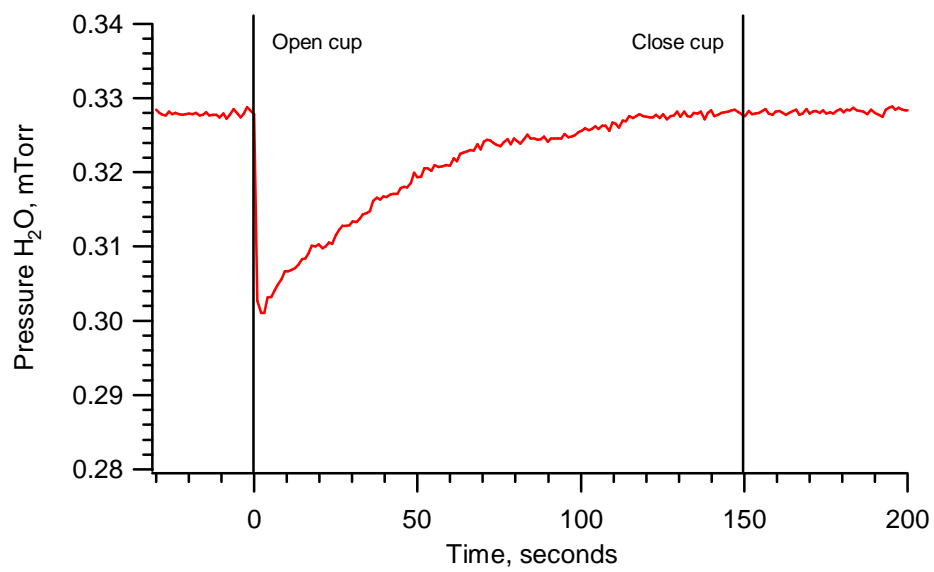


Figure 5.5. Water uptake to ammonium nitrate at 190 K, with nitric acid vapour below the limit of detection.

by Koop et al. (2000) the S_{ice} at 190 K for homogeneous ice nucleation is 1.75, and for this film ice formation occurred at $S_{ice} = 1.32$. Therefore, the possibility of a deliquesced film is unlikely.

The second possibility is that both a solid AN and a liquid layer coexist. The subtraction spectrum in Figure 5.4 is consistent with aqueous nitric acid and water. If an aqueous layer does exist, the AIM model predicts that a small fraction of the condensed AN will partition to the aqueous phase, and the bulk of AN will remain crystalline. Partial dissolution of AN is supported by the infrared spectra, as a decrease is observed for the solid AN peaks. While HNO_3 was not detected in the chamber, the limit of detection for the mass spectrometer is 1×10^{-8} Torr. Nitric acid is known to have a strong affinity for surfaces, even at room temperature (Dubowski, 2004). It is possible that the chamber walls could be maintaining nitric acid vapour pressures below the limit of detection of the mass spectrometer, and this nitric acid is partitioning to the cold AN film at these low pressures.

For the experimental conditions used here, the AIM model (Clegg, 1998) predicts the lowest equilibrium vapour pressure of nitric acid over a mixed AN/ HNO_3 aqueous/solid film would be 2×10^{-8} Torr. However, nitric acid uptake has been observed to surfaces below the predicted equilibrium vapour pressure; on ice (Hansen, 1992; Abbatt, 1997; Arora, 1999; Hudson, 2002; Ullerstam and Abbatt, 2005) and mineral dust (Frinak, 2004; Mashburn, 2006). To validate that residual nitric acid vapour is at a sufficient pressure to be the source, the data from the water uptake experiment in Figure 5.5 can be used again. The AIM model predicts the mixed aqueous phase would have a H_2O to HNO_3 ratio of 5:1. The uptake in Figure 5.5 was 5.5×10^{16} molecules,

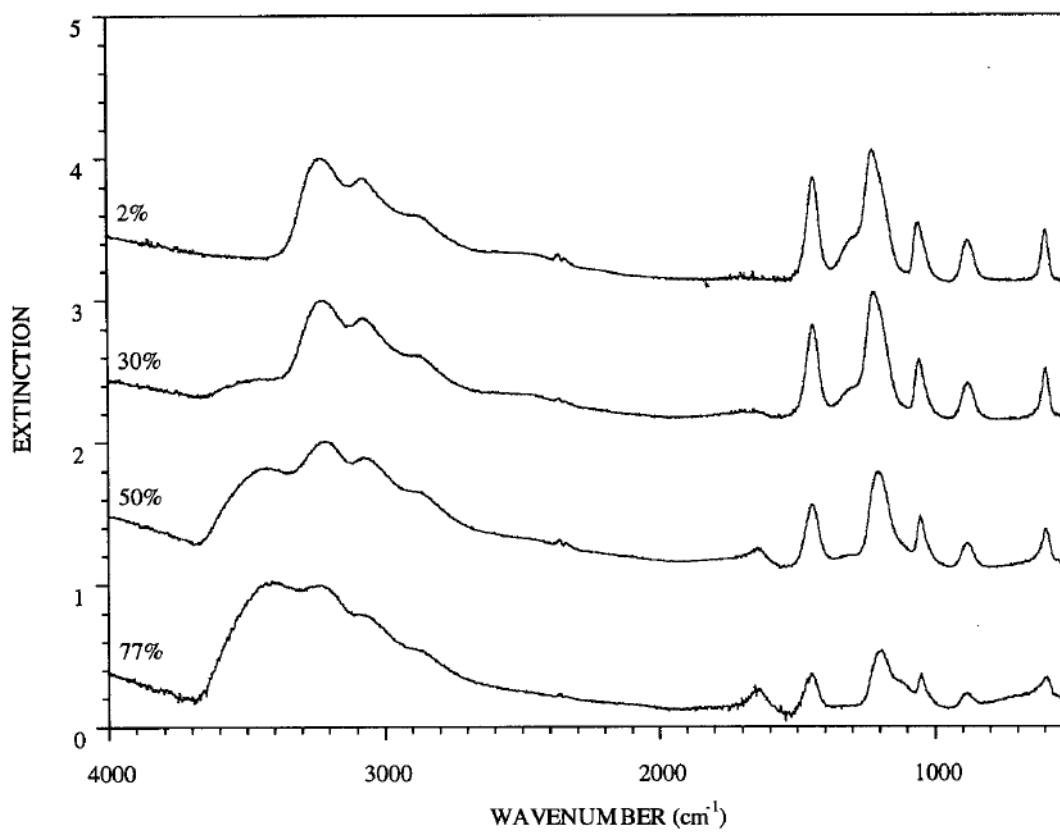


Figure 5.6. Spectra of aqueous ammonium nitrate at different relative humidity at 293 K from Cziczo and Abbatt (2000).

yielding an aqueous phase that contains $\sim 1.1 \times 10^{16}$ molecules of HNO_3 . Assuming a sticking coefficient of unity, a nitric acid pressure of only 5×10^{-9} Torr could condense 1.1×10^{16} molecules of HNO_3 in 2000 seconds, well within the time frame of the experiments. Therefore it is certainly possible that the liquid layer is developing at levels of nitric acid below the limit of detection of the mass spectrometer.

The FTIR-RAS and water uptake experiments support that the S_{crit} values determined are for heterogeneous (solid/liquid) nucleation. Therefore, critical heterogeneous supersaturation ratios for the solid/liquid mixed AN/ HNO_3 / H_2O films were determined between 190 and 210 K. The measured values are shown in Figure 5.7 representing at least seven experiments with error bars indicating one standard deviation. Figure 5.7 also shows the S_{crit} values for gold which lie above values determined for the mixed phase film confirming that nucleation is occurring in the condensed phase and not on the substrate. Compared to previous experiments, the S_{crit} values at 200 and 210 K are in agreement with the values of Shilling et al.(2006), and while the value at 190 K for low HNO_3 is less than the Shilling data by 0.1, the error bars for the results here and those previously do overlap.

The solid/liquid mixed AN/ HNO_3 films are observed to freeze well below the homogeneous freezing points ($S_{ice} \sim 1.6$) from the model proposed by Koop et al. (2000). However the model and the data the model is fit to uses only solution droplets. The experiments performed here consist of both solid and liquid phases, and the solid phase may provide a nucleation site for ice formation, thereby lowering the relative humidity at which nucleation is observed.

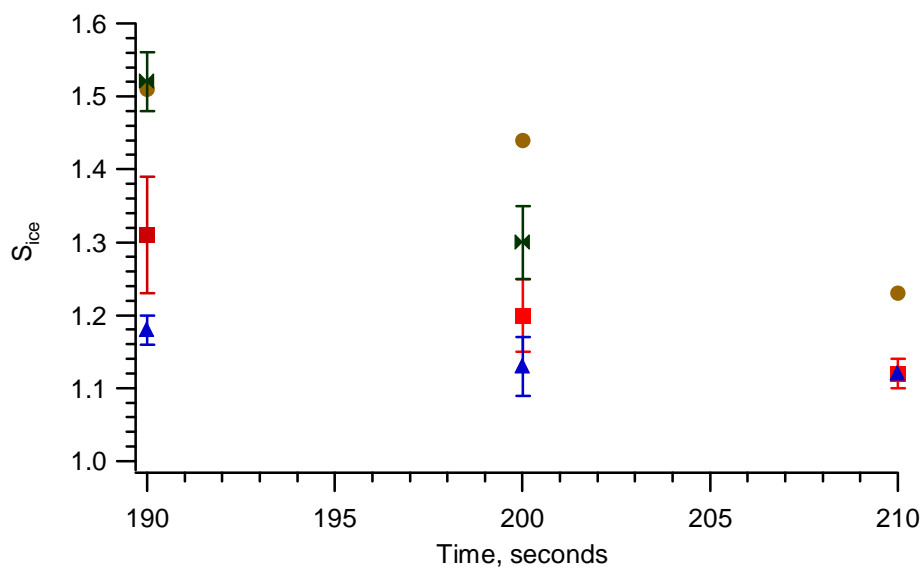


Figure 5.7. S_{ice} values determined for heterogeneous ice nucleation for mixed phase AN films at low pressure HNO_3 (red squares), for AN exposed to $\sim 10^{-7}$ Torr HNO_3 (blue triangles), for NAT (green), and for the gold substrate (gold circles). NAT formation was not observed at 210K.

10.3.2 Ice Nucleation on AN in the Presence of Nitric Acid

The values for S_{crit} for experiments conducted with nitric acid flow are shown in Figure 5.7, for nitric acid pressures ranging 1 to 3×10^{-7} Torr. At 210 K, the S_{ice} values are similar than the experiments with nitric acid below the limit of detection. However, at lower temperatures S_{crit} decreases in the presence of 10^{-7} Torr HNO_3 . Also with decreasing temperature, the difference between the S_{crit} values increases. Water uptake experiments were also performed at nitric acid pressures $\sim 10^{-7}$ Torr, and an example uptake shown in Figure 5.8. For the uptake the nitric acid pressure is above the equilibrium pressure of nitric acid predicted by the AIM model; therefore, continued growth of the supercooled liquid phase is predicted as the surface can not reach equilibrium. The uptake has a partial recovery, and the FTIR-RAS spectra confirm continued growth of the condensed phase. When the nitric acid vapour pressure is below the equilibrium pressure, the uptake trend is similar to Figure 5.6, with a recovery to the original pressure.

Experiments performed in the presence of $\sim 10^{-7}$ Torr of nitric acid had different outcomes, depending on the temperature and rate that the water pressure was increased. At 210 K, the aqueous phase grew when the saturation ratio was below S_{crit} and nucleated ice when the critical saturation was reached. At 200 and 190 K ice or nitric acid trihydrate (NAT) formation was observed. In these experiments, the difference between ice or NAT formation was kinetic in nature. If the water vapour was continually increased in the same manner shown in Figure 5.2, ice formation was observed. When the water pressure was held constant below S_{crit} , NAT formation occurred as shown in Figure 5.9. In Figure 5.9, Spectrum A is the original film, Spectrum B is the film during

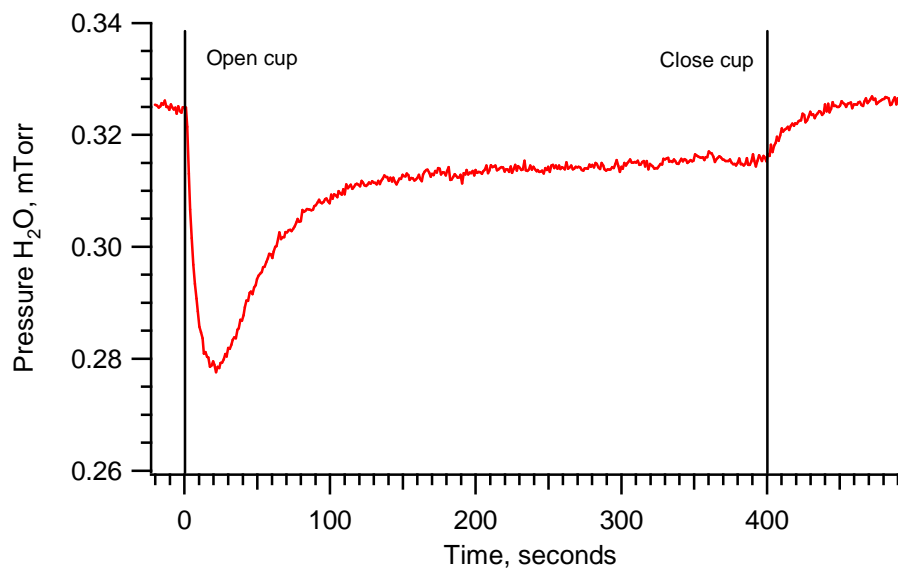


Figure 5.8. The uptake of water to an ammonium nitrate film exposed to 10^{-7} Torr H_2O . The uptake only recovers partially indicating continued uptake by the condensed phase.

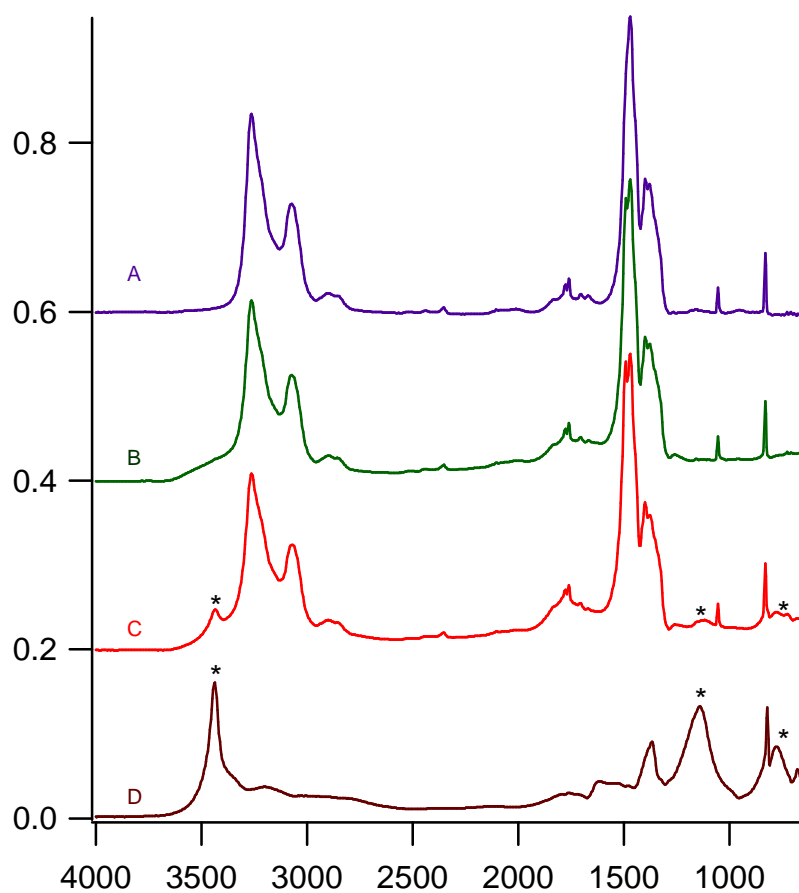


Figure 5.9. FTIR-RAS spectra of the nucleation of nitric acid trihydrate on ammonium nitrate. A. Original AN film. B. The film during exposure to 10^{-7} Torr HNO_3 and S_{ice} of 1.15. A supercooled layer of $\text{HNO}_3/\text{H}_2\text{O}$ is observed to grow on the film. C. Nitric acid trihydrate nucleation is observed. The asterisks indicate matching peaks from D, a spectrum of NAT.

exposure to 10^{-7} Torr HNO_3 , and Spectrum C is the film after NAT nucleation. For reference, and FTIR-RAS spectra of NAT is shown as Spectrum D. The strong, sharp peak centred at 3440 cm^{-1} is a clear indicator of NAT nucleation. At 190 K the average time required for NAT nucleation was ~ 10 minutes at constant H_2O pressure, while at 200 K the time required was ~ 30 minutes. After NAT formation occurred, S_{crit} values were determined for the nucleation of ice on NAT, and are shown in Figure 5.7. The S_{crit} values for NAT are significantly higher than the S_{crit} values for the mixed phase AN/ HNO_3 , and at 190K the value near that required for depositional nucleation on the bare gold substrate.

At 210 K, the film continued to grow for ~ 2 hours without NAT formation at $S_{ice} \sim 1.05$ and 2×10^{-7} Torr HNO_3 . After 2 hours, the aqueous phase was isothermally desorbed, and by using the desorption data shown in Figure 5.10, the number of molecules can be calculated by integrating the area under the curve. The calculations reveal 1.0×10^{19} molecules had condensed on the AN film, equivalent to ~ 500 nm of water over the two hours. While NAT formation was not observed for these conditions, a significant amount of water had partitioned to the condensed phase.

10.3.3 Experimental determination of the NAT growth rate

The ice nucleation experiments indicate that depending on the conditions either ice or NAT may nucleate in the upper troposphere. Therefore, it is necessary to understand both the evaporation and growth rate for these solid phases. To that end the growth rate of ice and NAT has been determined using both chamber pressure measurement instrumentation and FTIR-RAS. The FTIR-RAS results of the growth

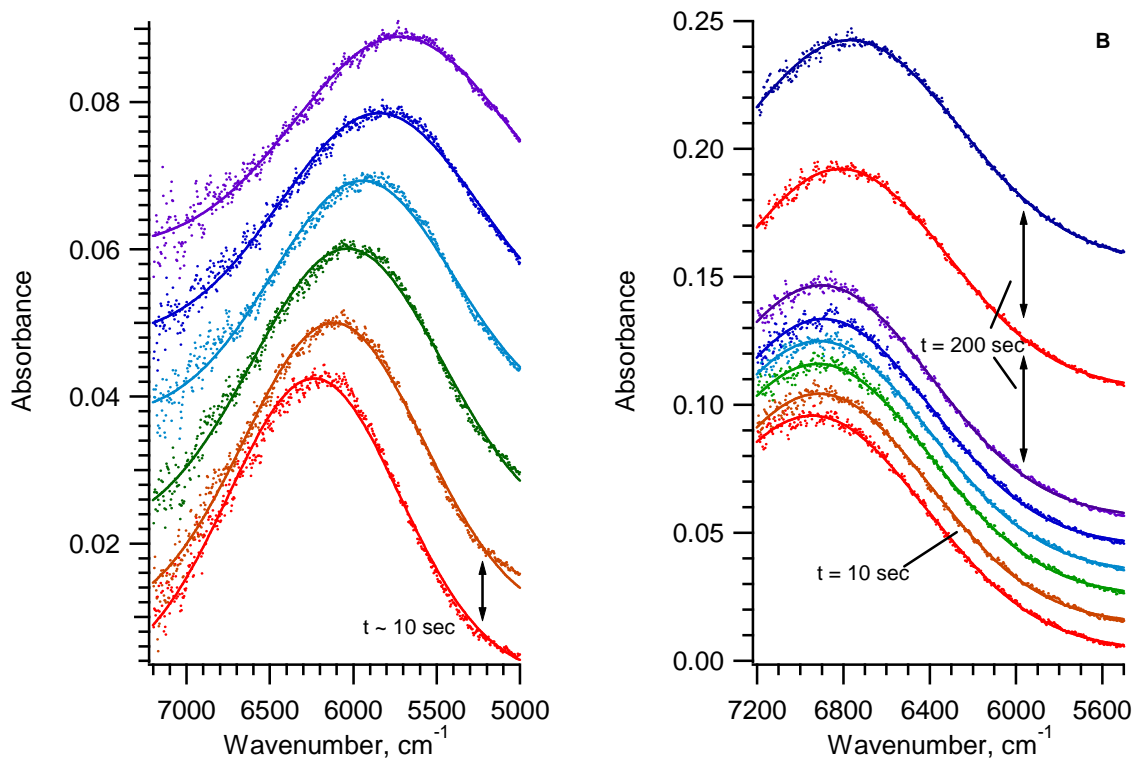


Figure 5.10. FTIR-RAS interference patterns from the growth of ice (A) and of NAT (B). In Panel A, each spectrum is separated by 10 seconds time. In Panel B, the lower six spectra are also spaced by 10 seconds, and the top two spectra are spaced by 200 seconds. The solid lines are Gaussian fits to the data (dots).

experiments performed at 200 K are shown in Figure 5.10. Figure 5.10 shows the interference pattern in the near IR caused by the thickness of the film, as described in Chapter 2.5. Panel A shows the growth of ice on the AN film. The interference pattern caused by the ice film thickness is clearly visible, and each spectrum is separated by 10 second intervals. Panel B shows the growth of a NAT film on AN. The interference pattern for NAT is shown initially at 10 second intervals, with the top two spectra spaced by 200 second intervals. It is clear from Figure 5.10, that even after 450 seconds of growth (bottom to top spectra), the NAT film has grown less than the ice film grew in just 10 seconds. Gaussian fits (solid lines, Figure 5.10) are used to pin point the interference maxima, and Equation 2.11 is used to calculate the thickness using published optical constants (Toon, 1994). The calculated growth rates for both ice and NAT are summarized in Table 5.1. An interesting trend is apparent, that at 200 K the NAT film grew at a slower rate than at 190 K, despite the higher pressure of water. However, NAT growth requires nitric acid; therefore the uptake of nitric acid regulates the growth of NAT. Also in Table 5.1 are the pressures of nitric acid for the growth experiments and literature γ values for nitric acid uptake to supercooled $\text{HNO}_3/\text{H}_2\text{O}/\text{ice}$ films. The calculated nitric acid uptake is a match for the nitric acid uptake experimentally required to grow the films at the 3:1 $\text{H}_2\text{O}:\text{HNO}_3$ ratio.

Evaporation experiments were also performed for ice and NAT films. The evaporation rates are similar, which confirms previous results (Delval and Rossi, 2005). It seems at first that the finding presents a thermodynamic conundrum, as proposed by Gao and coworkers (2004). If the evaporation kinetics are the same for both ice and NAT, but the uptake kinetics differ, than one could create a perpetual motion machine by

T, K	Film	Initial $P_{\text{H}_2\text{O}}$, 10^{-4} Torr	$^a\gamma_{\text{netH}_2\text{O}}$ $\times 10^{-4}$	b Baratron Growth Rate, nm/s	FTIR- RAS Growth Rate, nm/s	H_2O Uptake, molec/s	Required HNO_3 Uptake, molec/s	P_{HNO_3} , Torr	c Ave γ_{HNO_3}	Calc uptake, molec/s
190	NAT	3.83	12	8.4×10^{-2}	6.0×10^{-2}	1.1×10^{15}	3.5×10^{14}	8×10^{-7}	0.3	3.5×10^{14}
190	Ice	3.72	34	1.7×10^{-1}	1.7×10^{-1}	2.9×10^{15}				
200	NAT	14.5	1.8	4.0×10^{-2}	3.6×10^{-2}	5.1×10^{14}	1.7×10^{14}	6×10^{-7}	0.23	1.8×10^{14}
200	Ice	14.7	38	7.4×10^{-1}	8.6×10^{-1}	9.8×10^{15}				

^aThe γ value is for net uptake, which includes both uptake and sublimation from the surface

^bDensity of NAT estimated from density of aqueous nitric acid

^c γ values averaged from literature values (Leu, 1988; Hansen, 1992; Aguzzi and Rossi, 2001)

Table 5.1. Growth of ice and NAT films at 190 and 200 K.

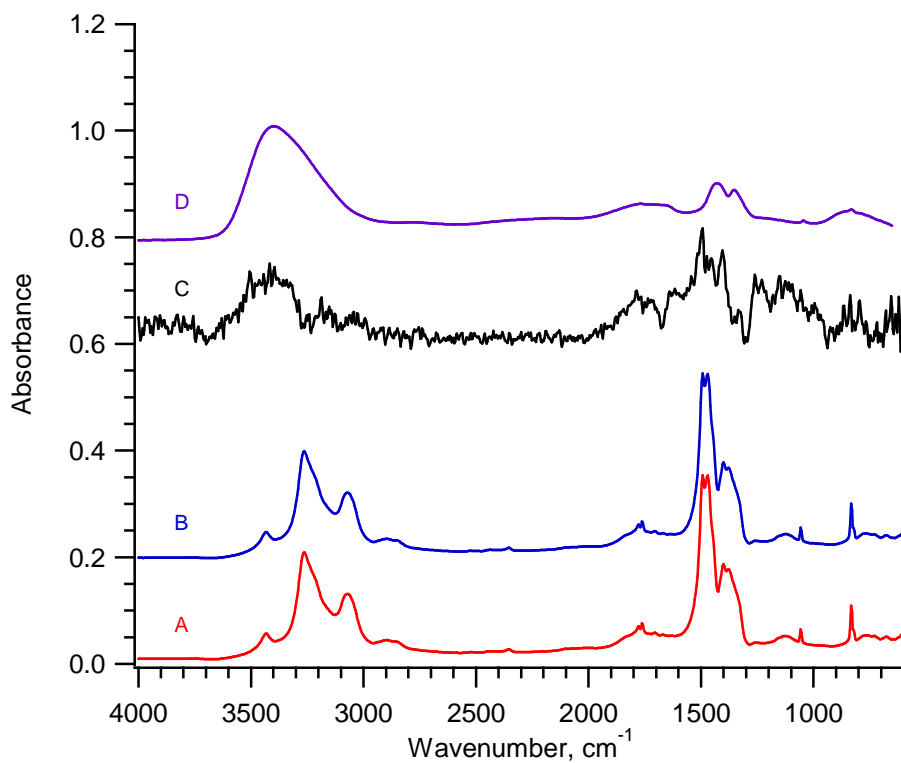


Figure 5.11. FTIR-RAS spectra of NAT films during growth and sublimation under high vacuum. Spectrum A is a the film during sublimation, and Spectra B is the film during growth. Spectrum C is a subtraction of A from B. The resulting spectrum is similar to Spectrum D which is of amorphous 3:1 H₂O/HNO₃.

coating a plug of ice sealed in a toroidal ring on one side with NAT, and the other with ice (McGraw, 2004). At equilibrium pressure, water vapour would condense on one side, and freely flow through the plug to the other, which would violate the second law of thermodynamics. However, examination of the FTIR-RAS spectra of the NAT film during growth, and during evaporation under high vacuum reveals a solution. Figure 5.11 is spectrum of the NAT film during growth, Spectrum A, with the spectrum of a NAT film of the same thickness during evaporation under high vacuum Spectrum B. Spectrum C is Spectrum B subtracted from Spectrum A. The spectra of amorphous 3:1 H₂O:HNO₃ is shown again as Spectrum D. Spectrum C indicates that during growth a layer of supercooled HNO₃/H₂O develops on the surface of the NAT.

The presence of a liquid layer solves the thermodynamic issue with the Gao et al. (2004) hypothesis. Both NAT and supercooled HNO₃/H₂O are stable under these conditions, though the supercooled liquid is the metastable state. During growth, the NAT does consume molecules from the metastable liquid layer. However, as molecules are consumed the liquid layer could replenish itself from the gas phase. Under high vacuum, the liquid phase is quickly removed, and the evaporation rate becomes that of crystalline NAT. In these experiments, the measured uptake is to the liquid layer, and growth of NAT from the supercooled liquid is slower than that of direct deposition on ice from the gas phase.

10.4 Atmospheric implications

The experiments performed here have confirmed the prediction of Lin and Tabazadeh (2002) for ammonium nitrate. The presence of even trace amounts of nitric

acid, less than 10^{-8} Torr, can cause mixed solid/liquid condensed phases. For low pressures of nitric acid ($< 10^{-8}$ Torr) ammonium nitrate is observed to heterogeneously nucleate ice at low S_{crit} values relative to homogenous nucleation (Koop, 2000), and depositional nucleation (Shilling, 2006). Under these conditions, particles containing sufficient ammonium nitrate may preferentially nucleate.

For pressures of $\text{HNO}_3 \sim 10^{-7}$ Torr, the state of the particle depends on the temperature and the rate of increase in relative humidity. At 210 K, the AN did not nucleate NAT but did uptake significant quantities of water. Experimentally, the AN film was observed to uptake ~ 600 nm of water at S_{ice} of 1.05. Therefore, if the nitric acid pressure is sufficient, particles could consist of mixed solid/liquid phases as they ascend in the UT. It is not likely they will grow continuously as determined experimentally, as eventually nitric acid would be scavenged from the gas phase and the particle would reach an equilibrium size.

As mixed phase particles rise they will eventually cool to temperatures where NAT nucleation is favoured. At 200 and 190 K, NAT nucleation occurred on AN in the presence of nitric acid when the relative humidity was held just above the saturation ratio with respect to ice. Given modelled updraft velocities and the corresponding slow adiabatic cooling rates in cirrus clouds (Gierens, 2003), NAT formation is likely as hours would pass before a particle is cooled to the determined critical saturation ratio for ice nucleation.

The experimental data indicates that the formation of NAT would truncate the particles growth in the upper troposphere. The growth rate of NAT is governed by the

uptake of nitric acid, and not the relative humidity. In the kinetic regime, the flux to a particle, I , can be calculated by:

$$I = \gamma n \langle v \rangle SA, \quad (5.1)$$

where γ , n , $\langle v \rangle$, SA are the uptake coefficient, number density of the gas, mean speed, and surface area respectively. For a first order approximation, a forward stepwise integration can be applied using Equation 5.1, by increasing the surface area respective to the uptake for 1 second steps of growth. Starting with an initial NAT particle 25 nm in diameter, using the γ values from Table 5.1, a gas phase pressure of nitric acid of 5×10^{-8} Torr (Popp, 2006), and a water pressure of 1.34×10^{-3} at 200 K the NAT particle would grow to approximately 55 nm in diameter. If we apply the same conditions to a 25 nm ice crystal, it would grow to 5300 nm in size. Therefore, small mixed phase particles that nucleate NAT will not grow to the size of a typical cirrus ice. Additionally, the high S_{crit} values for NAT would make these crystals an unlikely site for ice nucleation.

The experimental data here confirms the plausibility of the nitric acid inhibiting water uptake in cirrus clouds. While the original Gao et al. (2004) hypothesis may have had thermodynamic flaws, those issues are solved by the presence of a supercooled $\text{HNO}_3/\text{H}_2\text{O}$ which has been confirmed by the FTIR-RAS. However, additional experimentation would have to be performed to confirm that NAT could fully seal the ice portion from the surrounding atmosphere. If so, this process may explain the high supersaturation ratios measured in cirrus clouds.

References

- Abbatt, J. P. D., Interaction of HNO₃ with water-ice surfaces at temperatures of the free troposphere. *Geophysical Research Letters* **1997**, *24* (12), 1479-1482.
- Abbatt, J. P. D.; Benz, S.; Cziczo, D. J.; Kanji, Z.; Lohmann, U.; Mohler, O., Solid ammonium sulfate aerosols as ice nuclei: A pathway for cirrus cloud formation. *Science* **2006**, *313* (5794), 1770-1773.
- Arora, O. P.; Cziczo, D. J.; Morgan, A. M.; Abbott, J. P. D.; Niedziela, R. F., Uptake of nitric acid by sub-micron-sized ice particles. *Geophysical Research Letters* **1999**, *26* (24), 3621-3624.
- Audisio, G.; Priola, A.; Rossini, A., Cationic Oligomerization of Isoprene and Structure of Its Oligomers. *Makromolekulare Chemie-Macromolecular Symposia* **1991**, *47*, 263-270.
- Baustian, K. J.; Wise, M. E.; Tolbert, M. A., Depositional ice nucleation on solid ammonium sulfate and glutaric acid particles. *Atmospheric Chemistry and Physics* **2010**, *10* (5), 2307-2317.
- Beaver, M. R.; Elrod, M. J.; Garland, R. M.; Tolbert, M. A., Ice nucleation in sulfuric acid/organic aerosols: implications for cirrus cloud formation. *Atmospheric Chemistry and Physics* **2006**, *6*, 3231-3242.
- Beaver, M. R.; Garland, R. M.; Hasenkopf, C. A.; Baynard, T.; Ravishankara, A. R.; Tolbert, M. A., A laboratory investigation of the relative humidity dependence of light extinction by organic compounds from lignin combustion. *Environmental Research Letters* **2008**, *3* (4), 8.
- Benson, D. R.; Erupe, M. E.; Lee, S. H., Laboratory-measured H₂SO₄-H₂O-NH₃ ternary homogeneous nucleation rates: Initial observations. *Geophysical Research Letters* **2009**, *36*.
- Biermann, U. M.; Luo, B. P.; Peter, T., Absorption spectra and optical constants of binary and ternary solutions of H₂SO₄, HNO₃, and H₂O in the mid infrared at atmospheric temperatures. *Journal of Physical Chemistry A* **2000**, *104* (4), 783-793.
- Blake, N. J.; Blake, D. R.; Simpson, I. J.; Meinardi, S.; Swanson, A. L.; Lopez, J. P.; Katzenstein, A. S.; Barletta, B.; Shirai, T.; Atlas, E.; Sachse, G.; Avery, M.; Vay, S.; Fuelberg, H. E.; Kiley, C. M.; Kita, K.; Rowland, F. S., NMHCs and halocarbons in Asian continental outflow during the Transport and Chemical Evolution over the Pacific (TRACE-P) Field Campaign: Comparison with PEM-West B. *Journal of Geophysical Research-Atmospheres* **2003**, *108* (D20).
- Bogdan, A.; Molina, M. J., Why Does Large Relative Humidity with Respect to

Ice Persist in Cirrus Ice Clouds? *Journal of Physical Chemistry A* **2009**, *113* (51), 14123-14130.

Boge, O.; Miao, Y.; Plewka, A.; Herrmann, H., Formation of secondary organic particle phase compounds from isoprene gas-phase oxidation products: An aerosol chamber and field study. *Atmospheric Environment* **2006**, *40* (14), 2501-2509.

Bonn, B.; Hirsikko, A.; Hakola, H.; Kurten, T.; Laakso, L.; Boy, M.; Dal Maso, M.; Makela, J. M.; Kulmala, M., Ambient sesquiterpene concentration and its link to air ion measurements. *Atmospheric Chemistry and Physics* **2007**, *7* (11), 2893-2916.

Bonn, B.; Kulmala, M.; Riipinen, I.; Sihto, S. L.; Ruuskanen, T. M., How biogenic terpenes govern the correlation between sulfuric acid concentrations and new particle formation. *Journal of Geophysical Research-Atmospheres* **2008**, *113* (D12), 14.

Boy, M.; Karl, T.; Turnipseed, A.; Mauldin, R. L.; Kosciuch, E.; Greenberg, J.; Rathbone, J.; Smith, J.; Held, A.; Barsanti, K.; Wehner, B.; Bauer, S.; Wiedensohler, A.; Bonn, B.; Kulmala, M.; Guenther, A., New particle formation in the front range of the colorado rocky mountains. *Atmospheric Chemistry and Physics* **2008**, *8* (6), 1577-1590.

Brilman, D. W. F.; vanSwaaij, W. P. M.; Versteeg, G. F., On the absorption of isobutene and trans-2-butene in sulfuric acid solutions. *Industrial & Engineering Chemistry Research* **1997**, *36* (11), 4638-4650.

Claeys, M.; Graham, B.; Vas, G.; Wang, W.; Vermeylen, R.; Pashynska, V.; Cafmeyer, J.; Guyon, P.; Andreae, M. O.; Artaxo, P.; Maenhaut, W., Formation of secondary organic aerosols through photooxidation of isoprene. *Science* **2004**, *303* (5661), 1173-1176.

Claeys, M.; Wang, W.; Ion, A. C.; Kourtchev, I.; Gelencser, A.; Maenhaut, W., Formation of secondary organic aerosols from isoprene and its gas-phase oxidation products through reaction with hydrogen peroxide. *Atmospheric Environment* **2004**, *38* (25), 4093-4098.

Clegg, S. L.; Brimblecombe, P.; Wexler, A. S., Thermodynamic model of the system $\text{H}^+ \text{--} \text{NH}_4^+ \text{--} \text{SO}_4^{2-} \text{--} \text{NO}_3^- \text{--} \text{H}_2\text{O}$ at tropospheric temperatures. *Journal of Physical Chemistry A* **1998**, *102* (12), 2137-2154.

Cottrell, L. D.; Griffin, R. J.; Jimenez, J. L.; Zhang, Q.; Ulbrich, I.; Ziemba, L. D.; Beckman, P. J.; Sive, B. C.; Talbot, R. W., Submicron particles at Thompson Farm during ICARTT measured using aerosol mass spectrometry. *Journal of Geophysical Research-Atmospheres* **2008**, *113* (D8).

Cziczo, D. J.; Abbatt, J. P. D., Ice nucleation in NH_4HSO_4 , NH_4NO_3 , and H_2SO_4 aqueous particles: Implications for cirrus cloud formation. *Geophysical Research Letters* **2001**, 28 (6), 963-966.

Cziczo, D. J.; Murphy, D. M.; Hudson, P. K.; Thomson, D. S., Single particle measurements of the chemical composition of cirrus ice residue during CRYSTAL-FACE. *Journal of Geophysical Research-Atmospheres* **2004**, 109 (D4), 13.

Danckwerts, P. V., *Gas-liquid reactions*. McGraw-Hill Book Co.: New York,, 1970; p xiii, 276 p.

Delval, C.; Rossi, M. J., Influence of monolayer amounts of HNO_3 on the evaporation rate of H_2O over ice in the range 179 to 208 K: A quartz crystal microbalance study. *Journal Of Physical Chemistry A* **2005**, 109 (32), 7151-7165.

Docherty, K. S.; Ziemann, P. J., Reaction of oleic acid particles with NO_3 radicals: Products, mechanism, and implications for radical-initiated organic aerosol oxidation. *Journal of Physical Chemistry A* **2006**, 110 (10), 3567-3577.

Dockery, D. W.; Pope, C. A.; Xu, X. P.; Spengler, J. D.; Ware, J. H.; Fay, M. E.; Ferris, B. G.; Speizer, F. E., An Association Between Air-pollution and Mortality in 6 United-States Cities. *New England Journal of Medicine* **1993**, 329 (24), 1753-1759.

Doskey, P. V.; Gao, W. G., Vertical mixing and chemistry of isoprene in the atmospheric boundary layer: Aircraft-based measurements and numerical modeling. *Journal of Geophysical Research-Atmospheres* **1999**, 104 (D17), 21263-21274.

Dubowski, Y.; Sumner, A. L.; Menke, E. J.; Gaspar, D. J.; Newberg, J. T.; Hoffman, R. C.; Penner, R. M.; Hemminger, J. C.; Finlayson-Pitts, B. J., Interactions of gaseous nitric acid with surfaces of environmental interest. *Physical Chemistry Chemical Physics* **2004**, 6 (14), 3879-3888.

Edney, E. O.; Kleindienst, T. E.; Jaoui, M.; Lewandowski, M.; Offenbergl, J. H.; Wang, W.; Claeys, M., Formation of 2-methyl tetrols and 2-methylglyceric acid in secondary organic aerosol from laboratory irradiated isoprene/ NO_x / SO_2 /air mixtures and their detection in ambient $\text{PM}_{2.5}$ samples collected in the eastern United States. *Atmospheric Environment* **2005**, 39 (29), 5281-5289.

Ervens, B.; Kreidenweis, S. M., SOA formation by biogenic and carbonyl compounds: Data evaluation and application. *Environmental Science & Technology* **2007**, 41 (11), 3904-3910.

Feierabend, K. J.; Zhu, L.; Talukdar, R. K.; Burkholder, J. B., Rate Coefficients for the OH+HC(O)C(O)H (glyoxal) Reaction between 210 and 390. *Journal of Physical Chemistry A* **2008**, *112* (1), 73-82.

Finlayson-Pitts, B. J.; Pitts, J. N., *Chemistry of the upper and lower atmosphere : theory, experiments, and applications*. Academic Press: San Diego, 2000; p xxii, 969 p.

Fleury, G.; Tabacik, V., Glyoxylic Acid - Asymmetry of Free Molecule Vibration-Spectra and Attribution. *Journal of Molecular Structure* **1971**, *10* (3), 359-&.

Freedman, M. A.; Hasenkopf, C. A.; Beaver, M. R.; Tolbert, M. A., Optical Properties of Internally Mixed Aerosol Particles Composed of Dicarboxylic Acids and Ammonium Sulfate. *Journal of Physical Chemistry A* **2009**, *113* (48), 13584-13592.

Frinak, E. K.; Wermeille, S. J.; Mashburn, C. D.; Tolbert, M. A.; Pursell, C. J., Heterogeneous reaction of gaseous nitric acid on gamma-phase iron(III) oxide. *Journal of Physical Chemistry A* **2004**, *108* (9), 1560-1566.

Froyd, K. D.; Murphy, D. M.; Lawson, P.; Baumgardner, D.; Herman, R. L., Aerosols that form subvisible cirrus at the tropical tropopause. *Atmospheric Chemistry and Physics* **2010**, *10* (1), 209-218.

Froyd, K. D.; Murphy, D. M.; Sanford, T. J.; Thomson, D. S.; Wilson, J. C.; Pfister, L.; Lait, L., Aerosol composition of the tropical upper troposphere. *Atmospheric Chemistry and Physics* **2009**, *9* (13), 4363-4385.

Gao, R. S.; Popp, P. J.; Fahey, D. W.; Marcy, T. P.; Herman, R. L.; Weinstock, E. M.; Baumgardner, D. G.; Garrett, T. J.; Rosenlof, K. H.; Thompson, T. L.; Bui, P. T.; Ridley, B. A.; Wofsy, S. C.; Toon, O. B.; Tolbert, M. A.; Karcher, B.; Peter, T.; Hudson, P. K.; Weinheimer, A. J.; Heymsfield, A. J., Evidence that nitric acid increases relative humidity in low-temperature cirrus clouds. *Science* **2004**, *303* (5657), 516-520.

Gao, S.; Keywood, M.; Ng, N. L.; Surratt, J.; Varutbangkul, V.; Bahreini, R.; Flagan, R. C.; Seinfeld, J. H., Low-molecular-weight and oligomeric components in secondary organic aerosol from the ozonolysis of cycloalkenes and alpha-pinene. *Journal of Physical Chemistry A* **2004**, *108* (46), 10147-10164.

Gao, S.; Ng, N. L.; Keywood, M.; Varutbangkul, V.; Bahreini, R.; Nenes, A.; He, J. W.; Yoo, K. Y.; Beauchamp, J. L.; Hodyss, R. P.; Flagan, R. C.; Seinfeld, J. H., Particle phase acidity and oligomer formation in secondary organic aerosol. *Environmental Science & Technology* **2004**, *38* (24), 6582-6589.

Garland, R. M.; Wise, M. E.; Beaver, M. R.; DeWitt, H. L.; Aiken, A. C.; Jimenez, J. L.; Tolbert, M. A., Impact of palmitic acid coating on the water uptake and loss of ammonium sulfate particles. *Atmospheric Chemistry and Physics* **2005**, *5*, 1951-1961.

Gehlawat, J. K.; Sharma, M. M., Absorption of Isobutylene In Aqueous Solutions of Sulfuric Acid. *Chemical Engineering Science* **1968**, *23* (10), 1173-&.

Gensch, I. V.; Bunz, H.; Baumgardner, D. G.; Christensen, L. E.; Fahey, D. W.; Herman, R. L.; Popp, P. J.; Smith, J. B.; Troy, R. F.; Webster, C. R.; Weinstock, E. M.; Wilson, J. C.; Peter, T.; Kramer, M., Supersaturations, microphysics and nitric acid partitioning in a cold cirrus cloud observed during CR-AVE 2006: an observation-modelling intercomparison study. *Environmental Research Letters* **2008**, *3* (3).

Gierens, K., On the transition between heterogeneous and homogeneous freezing. *Atmospheric Chemistry and Physics* **2003**, *3*, 437-446.

Gmitro, J. I.; Vermeulen, T., Vapor-Liquid Equilibria for Aqueous Sulfuric Acid. *Aiche Journal* **1964**, *10* (5), 740-746.

Golden, D. M.; Spokes, G. N.; Benson, S. W., Very Low-Pressure Pyolysis (VLPP) - Versatile Kinetic Tool. *Angewandte Chemie-International Edition in English* **1973**, *12* (7), 534-546.

Greenberg, J. P.; Zimmerman, P. R., Nonmethane Hydrocarbons in Remote Tropical, Continental, and Marine Atmospheres. *Journal of Geophysical Research-Atmospheres* **1984**, *89* (ND3), 4767-4778.

Greenler, R. G., Infrared Study of Adsorbed Molecules on Metal Surfaces by Reflection Techniques. *Journal of Chemical Physics* **1966**, *44* (1), 310-&.

Griffin, R. J.; Dabdub, D.; Seinfeld, J. H., Secondary organic aerosol - 1. Atmospheric chemical mechanism for production of molecular constituents. *Journal of Geophysical Research-Atmospheres* **2002**, *107* (D17), 26.

Guenther, A.; Karl, T.; Harley, P.; Wiedinmyer, C.; Palmer, P. I.; Geron, C., Estimates of global terrestrial isoprene emissions using MEGAN (Model of Emissions of Gases and Aerosols from Nature). *Atmospheric Chemistry and Physics* **2006**, *6*, 3181-3210.

Guenther, A.; Hewitt, C. N.; Erickson, D.; Fall, R.; Geron, C.; Graedel, T.; Harley, P.; Klinger, L.; Lerdau, M.; McKay, W. A.; Pierce, T.; Scholes, B.; Steinbrecher, R.; Tallamraju, R.; Taylor, J.; Zimmerman, P., A Global-Model of Natural Volatile Organic-Compound Emissions. *Journal of Geophysical Research-Atmospheres* **1995**, *100* (D5), 8873-8892.

Hanson, D. R., The Uptake of HNO₃ onto Ice, NAT, and Frozen Sulfuric-Acid. *Geophysical Research Letters* **1992**, *19* (20), 2063-2066.

Heald, C. L.; Jacob, D. J.; Park, R. J.; Russell, L. M.; Huebert, B. J.; Seinfeld, J. H.; Liao, H.; Weber, R. J., A large organic aerosol source in the free troposphere missing from current models. *Geophysical Research Letters* **2005**, *32* (18).

Hudson, P. K.; Shilling, J. E.; Tolbert, M. A.; Toon, O. B., Uptake of nitric acid on ice at tropospheric temperatures: Implications for cirrus clouds. *Journal Of Physical Chemistry A* **2002**, *106* (42), 9874-9882.

Iraci, L. T.; Middlebrook, A. M.; Wilson, M. A.; Tolbert, M. A., Growth of Nitric Acid Hydrates on Thin Sulfuric-Acid Films. *Geophysical Research Letters* **1994**, *21* (10), 867-870.

Jacob, D. J., *Introduction to atmospheric chemistry*. Princeton University Press: Princeton, N.J., 1999; p xii, 266 p.

Jang, M. S.; Czoschke, N. M.; Lee, S.; Kamens, R. M., Heterogeneous atmospheric aerosol production by acid-catalyzed particle-phase reactions. *Science* **2002**, *298* (5594), 814-817.

Jensen, E. J.; Toon, O. B.; Vay, S. A.; Ovarlez, J.; May, R.; Bui, T. P.; Twohy, C. H.; Gandrud, B. W.; Poeschel, R. F.; Schumann, U., Prevalence of ice-supersaturated regions in the upper troposphere: Implications for optically thin ice cloud formation. *Journal of Geophysical Research-Atmospheres* **2001**, *106* (D15), 17253-17266.

Jensen, E.; Pfister, L.; Bui, T.; Weinheimer, A.; Weinstock, E.; Smith, J.; Pittman, J.; Baumgardner, D.; Lawson, P.; McGill, M. J., Formation of a tropopause cirrus layer observed over Florida during CRYSTAL-FACE. *Journal of Geophysical Research-Atmospheres* **2005**, *110* (D3).

Jimenez, J. L.; Canagaratna, M. R.; Donahue, N. M.; Prevot, A. S. H.; Zhang, Q.; Kroll, J. H.; DeCarlo, P. F.; Allan, J. D.; Coe, H.; Ng, N. L.; Aiken, A. C.; Docherty, K. S.; Ulbrich, I. M.; Grieshop, A. P.; Robinson, A. L.; Duplissy, J.; Smith, J. D.; Wilson, K. R.; Lanz, V. A.; Hueglin, C.; Sun, Y. L.; Tian, J.; Laaksonen, A.; Raatikainen, T.; Rautiainen, J.; Vaattovaara, P.; Ehn, M.; Kulmala, M.; Tomlinson, J. M.; Collins, D. R.; Cubison, M. J.; Dunlea, E. J.; Huffman, J. A.; Onasch, T. B.; Alfarra, M. R.; Williams, P. I.; Bower, K.; Kondo, Y.; Schneider, J.; Drewnick, F.; Borrmann, S.; Weimer, S.; Demerjian, K.; Salcedo, D.; Cottrell, L.; Griffin, R.; Takami, A.; Miyoshi, T.; Hatakeyama, S.; Shimono, A.; Sun, J. Y.; Zhang, Y. M.; Dzepina, K.; Kimmel, J. R.; Sueper, D.; Jayne, J. T.; Herndon, S. C.; Trimborn, A. M.; Williams, L. R.; Wood, E. C.; Middlebrook, A. M.; Kolb, C. E.; Baltensperger, U.; Worsnop, D. R., Evolution of Organic Aerosols in the Atmosphere. *Science* **2009**, *326* (5959), 1525-1529.

Kalberer, M.; Paulsen, D.; Sax, M.; Steinbacher, M.; Dommen, J.; Prevot, A. S. H.; Fisseha, R.; Weingartner, E.; Frankevich, V.; Zenobi, R.; Baltensperger, U., Identification of polymers as major components of atmospheric organic aerosols. *Science* **2004**, *303* (5664), 1659-1662.

Karcher, B.; Koop, T., The role of organic aerosols in homogeneous ice formation. *Atmospheric Chemistry and Physics* **2005**, *5*, 703-714.

Karcher, B.; Lohmann, U., A parameterization of cirrus cloud formation: Homogeneous freezing of supercooled aerosols. *Journal of Geophysical Research-Atmospheres* **2002**, *107* (D1-D2), 10.

Katsouyanni, K.; Pantazopoulou, A.; Touloumi, G.; Tselepidaki, I.; Moustiris, K.; Asimakopoulos, D.; Pouloupoulou, G.; Trichopoulos, D., Evidence for Interaction Between Air-Pollution and High-Temperature in the Causation of Excess Mortality. *Archives of Environmental Health* **1993**, *48* (4), 235-242.

Keywood, M. D.; Kroll, J. H.; Varutbangkul, V.; Bahreini, R.; Flagan, R. C.; Seinfeld, J. H., Secondary organic aerosol formation from cyclohexene ozonolysis: Effect of OH scavenger and the role of radical chemistry. *Environmental Science & Technology* **2004**, *38* (12), 3343-3350.

Keywood, M. D.; Varutbangkul, V.; Bahreini, R.; Flagan, R. C.; Seinfeld, J. H., Secondary organic aerosol formation from the ozonolysis of cycloalkenes and related compounds. *Environmental Science & Technology* **2004**, *38* (15), 4157-4164.

Knopf, D. A.; Lopez, M. D., Homogeneous ice freezing temperatures and ice nucleation rates of aqueous ammonium sulfate and aqueous levoglucosan particles for relevant atmospheric conditions. *Physical Chemistry Chemical Physics* **2009**, *11* (36), 8056-8068.

Koop, T.; Luo, B. P.; Tsias, A.; Peter, T., Water activity as the determinant for

homogeneous ice nucleation in aqueous solutions. *Nature* **2000**, *406* (6796), 611-614.

Kramer, M.; Schiller, C.; Afchine, A.; Bauer, R.; Gensch, I.; Mangold, A.; Schlicht, S.; Spelten, N.; Sitnikov, N.; Borrmann, S.; de Reus, M.; Spichtinger, P., Ice supersaturations and cirrus cloud crystal numbers. *Atmospheric Chemistry and Physics* **2009**, *9* (11), 3505-3522.

Kroll, J. H.; Ng, N. L.; Murphy, S. M.; Flagan, R. C.; Seinfeld, J. H., Secondary organic aerosol formation from isoprene photooxidation under high-NO_x conditions. *Geophysical Research Letters* **2005**, *32* (18).

Kroll, J. H.; Ng, N. L.; Murphy, S. M.; Varutbangkul, V.; Flagan, R. C.; Seinfeld, J. H., Chamber studies of secondary organic aerosol growth by reactive uptake of simple carbonyl compounds. *Journal of Geophysical Research-Atmospheres* **2005**, *110* (D23).

Kulmala, M.; Kerminen, V. M., On the formation and growth of atmospheric nanoparticles. *Atmospheric Research* **2008**, *90* (2-4), 132-150.

Larson, B. H.; Swanson, B. D., Experimental investigation of the homogeneous freezing of aqueous ammonium sulfate droplets. *Journal of Physical Chemistry A* **2006**, *110* (5), 1907-1916.

Lawson, R. P.; Pilson, B.; Baker, B.; Mo, Q.; Jensen, E.; Pfister, L.; Bui, P., Aircraft measurements of microphysical properties of subvisible cirrus in the tropical tropopause layer. *Atmospheric Chemistry and Physics* **2008**, *8* (6), 1609-1620.

Lee, C.; Martin, R. V.; van Donkelaar, A.; O'Byrne, G.; Krotkov, N.; Richter, A.; Huey, L. G.; Holloway, J. S., Retrieval of vertical columns of sulfur dioxide from SCIAMACHY and OMI: Air mass factor algorithm development, validation, and error analysis. *Journal of Geophysical Research-Atmospheres* **2009**, *114*, 20.

Liggio, J.; Li, S. M., Reactive uptake of pinonaldehyde on acidic aerosols. *Journal of Geophysical Research-Atmospheres* **2006**, *111* (D24).

Liggio, J.; Li, S. M., Reversible and irreversible processing of biogenic olefins on acidic aerosols. *Atmospheric Chemistry and Physics* **2008**, *8* (7), 2039-2055.

Liggio, J.; Li, S. M.; Brook, J. R.; Mihele, C., Direct polymerization of isoprene and alpha-pinene on acidic aerosols. *Geophysical Research Letters* **2007**, *34* (5).

Liggio, J.; Li, S. M.; McLaren, R., Heterogeneous reactions of glyoxal on particulate matter: Identification of acetals and sulfate esters. *Environmental Science & Technology* **2005**, *39* (6), 1532-1541.

Liggio, J.; Li, S. M.; McLaren, R., Reactive uptake of glyoxal by particulate matter. *Journal of Geophysical Research-Atmospheres* **2005**, *110* (D10).

Lin, J. S.; Tabazadeh, A., The effect of nitric acid uptake on the deliquescence and efflorescence of binary ammoniated salts in the upper troposphere. *Geophysical Research Letters* **2002**, *29* (10).

Lu, Y.; Khalil, M. A. K., Tropospheric OH - Model-Calculations of Spatial, Temporal, and Secular Variations. *Chemosphere* **1991**, *23* (3), 397-444.

Mackay, D.; Shiu, W. Y., A Critical Review of Henry's Law Constants for Chemicals of Environmental Interest. *Journal of Physical and Chemical Reference Data* **1981**, *10* (4), 1175-1199.

Mangold, A.; Wagner, R.; Saathoff, H.; Schurath, U.; Gieseemann, C.; Ebert, V.; Kramer, M.; Mohler, O., Experimental investigation of ice nucleation by different types of aerosols in the aerosol chamber AIDA: implications to microphysics of cirrus clouds. *Meteorologische Zeitschrift* **2005**, *14* (4), 485-497.

Marcilli, C.; Luo, B. P.; Peter, T., Mixing of the organic aerosol fractions: Liquids as the thermodynamically stable phases. *Journal of Physical Chemistry A* **2004**, *108* (12), 2216-2224.

Marti, J.; Mauersberger, K., A Survey and New Measurements of Ice Vapor-Pressure at Temperatures Between 170 AND 250K. *Geophysical Research Letters* **1993**, *20* (5), 363-366.

Mashburn, C. D.; Frinak, E. K.; Tolbert, M. A., Heterogeneous uptake of nitric acid on Na-montmorillonite clay as a function of relative humidity. *Journal of Geophysical Research-Atmospheres* **2006**, *111* (D15), 14.

McGraw, R., Humidity, ice, and nitric acid. *Science* **2004**, *304* (5673), 961-961.

McLafferty, F. W.; Turecek, F. e., *Interpretation of mass spectra*. 4th ed.; Mill Valley, Calif. bUniversity Science Books,, 1993; p xviii, 371 p.

Middlebrook, A. M.; Berland, B. S.; George, S. M.; Tolbert, M. A.; Toon, O. B., Real Refractive-Indexes of Infrared-Characterized Nitric-Acid Ice Films - Implications For Optical Measurements of Polar Stratospheric Clouds. *Journal of Geophysical Research-Atmospheres* **1994**, *99* (D12), 25655-25666.

Middlebrook, A. M.; Iraci, L. T.; McNeill, L. S.; Koehler, B. G.; Wilson, M. A.; Saastad, O. W.; Tolbert, M. A.; Hanson, D. R., Fourier Transform-Infrared Studies of Thin H₂SO₄/H₂O Films - Formation, Water-Uptake, and Solid-Liquid Phase-Changes. *Journal of Geophysical Research-Atmospheres* **1993**, *98* (D11), 20473-20481.

Middlebrook, A. M.; Murphy, D. M.; Thomson, D. S., Observations of organic material in individual marine particles at Cape Grim during the First Aerosol Characterization Experiment (ACE 1). *Journal of Geophysical Research-Atmospheres* **1998**, *103* (D13), 16475-16483.

Mirme, S.; Mirme, A.; Minikin, A.; Petzold, A.; Horrak, U.; Kerminen, V. M.; Kulmala, M., Atmospheric sub-3 nm particles at high altitudes. *Atmospheric Chemistry and Physics* **2010**, *10* (2), 437-451.

Muller, J. F., Geographical-Distribution and Seasonal-Variation of Surface Emissions and Deposition Velocities of Atmospheric Trace Gases. *Journal of Geophysical Research-Atmospheres* **1992**, *97* (D4), 3787-3804.

Murphy, D. M.; Cziczo, D. J.; Froyd, K. D.; Hudson, P. K.; Matthew, B. M.; Middlebrook, A. M.; Peltier, R. E.; Sullivan, A.; Thomson, D. S.; Weber, R. J., Single-particle mass spectrometry of tropospheric aerosol particles. *Journal of Geophysical Research-Atmospheres* **2006**, *111* (D23).

Murphy, D. M.; Cziczo, D. J.; Hudson, P. K.; Thomson, D. S., Carbonaceous material in aerosol particles in the lower stratosphere and tropopause region. *Journal of Geophysical Research-Atmospheres* **2007**, *112* (D4), 10.

Murray, B. J., Inhibition of ice crystallisation in highly viscous aqueous organic acid droplets. *Atmospheric Chemistry and Physics* **2008**, *8* (17), 5423-5433.

Murray, B. J.; Wilson, T. W.; Dobbie, S.; Cui, Z. Q.; Al-Jumur, S.; Mohler, O.; Schnaiter, M.; Wagner, R.; Benz, S.; Niemand, M.; Saathoff, H.; Ebert, V.; Wagner, S.; Karcher, B., Heterogeneous nucleation of ice particles on glassy aerosols under cirrus conditions. *Nature Geoscience* **2010**, *3* (4), 233-237.

Myriokefalitakis, S.; Vrekoussis, M.; Tsigaridis, K.; Wittrock, F.; Richter, A.; Bruhl, C.; Volkamer, R.; Burrows, J. P.; Kanakidou, M., The influence of natural and anthropogenic secondary sources on the glyoxal global distribution. *Atmospheric Chemistry and Physics* **2008**, *8* (16), 4965-4981.

Nel, A., Air pollution-related illness: Effects of particles. *Science* **2005**, *308* (5723), 804-806.

Ng, N. L.; Chhabra, P. S.; Chan, A. W. H.; Surratt, J. D.; Kroll, J. H.; Kwan, A. J.; McCabe, D. C.; Wennberg, P. O.; Sorooshian, A.; Murphy, S. M.; Dalleska, N. F.; Flagan, R. C.; Seinfeld, J. H., Effect of NO_x level on secondary organic aerosol (SOA) formation from the photooxidation of terpenes. *Atmospheric Chemistry and Physics* **2007**, *7* (19), 5159-5174.

Nguyen, H. N.; Martinsson, B. G.; Wagner, J. B.; Carlemalm, E.; Ebert, M.; Weinbruch, S.; Brenninkmeijer, C. A. M.; Heintzenberg, J.; Hermann, M.; Schuck, T.; van Velthoven, P. F. J.; Zahn, A., Chemical composition and morphology of individual aerosol particles from a CARIBIC flight at 10 km altitude between 50 degrees N and 30 degrees S. *Journal of Geophysical Research-Atmospheres* **2008**, *113* (D23).

Norman, M. L.; Qian, J.; Miller, R. E.; Worsnop, D. R., Infrared complex refractive indices of supercooled liquid HNO₃/H₂O aerosols. *Journal of Geophysical Research-Atmospheres* **1999**, *104* (D23), 30571-30584.

Nriagu, J. O.; Simmons, M. S., *Environmental oxidants*. J. Wiley: New York, 1994; p xviii, 630 p.

O'Dowd, C. D.; Aalto, P.; Hameri, K.; Kulmala, M.; Hoffmann, T., Aerosol formation - Atmospheric particles from organic vapours. *Nature* **2002**, *416* (6880), 497-498.

Odian, G. G., *Principles of polymerization*. 4th ed.; Wiley-Interscience: Hoboken, N.J., 2004; p xxiv, 812 p.

Oura, K., *Surface science : an introduction*. Springer: Berlin ; New York, 2003; p xii, 440 p.

Pant, A.; Fok, A.; Parsons, M. T.; Mak, J.; Bertram, A. K., Deliquescence and crystallization of ammonium sulfate-glutaric acid and sodium chloride-glutaric acid particles. *Geophysical Research Letters* **2004**, *31* (12), 4.

Patton, J. S.; Byron, P. R., Inhaling medicines: delivering drugs to the body through the lungs. *Nature Reviews Drug Discovery* **2007**, *6* (1), 67-74.

Pope, C. A.; Ezzati, M.; Dockery, D. W., Fine-Particulate Air Pollution and Life Expectancy in the United States. *New England Journal of Medicine* **2009**, *360* (4), 376-386.

Popp, P. J.; Marcy, T. P.; Jensen, E. J.; Karcher, B.; Fahey, D. W.; Gao, R. S.; Thompson, T. L.; Rosenlof, K. H.; Richard, E. C.; Herman, R. L.; Weinstock, E. M.; Smith, J. B.; May, R. D.; Vomel, H.; Wilson, J. C.; Heymsfield, A. J.; Mahoney, M. J.; Thompson, A. M., The observation of nitric acid-containing particles in the tropical lower stratosphere. *Atmospheric Chemistry And Physics* **2006**, *6*, 601-611.

Prenni, A. J.; DeMott, P. J.; Kreidenweis, S. M.; Sherman, D. E.; Russell, L. M.; Ming, Y., The effects of low molecular weight dicarboxylic acids on cloud formation. *Journal of Physical Chemistry A* **2001**, *105* (50), 11240-11248.

Riipinen, I.; Sihto, S. L.; Kulmala, M.; Arnold, F.; Dal Maso, M.; Birmili, W.; Saarnio, K.; Teinila, K.; Kerminen, V. M.; Laaksonen, A.; Lehtinen, K. E. J., Connections between atmospheric sulphuric acid and new particle formation during QUEST III-IV campaigns in Heidelberg and Hyyti. *Atmospheric Chemistry and Physics* **2007**, *7* (8), 1899-1914.

Robinson, M. S.; Mallick, G.; Spillman, J. L.; Carreon, P. A.; Shalloo, S., Polarization-dependent interference effects in grazing-angle Fourier transform infrared reflection-absorption spectroscopy to determine the thickness of water-ice films. *Applied Optics* **1999**, *38* (1), 91-95.

Ruppert, L. F.; Tewalt, S. J.; Bragg, L. J.; Wallack, R. N., A digital resource model of the upper Pennsylvanian Pittsburgh coal bed, Monongahela Group, northern Appalachian basin coal region, USA. *International Journal of Coal Geology* **1999**, *41* (1-2), 3-24.

Ryoo, J. M.; Waugh, D. W.; Gettelman, A., Variability of subtropical upper tropospheric humidity. *Atmospheric Chemistry and Physics* **2008**, *8* (10), 2643-2655.

Seinfeld, J. H.; Pandis, S. N., *Atmospheric chemistry and physics : from air pollution to climate change*. 2nd ed.; Wiley: Hoboken, N.J., 2006; p xxviii, 1203 p.

Shibata, T.; Vomel, H.; Hamdi, S.; Kaloka, S.; Hasebe, F.; Fujiwara, M.; Shiotani, M., Tropical cirrus clouds near cold point tropopause under ice supersaturated conditions observed by lidar and balloon-borne cryogenic frost point hygrometer. *Journal of Geophysical Research-Atmospheres* **2007**, *112* (D3).

Shilling, J. E.; Fortin, T. J.; Tolbert, M. A., Depositional ice nucleation on crystalline organic and inorganic solids. *Journal of Geophysical Research-Atmospheres* **2006**, *111* (D12).

Shilling, J. E.; King, S. M.; Mochida, M.; Martin, S. T., Mass spectral evidence that small changes in composition caused by oxidative aging processes alter aerosol CCN properties. *Journal of Physical Chemistry A* **2007**, *111* (17), 3358-3368.

Shilling, J. E.; Tolbert, M. A., Uptake of acetic acid on thin ammonium nitrate films as a function of temperature and relative humidity. *Journal of Physical Chemistry A* **2004**, *108* (51), 11314-11320.

Shilling, J. E.; Tolbert, M. A.; Toon, O. B.; Jensen, E. J.; Murray, B. J.; Bertram, A. K., Measurements of the vapor pressure of cubic ice and their implications for atmospheric ice clouds. *Geophysical Research Letters* **2006**, *33* (17).

Shu, Y. H.; Atkinson, R., Atmospheric Lifetimes and Fates of a Series of Sesquiterpenes. *Journal of Geophysical Research-Atmospheres* **1995**, *100* (D4), 7275-7281.

Sipila, M.; Berndt, T.; Petaja, T.; Brus, D.; Vanhanen, J.; Stratmann, F.; Patokoski, J.; Mauldin, R. L.; Hyvarinen, A. P.; Lihavainen, H.; Kulmala, M., The Role of Sulfuric Acid in Atmospheric Nucleation. *Science* **2010**, *327* (5970), 1243-1246.

Smith, J. N.; Dunn, M. J.; VanReken, T. M.; Iida, K.; Stolzenburg, M. R.; McMurry, P. H.; Huey, L. G., Chemical composition of atmospheric nanoparticles formed from nucleation in Tecamac, Mexico: Evidence for an important role for organic species in nanoparticle growth. *Geophysical Research Letters* **2008**, *35* (4), 5.

Smith, J. N.; Moore, K. F.; Eisele, F. L.; Voisin, D.; Ghimire, A. K.; Sakurai, H.; McMurry, P. H., Chemical composition of atmospheric nanoparticles during nucleation events in Atlanta. *Journal of Geophysical Research-Atmospheres* **2005**, *110* (D22), 13.

Solomon, S.; Intergovernmental Panel on Climate Change.; Intergovernmental Panel on Climate Change. Working Group I., Climate change 2007 the physical science basis : contribution of Working Group I to the Fourth Assessment Report of the Intergovernmental Panel on Climate Change. IPCC Secretariat: Geneva, Switzerland, 2007. <http://www.ipcc.ch/ipccreports/ar4-wg1.htm>.

Spiro, P. A.; Jacob, D. J.; Logan, J. A., Global Inventory of Sulfur Emissions With 1-Degrees-X1-Degrees Resolution. *Journal of Geophysical Research-Atmospheres* **1992**, *97* (D5), 6023-6036.

Surratt, J. D.; Lewandowski, M.; Offenberg, J. H.; Jaoui, M.; Kleindienst, T. E.; Edney, E. O.; Seinfeld, J. H., Effect of acidity on secondary organic aerosol formation from isoprene. *Environmental Science & Technology* **2007**, *41* (15), 5363-5369.

Tang, I. N., Chemical and size effects of hygroscopic aerosols on light scattering coefficients. *Journal of Geophysical Research-Atmospheres* **1996**, *101* (D14), 19245-19250.

Tanner, R. L.; Olszyna, K. J.; Edgerton, E. S.; Knipping, E.; Shaw, S. L., Searching for evidence of acid-catalyzed enhancement of secondary organic aerosol formation using ambient aerosol data. *Atmospheric Environment* **2009**, *43* (21), 3440-3444.

Toon, O. B.; Tolbert, M. A.; Koehler, B. G.; Middlebrook, A. M.; Jordan, J., Infrared Optical-Constants of H₂O Ice, Amorphous Nitric-Acid Solutions, and Nitric-Acid Hydrates. *Journal of Geophysical Research-Atmospheres* **1994**, *99* (D12), 25631-25654.

Ulbrich, I. M.; Canagaratna, M. R.; Zhang, Q.; Worsnop, D. R.; Jimenez, J. L., Interpretation of organic components from Positive Matrix Factorization of aerosol mass spectrometric data. *Atmospheric Chemistry and Physics* **2009**, *9* (9), 2891-2918.

Ullerstam, M.; Thornberry, T.; Abbatt, J. P. D., Uptake of gas-phase nitric acid to ice at low partial pressures: evidence for unsaturated surface coverage. *Faraday Discussions* **2005**, *130*, 211-226.

Voigt, C.; Schlager, H.; Ziereis, H.; Karcher, B.; Luo, B. P.; Schiller, C.; Kramer, M.; Popp, P. J.; Irie, H.; Kondo, Y., Nitric acid in cirrus clouds. *Geophysical Research Letters* **2006**, *33* (5), 4.

Volkamer, R.; Jimenez, J. L.; San Martini, F.; Dzepina, K.; Zhang, Q.; Salcedo, D.; Molina, L. T.; Worsnop, D. R.; Molina, M. J., Secondary organic aerosol formation from anthropogenic air pollution: Rapid and higher than expected. *Geophysical Research Letters* **2006**, *33* (17).

Volkamer, R.; Martini, F. S.; Molina, L. T.; Salcedo, D.; Jimenez, J. L.; Molina, M. J., A missing sink for gas-phase glyoxal in Mexico City: Formation of secondary organic aerosol. *Geophysical Research Letters* **2007**, *34* (19).

Wang, L.; Khalizov, A. F.; Zheng, J.; Xu, W.; Ma, Y.; Lal, V.; Zhang, R. Y., Atmospheric nanoparticles formed from heterogeneous reactions of organics. *Nature Geoscience* **2010**, *3* (4), 238-242.

Willeke, K.; American Chemical Society.; Nihon Kagakkai., *Generation of aerosols and facilities for exposure experiments*. Ann Arbor Science: Ann Arbor, Mich., 1980; p ix, 597 p.

Wise, M. E.; Baustian, K. J.; Tolbert, M. A., Laboratory studies of ice formation pathways from ammonium sulfate particles. *Atmospheric Chemistry and Physics* **2009**, *9* (5), 1639-1646.

Wise, M. E.; Garland, R. M.; Tolbert, M. A., Ice nucleation in internally mixed ammonium sulfate/dicarboxylic acid particles. *Journal of Geophysical Research-Atmospheres* **2004**, *109* (D19).

Zhang, R. Y.; Suh, I.; Zhao, J.; Zhang, D.; Fortner, E. C.; Tie, X. X.; Molina, L. T.; Molina, M. J., Atmospheric new particle formation enhanced by organic acids. *Science* **2004**, *304* (5676), 1487-1490.

Zobrist, B.; Marcolli, C.; Pedernera, D. A.; Koop, T., Do atmospheric aerosols form glasses? *Atmospheric Chemistry and Physics* **2008**, *8* (17), 5221-5244.

Zobrist, B.; Marcolli, C.; Peter, T.; Koop, T., Heterogeneous ice nucleation in aqueous solutions: the role of water activity. *Journal of Physical Chemistry A* **2008**, *112* (17), 3965-3975.

Zondlo, M. A.; Barone, S. B.; Tolbert, M. A., Condensed-phase products in heterogeneous reactions: N₂O₅, ClONO₂, and HNO₃ reacting on ice films at 185 K. *Journal Of Physical Chemistry A* **1998**, *102* (29), 5735-5748.

Zondlo, M. A.; Onasch, T. B.; Warshawsky, M. S.; Tolbert, M. A.; Mallick, G.; Arentz, P.; Robinson, M. S., Experimental studies of vapor-deposited water-ice films using grazing-angle FTIR-reflection absorption spectroscopy. *Journal of Physical Chemistry B* **1997**, *101* (50), 10887-10895.

Zuberi, B.; Bertram, A. K.; Cassa, C. A.; Molina, L. T.; Molina, M. J., Heterogeneous nucleation of ice in (NH₄)₂SO₄-H₂O particles with mineral dust immersions. *Geophysical Research Letters* **2002**, *29* (10).